

NASA Contractor Report 195440

1N-71
62759
p. 150

Active Control of Fan Noise-Feasibility Study

Volume 2: Canceling Noise Source-Design of an Acoustic Plate Radiator Using Piezoceramic Actuators

F.G. Pla and H. Rajiyah
General Electric Aircraft Engines
Cincinnati, Ohio

(NASA-CR-195440) ACTIVE CONTROL OF
FAN NOISE-FEASIBILITY STUDY. VOLUME
2: CANCELING NOISE SOURCE-DESIGN OF
AN ACOUSTIC PLATE RADIATOR USING
PIEZOCERAMIC ACTUATORS (GE) 150 p

N96-13385

Unclass

63/71 0062759

March 1995

Prepared for
Lewis Research Center
Under Contract NAS3-26617



National Aeronautics and
Space Administration

EXECUTIVE SUMMARY

The feasibility of using acoustic plate radiators powered by piezoceramic thin sheets as canceling sources for active control of aircraft engine fan noise is demonstrated.

Analytical and numerical models of actuated beams and plates are developed and validated. Analytical and experimental responses are within 1 % to 3 % of each other for aluminum plates. An optimization study is performed to identify the optimum combination of design parameters that maximizes the plate volume velocity for a given resonance frequency.

Fifteen plates with various plate and actuator sizes, thicknesses, and bonding layers were fabricated and tested using results from the optimization study. A maximum equivalent piston displacement of 0.39 mm was achieved with the optimized plate samples tested with only one actuator powered, corresponding to a plate deflection at the center of over 1 millimeter. This is very close to the deflection required for a full size engine application and represents a 160-fold improvement over previous work.

Experimental results further show that performance is limited by the critical stress of the piezoceramic actuator and bonding layer rather than by the maximum moment available from the actuator. In addition, for high stress levels and for high electrical fields, nonlinearities in the mechanical and electrical properties of the actuator material result in a drop in resonance frequency and velocity response.

Design enhancements are described in detail that will lead to a flight-worthy acoustic plate radiator by minimizing actuator tensile stresses and reduce nonlinear effects.

Finally, several adaptive tuning methods designed to increase the bandwidth of acoustic plate radiators are analyzed including passive, active, and semi-active approaches. The back chamber pressurization and volume variation methods are investigated experimentally and shown to be simple and effective ways to obtain substantial control over the resonance frequency of a plate radiator.

This study shows that piezoceramic-based plate radiators can be a viable acoustic source for active control of aircraft engine fan noise.

TABLE OF CONTENTS - VOLUME II

1.	Introduction.....	1
	1.1. General Background	1
	1.2. Piezoelectric Actuators in Active Noise and Vibration Control	2
	1.3. Current Investigation	4
2.	Structural Actuation using Piezoelectric Materials: Fundamental Principles - Beam Study.....	6
	2.1. Linear PZT Constitutive Relations	6
	2.2. Analytical Formulation for a PZT/Beam Configuration.....	7
	2.2.1. Analytical Derivation of a Single PZT/Beam Configuration....	7
	2.2.2. Generalized FEM Approach	13
	2.3. Experimental Validation - Beam Experiments	15
	2.3.1. Experimental Setup	15
	2.3.2. Results	17
	2.3.2.1. Lexan Beam.....	17
	2.3.2.2. Aluminum Beam	22
	2.3.2.3. Steel Beam.....	23
	2.3.3. Summary - Beam Experiments.....	25
	2.4. Optimization of Actuator/Beam Configuration for Maximum Volume Velocity.....	25
	2.4.1. Beam Volume Velocity.....	26
	2.4.2. Effect of Actuator Location.....	26
	2.4.3. Effect of Boundary Conditions	29
	2.4.4. Effect of Actuator Length.....	29
	2.4.5. Effect of Actuator Thickness	31
	2.4.6. Multiple Actuator Configuration.....	32
	2.4.7. Effect of Beam Material Properties.....	34
	2.5. Conclusions	36
3.	Acoustic Plate Radiator Design Using PZT Actuators.....	37
	3.1. Introduction.....	37
	3.2. Acoustic Radiation by Flexural Modes in a Finite Plate.....	38
	3.3. Plate Actuation Using Piezoelectric Actuators - Litterature Survey	41
	3.4. FEM Approach - Effective Moment Computation	41
	3.5. Comparison Between Analysis and Experiment - Methodology	44
	3.6. Experimental Validation.....	45
	3.6.1. Plate Experimental Setup.....	46
	3.6.2. Experimental Validation - $140 \times 127 \times 1.6$ mm Lexan Plate....	47

3.6.3.	Experimental Validation - 100×115×0.76 mm Al. Plate	53
3.6.4.	Experimental Validation - 90×90×1.524 mm Al. Plate	56
3.6.5.	Summary - Experimental Validation	57
3.7.	Optimization of Actuator/Plate Configuration for Maximum Volume Velocity.....	57
3.7.1.	Effect of Actuator Size.....	58
3.7.2.	Effect of Actuator Thickness	59
3.7.3.	Conclusions.....	60
3.8.	Experimental Evaluation of Optimized Acoustic Plate Radiators	60
3.8.1.	Introduction	61
3.8.2.	100 × 115 × 0.76 mm Aluminum Plate - Plate 2.....	63
3.8.2.1.	High Actuator Voltage Tests - Plate 2.....	63
3.8.2.2.	Effect of Actuator Number and Actuator Polarity - Plate 2	67
3.8.2.3.	Harmonic Distortion - Plate 2.....	68
3.8.3.	90 × 90 × 1.52 mm Aluminum Plate - Plate 3.....	68
3.8.3.1.	High Actuator Voltage Tests - Plate 3.....	68
3.8.3.2.	Effect of Actuator Number and Actuator Polarity - Plate 3	71
3.8.4.	90 × 90 mm Aluminum Plates - Plates 4 to 15.....	71
3.8.4.1.	Mode Shapes and Equivalent Piston Velocity	72
3.8.4.2.	1.52 mm Thick Aluminum - 0.51-mm Actuator - Plates 3 to 7	72
3.8.4.3.	1.52 mm Thick Aluminum - 0.25-mm Actuator - Plates 8 to 11	75
3.8.4.4.	0.76 mm Thick Aluminum - 0.25-mm Actuator - Plates 12 to 15	77
3.8.5.	Summary - Plate Experimental Results.....	79
3.9.	Stresses in the Aluminum/Piezoceramic Radiator.....	79
3.10.	Fatigue Life of Aluminum/Piezoceramic Acoustic Plate Radiator.....	85
4.	Adaptive Tuning for Acoustic Plate Radiators.....	87
4.1.	Wide-Bandwidth Source Through Damping Control	87
4.2.	Adaptive Tuning Using Linear or Bending Stiffness Control.....	89
4.2.1.	Analysis.....	89
4.2.2.	Results	91
4.2.3.	Implementation.....	93
4.3.	Adaptive Tuning Using Variable In-Plane Frame Loading	97
4.4.	Adaptive Tuning Using Variable Embedded In-Plane Loading.....	101
4.5.	Adaptive Tuning Using Back Chamber Pressurization and Volume Variation	102

4.5.1. Adaptive Tuning Through Chamber Volume Variation	104
4.5.2. Adaptive Tuning Through Chamber Pressure Variation	108
4.6. Summary of Adaptive Tuning Methods	112
5. Conclusions	114
6. Follow-on Work Recommendations	119
6.1. Development and Demonstration of an Active Noise Cancellation System for the NASA Lewis Four-Foot Test Fan	119
6.2. Improvements to the Current PZT-Based Acoustic Plate Radiator Design to Satisfy Flight-Worthiness Standards	120
7. References	123
Appendix A. Installation of Piezoelectric Actuators - Standard Operating Procedures	127
Appendix B. Actuator Bonding	131
Appendix C. Properties of Piezoceramic Materials.....	133
Appendix D. Voltage Limitations for Piezoelectric Materials	136

LIST OF TABLES

Table 2.1.	Material properties.....	18
Table 2.2.	Natural frequencies - Lexan beam	19
Table 2.3.	Experimental damping and beam tip response - Lexan beam.....	19
Table 2.4.	Experimental damping and beam tip response - Lexan beam.....	20
Table 2.5.	Effect of actuator polarity on beam response - Lexan beam.....	22
Table 2.6.	Natural frequencies - Aluminum beam.....	22
Table 2.7.	Experimental damping and beam tip response - Aluminum beam ..	23
Table 2.8.	Effect of actuator polarity on beam response - Aluminum beam ...	23
Table 2.9.	Natural frequencies - Steel beam.....	24
Table 2.10.	Experimental damping and beam tip response - Steel beam	24
Table 2.11.	Effect of actuator polarity on beam response - Steel beam.....	24
Table 2.12.	Effect of boundary conditions on beam response - Constant beam thickness - Mode 1 - Steel beam	29
Table 2.13.	Effect of boundary conditions on beam response - Constant resonance frequency - Mode 1 - Steel beam.....	29
Table 2.14.	Material properties.....	34
Table 3.1.	Far-field acoustic intensity level as a function of plate mode number (with (1,1) mode as reference) - Low frequency and high frequency approximations.....	41
Table 3.2.	Natural frequencies - Lexan plate.....	48
Table 3.3.	Peak response at plate center and damping - Experimental and analytical data - Lexan plate	49
Table 3.4.	Linear and torsional spring constants at plate boundary.....	50
Table 3.5.	Natural frequencies - 100 × 115 × 0.76 mm aluminum plate.....	53
Table 3.6.	Peak response at plate center - Experimental and analytical data - 100 × 115 × 0.76 mm aluminum plate	53
Table 3.7.	Natural frequencies - 90 × 90 × 1.52 mm aluminum plate.....	56
Table 3.8.	Peak response at plate center - Experimental and analytical data - 90 × 90 × 1.52 mm aluminum plate	56
Table 3.9.	Velocity data for (1,1) mode - 90×90×1.52 mm aluminum plate...	57
Table 3.10.	Plate configurations for experimental study	61
Table 3.11.	Effect of actuator polarity on plate response - 100 × 115 × 0.76 mm aluminum plate.....	67
Table 3.12.	Harmonic distortion - 500 Hz Excitation - 100 × 115 × 0.76 mm aluminum plate.....	68
Table 3.13.	Effect of actuator polarity on plate response - Plate 3.....	71
Table 3.14.	90 × 90 mm aluminum plate configurations.....	71

Table 3.15.	(Equivalent piston velocity / velocity at plate center) for (1,1) mode - Plates 1,2, 3, and clamped and simply-supported plates	72
Table 3.16.	Harmonic distortion - Plates 9 and 10	77
Table 3.17.	Harmonic distortion - Plate 15	79
Table 3.18.	Summary of plate results - Plates 1 to 7	80
Table 3.19.	Summary of plate results - Plates 8 to 15	81
Table 3.20.	Physical properties of acoustic plate radiator - Stress analysis	82
Table 4.1.	3-dB and 10-dB bandwidths, and normalized response for plate radiator versus damping ratio	88
Table 4.2.	G , H , and J coefficients for simply-supported and clamped plates.	98
Table 4.3.	Beam buckling load versus beam thickness - Aluminum	99
Table 4.4.	Stresses in piezoceramic actuator versus beam thickness - Al.	101
Table 4.5.	Back chamber volumes for Lexan plates experiment.....	105
Table 4.6.	Back chamber volumes for Lexan plate experiment.....	106
Table 4.7.	Benefits and drawbacks of various adaptive tuning approaches ...	113
Table C.1.	Piezoceramic materials - Ranking by manufacturer	134
Table C.2.	Piezoceramic materials - Ranking by $d_{13} \times Y_{11}$	135
Table D.1.	Piezoceramic materials - Maximum allowable electrical field	137
Table D.2.	Maximum actuator voltage versus actuator thickness.....	136
Table D.3.	Maximum actuator AC RMS voltage versus actuator thickness....	138

LIST OF FIGURES

Figure 2.1.	Composite PZT actuator/beam configuration	8
Figure 2.2.	Free-body diagram with induced voltage V for a double-sided configuration	8
Figure 2.3.	Free-body diagram with induced voltage V for a double-sided configuration	9
Figure 2.4.	FEM discretization for a multiple PZT actuator/beam configuration	14
Figure 2.5.	Forced response for multiple PZT actuator/beam configuration	14
Figure 2.6.	Beam samples	15
Figure 2.7.	Beam experimental setup	16
Figure 2.8.	Beam experimental setup	17
Figure 2.9.	Beam setup	18
Figure 2.10.	Experimental model shapes - Lexan beam	21
Figure 2.11.	Mode shape for mode #2 - Lexan beam	21
Figure 2.12.	Beam analytical and experimental forced response - Summary	25
Figure 2.13.	Volume velocity and resonance frequency for simply-supported aluminum beam as a function of actuator location - Mode 1	26
Figure 2.14.	Volume velocity as a function of actuator location, and averaged 2nd derivative as a function of beam location for simply-supported aluminum beam - Mode 1	27
Figure 2.15.	Volume velocity and resonance frequency for clamped aluminum beam as a function of actuator location - Mode 1	28
Figure 2.16.	Volume velocity as a function of actuator location and averaged 2nd derivative as a function of beam location for clamped aluminum beam - Mode 1	28
Figure 2.17.	Deflection at beam center versus actuator length ratio for two actuator thicknesses (0.28 mm and 0.51 mm)	30
Figure 2.18.	Resonance Frequency versus actuator length ratio for two actuator thicknesses (0.28 mm and 0.51 mm) - Aluminum beam ...	30
Figure 2.19.	Deflection at beam center, deflection at beam center \times actuator thickness, And resonance frequency versus actuator thickness - Aluminum beam	32
Figure 2.20.	Deflection at beam center and resonance frequency versus combined actuator length - End Actuators - Aluminum beam	33
Figure 2.21.	Center and end actuator configurations- Aluminum beam	33
Figure 2.22.	Deflection at beam center and resonance frequency for several actuator combinations - Aluminum beam	34

Figure 2.23.	Deflection at beam center and resonance frequency for lexan, aluminum, and steel beams.....	35
Figure 2.24.	Deflection at beam center and resonance frequency for aluminum carbon, and titanium beams.....	36
Figure 3.1.	Coordinate system for plate radiation.....	40
Figure 3.2.	Plate radiator in frame with PZT actuator bonded at center.....	42
Figure 3.3.	Plate radiator with linear and torsional spring boundary conditions.....	42
Figure 3.4.	Effective moments induced in the plate by the PZT actuators.....	43
Figure 3.5.	Stresses in the actuators.....	43
Figure 3.6.	Plate samples used for experimental validation.....	45
Figure 3.7.	Plate experimental setup.....	46
Figure 3.8.	Plate experimental setup.....	47
Figure 3.9.	Plate setup - Lexan.....	48
Figure 3.10.	Experimental mode shapes - Lexan plate.....	51
Figure 3.11.	Equivalent piston velocity response - Lexan plate.....	52
Figure 3.12.	Ratio of equivalent piston velocity response by maximum plate velocity - Lexan plate.....	52
Figure 3.13.	Experimental mode shapes - 100×115×0.76 mm aluminum plate..	54
Figure 3.14.	Equivalent piston velocity response - 100 × 115 × 0.76 mm aluminum plate.....	55
Figure 3.15.	Ratio of equivalent piston velocity response by maximum plate velocity - 100 × 115 × 0.76 mm aluminum plate.....	55
Figure 3.16.	Deflection at plate center and resonance frequency versus actuator size ratio - Aluminum plate.....	58
Figure 3.17.	Deflection at plate center and resonance frequency versus plate thickness - Aluminum plate.....	59
Figure 3.18.	Deflection at plate center, deflection at beam center × actuator thickness, and resonance frequency versus actuator thickness - Aluminum plate.....	60
Figure 3.19a.	Plate configurations for experimental study - Plates 4 to 9.....	62
Figure 3.19b.	Plate configurations for experimental study - Plates 10 to 15.....	63
Figure 3.20.	Velocity response at plate center versus actuator voltage - 100 × 115 × 0.76 mm aluminum plate.....	64
Figure 3.21.	Velocity at plate center versus actuator voltage - 100 × 115 × 0.76 mm aluminum plate.....	65
Figure 3.22.	Velocity response at plate center versus actuator voltage - 100 × 115 × 0.76 mm aluminum plate.....	66
Figure 3.23.	Velocity at plate center versus actuator voltage - 100 × 115 × 0.76 mm aluminum plate.....	66

Figure 3.24. Velocity at plate center and equivalent piston displacement versus actuator voltage - 100 × 115 × 0.76 mm aluminum plate ...	67
Figure 3.25. Actuator voltage and velocity at plate center versus frequency - Plate 3	69
Figure 3.26. Velocity response at plate center versus frequency - Plate 3	69
Figure 3.27. Plate resonance frequency versus actuator voltage - Plate 3	70
Figure 3.28. Velocity response at plate center versus actuator voltage - Plate 3...	70
Figure 3.29. Resonance frequency versus actuator voltage - Plates 3 to 7	73
Figure 3.30. Velocity response at plate center versus actuator voltage - Plates 3 to 7.....	73
Figure 3.31. Equivalent piston displacement versus actuator voltage - Plates 3 to 7.....	74
Figure 3.32. Resonance frequency versus actuator voltage - Plates 8 to 11	75
Figure 3.33. Velocity response at plate center versus actuator voltage - Plates 8 to 11.....	76
Figure 3.34. Equivalent piston displacement versus actuator voltage - Plates 8 to 11.....	76
Figure 3.35. Resonance frequency versus actuator voltage - Plates 12 to 15	77
Figure 3.36. Velocity response at plate center versus actuator voltage - Plates 12 to 15.....	78
Figure 3.37. Equivalent piston displacement versus actuator voltage - Plates 12 to 15.....	78
Figure 3.38. Tresca stresses in acoustic plate radiator	83
Figure 3.39. S-N curve for bending stresses with zero mean stress	86
Figure 4.1. Amplitude response for damping ratios of 0.5 % and 5 %	88
Figure 4.2. Phase response for damping ratios of 0.5 % and 5 %.....	89
Figure 4.3. Free-body diagram of a simply supported half-beam with linear springs.....	90
Figure 4.4. First mode resonance frequency versus linear spring stiffness	92
Figure 4.5. First mode resonance frequency versus torsional spring stiffness ..	92
Figure 4.6. Maximum variation of the first mode resonance frequency versus torsional spring location	93
Figure 4.7. Adaptive tuning using linear stiffness control.....	94
Figure 4.8. Adaptive tuning using bending stiffness control.....	94
Figure 4.9. Adaptive tuning using linear stiffness control.....	95
Figure 4.10. Adaptive tuning using in-plane plate loading	98
Figure 4.11. Plate resonance frequencies versus in-plane load	99
Figure 4.12. Force/Displacement diagram for aluminum plates of varying thicknesses	100
Figure 4.13. Adaptive tuning using in-plane plate loading	101

Figure 4.14. Adaptive tuning using back chamber pressurization and volume variation	103
Figure 4.15. Back chambers and plate used for adaptive tuning using chamber volume variation	105
Figure 4.16. Simplified model for plate and back chamber cavity	105
Figure 4.17. (Resonance frequency for plate/back cavity combination) / (Resonance frequency for plate alone) versus chamber depth - (1,1) mode - Lexan plates	107
Figure 4.18. (Resonance frequency for plate/back cavity combination) / (Resonance frequency for plate alone) versus chamber depth - (1,1) mode - Aluminum plates.....	107
Figure 4.19. Pressure chamber and plate used for adaptive tuning using chamber pressure variation.....	108
Figure 4.20. (Resonance frequency for plate/back cavity combination) / (Resonance frequency for plate alone) versus back chamber pressure - (1,1) mode - Lexan plate.....	109
Figure 4.21. (Resonance frequency for plate/back cavity combination) / (Resonance frequency for plate alone) versus back chamber pressure - (1,1) mode - 1.524-mm thick aluminum plate.....	109
Figure 4.22. Frequency response for several back chamber pressures - (1,1) mode - 1.52-mm thick aluminum plate. 10/93 test.....	110
Figure 4.23. Velocity response at resonance for several back chamber pressures - (1,1) mode - 1.52-mm aluminum plate. 10/93 and 12/93 tests.....	111
Figure 4.24. Resonance frequency for plate/back cavity combination versus back chamber pressure - (1,1) mode - 0.762-mm aluminum plate	111
Figure 4.25. Deflection at center of plate versus back chamber pressures for several plates.....	112

1. Introduction

Noise generated by fans and turbines in modern high-bypass aircraft engines is a major environmental issue in many communities surrounding airports. The enforcement of ever stricter noise regulations and the advent of new high-thrust, high-bypass ratio engines is leading engine manufacturers to look at new techniques such as active noise control to reduce aircraft engine noise.

1.1. General Background

Active Noise Control (ANC) is a method of reducing noise in a region of space using controlled acoustic sources to create a secondary sound field which when superimposed with the existing noise field results in an overall noise reduction. This concept has been known for many decades, but successful implementations were not reported until the late 1970's. In the last 15 years, technological advances in digital electronics have made the implementation of sophisticated digital control techniques inexpensive, leading to a rapid growth of the active noise and vibration control field (Stevens and Ahuja [1]).

Active noise control of aircraft engine noise is a relatively new field which offers great potential especially with new high-bypass ratio engines. Since the trend in newer and future engines is a combination of larger fans, lower blade passage frequency, and shorter ducts, the effectiveness of passive noise treatment is greatly reduced, making active noise control a very attractive option.

Several approaches are being investigated. One approach studied by United Technologies concentrates on reducing noise using active aerodynamic control [2,3,4]. Controlling trailing edge flaps on a stator were used to reduce noise generated by 2-D blade-gust interaction. A reduction in unsteady lift of over 10 dB was observed. Another approach studied by General Electric, SNECMA, and Virginia Polytechnic Institute uses canceling noise sources mounted on the fan duct perimeter to generate a sound field which cancels fan-generated noise. Work done at Virginia Polytechnic Institute by Thomas et. al. using a JT15D in a test stand has shown up to 16 dB noise reduction over a 60 degree angle about the engine axis [5,6] using loudspeakers mounted around the perimeter of the fan duct. Analytical tools were developed by Kraft and Kontos [7] from General Electric to allow performance assessment and system design of active control systems for aircraft engines. Initial results by Kraft and Kontos indicates that cases in which more than one radial mode is cut-on for the spinning mode of order of interest may require more than wall-mounted canceling sources. A sample case presented for a typical 1.52- meter turbofan engine with an $m = 5$ spinning mode at 600 Hz indicates that the equivalent piston source displacement for the wall mounted sources is of the order of 1.27 mm (0.05 inches). Power requirements may not be prohibitive, but weight reduction was found to be the most critical factor in transducer design and operation. Julliard et. al. from SNECMA [8,9] have carried out both analytical and experimental work. Tests performed on a scaled fan achieved a reduction of fan tone noise of up to 10-15 dB in a broad angular range.

As pointed out by Kraft [7], one of the critical issue is the generation of the very high canceling noise levels required. The canceling sources must be able to generate upward of 150-160 dB over a fairly wide frequency range. In addition, reliability must be high while power consumption and weight must be low. A variety of high-intensity, high-efficiency sources are now being investigated for this purpose such as piezoceramic-based actuators, fluidic actuators, and other electromechanical transducers.

Dungan at Virginia Polytechnic Institute designed and built a piezoceramic (PZT) based sound source for aircraft engine application [10]. The source consisted of a curved $140 \times 165 \times 1.6$ mm aluminum panel with $63 \times 38 \times 0.19$ mm PZT actuators bonded on each side of the panel. The panel was resiliently mounted on a duct section resulting in a high 5% damping ratio. The curvature of the panel was shown to greatly affect the resonance frequency and response of the panel.

The maximum RMS displacement achieved at the center of the panel at the resonance frequency of the (1,1) mode (1753 Hz) and for an actuator voltage of 100 V RMS can be estimated at approximately 0.007 mm. This displacement is over 500 times lower than the displacement required according to the study by Kraft [7].

1.2. Piezoelectric Actuators in Active Noise and Vibration Control

In recent years, much effort has been devoted to developing active noise and vibration control systems using piezoelectric actuators and sensors. Piezoelectric transducers have shown great promise for use as distributed actuators and sensors because they are inexpensive, space-efficient, light-weight, low-power, and are easily shaped and bonded or embedded to structural surfaces. In addition, the distributed nature of PZT actuators can be used to provide control with a minimum of spillover of the control energy into the uncontrolled modes of the system. Spillover usually occurs when discrete point control actuators are used due to their spectrally white characteristic in a spatial sense. Spillover reduces the control performance and further can lead to structural fatigue problems.

Piezoelectric materials exhibit an interesting phenomenon, whereby upon mechanical strain a measurable electric polarization (or voltage) proportional to the strain and vice-versa is produced. PZT materials have found common use in sensing devices such as sonar transducers and accelerometers. With the advances in ceramic technology PZT transducers have found widespread use in diverse range of applications including ultrasonic motors, surface acoustic wave (SAW) filters and micro-positioning controllers.

Bailey and Hubbard [11] demonstrated the possibility of using PZT actuators as active dampers for one-dimensional beams. Considerable vibrational decay times were demonstrated. Fanson and Chen [12], and Baz and Poh [13] demonstrated that a number of vibrational modes can be simultaneously controlled with reduced spillover of energy into higher modes. Crawley and de Luis [14] presented a rigorous analysis of stress-strain-voltage behavior of twin, symmetric surface-bonded and embedded PZT actuators in one-dimensional cantilever beams. Several important findings were demonstrated, including the

increased PZT actuator/structure coupling for stiffer and thinner bonding layers and relatively stiffer PZT materials compared to the structure. Also, it was demonstrated that when the bonding layer becomes negligibly thin, the shear stresses at the bonding layer/structure becomes uniform. Im and Atluri [15] further extended Crawley's work to include finite deformations in the presence of general loading of a bonded PZT actuator/beam configuration. Dimitriadis et. al. [16], investigated the behavior of surface bonded patches to an elastic plate and their use as vibration actuators to create a sound field around the plate. The analysis assumptions were a direct extension of Crawley's 1-D analog. It was demonstrated that modes can be selectively excited and that the geometry of the actuator shape markedly affected the modal distribution of the plate. The analysis was also extended to accommodate the use of piezoceramic actuators for ANC of structurally radiated/transmitted noise.

A generalized approach was presented by Kim and Jones [17], which took into consideration the thickness of the bonding layer in the analysis of the coupling between the PZT actuator and the structure. It was shown that an increase in the Young's Modulus of the actuators reduces the optimal thickness of the actuators and gives larger bending moments. The thickness of the bonding layer does not significantly affect the optimal thickness of the piezoceramic actuators; however, thicker bonding layers give lower bending moments. It was also shown that the damping and material properties of commercially available materials do not significantly influence either the optimal thickness of the actuators or the induced bending moment, given the bonding layer is thin with respect to the composite thickness.

Lee [18] generalized the idea of piezoceramic actuator shaping by developing a formulation of equations for a composite which incorporates the piezoelectric properties of materials into classical laminate theory. Two design parameters, namely actuator skew angle and polarization profile were discussed. Model sensors/actuators which detect/excite a single mode exclusively were investigated also by Lee and Moon [19].

In the area of noise control of structural radiated/transmitted noise, Jones and Fuller [20] demonstrated that successful noise reduction can be achieved by direct control of structural vibrations. This was achieved in an enclosed cylindrical shell by controlling shell vibrations using point actuators. Point actuators in practice are difficult to implement and tend to have serious spillover problems. As an alternative to point actuators, piezoceramic actuators/sensors have attracted considerable attention to attenuate structurally radiated/transmitted noise problems. Dimitriadis et. al. [21] have demonstrated that global attenuation of radiated sound can be achieved for on or off plate resonance frequencies. Both size and location of the actuator was demonstrated to affect the control performance. Wang and Fuller [22] have shown that control performance is affected by size, number, and location of actuators. It was found that increasing the number of actuators lead to only marginal improvement in sound attenuation at resonance which is usually dominated by the mode of the structure. In contrast, for off resonance cases, increasing the number of control actuators significantly improved the sound attenuation.

Clark and Fuller [23] employed PZT actuator and PVDF sensors to control the sound field from a vibrating panel. Two narrow strips of PVDF sensors were positioned on the plate such that the dominant observed response was due to the odd-odd and to a smaller extent to odd-even modes. It was demonstrated that PVDF sensors were very effective as microphones in providing error information necessary to reduce the far field sound radiation from the structure.

Fuller and Hanson [24] studied active control of interior noise in model aircraft fuselages using piezoceramic actuators. It was demonstrated that global attenuation of 10 to 15 dB of interior noise can be achieved with PZT actuators, irrespective of whether the shell system is vibrating at resonance frequencies or not. Active control of sound radiation of cylindrical shells with PZT actuators were studied by Sonti and Jones [25], and Lester and Lefebvre [26]. It was shown that controlling in-plane vibrations of cylindrical shells in general gives superior noise reduction especially at low frequencies. Liang and Rogers [27] proposed the use of corrugated piezoceramic actuator/sound radiators. These can be attached to a wall or inside an airplane fuselage to control the structural sound by active sound attenuation and can serve as distributed acoustic sources.

1.3. Current Investigation

The main goal of this study can be summarized simply: Is it possible, using piezoceramic-based plate radiators, to generate volume velocities that are high enough to be used for canceling aircraft engine fan noise ?

As a result, this study concentrates on maximizing volume velocity for a plate radiator using expertise gained at GE CRD in the last four years in designing piezoceramic-based sound sources for various applications.

To achieve this result, analytical models of beams and plates were developed and validated to allow optimization of transducer parameters to maximize volume velocity. In total, fifteen plates of various configurations were tested as well as several adaptive tuning methods to control the frequency bandwidth of plate transducers. The plate structure is excited at resonance so as to maximize volume velocity and hence acoustic output. Even though a number of researchers have investigated the fundamental issues encompassing the PZT actuator/structure coupling phenomena (Crawley and de Luis [14], Im and Atluri [15], Dimitriadis et. al. [16], and Kim and Jones [17]), the parameters influencing volume velocity have not been given much attention from a design standpoint. For this reason this work concentrates on optimizing the design parameters which affect volume velocity at resonance such as the bonding layer, structural thickness, PZT configuration, and material properties.

Chapter 2 reviews the models in existence for PZT/structure interface, and their influence on structural performance. The analytical formulation underlying resonance frequency and forced response for the PZT/structure configuration is presented. A further generalization

of the analysis of the PZT/beam configuration through FEM is also undertaken. Analytical results are compared against experimental results so as to validate the developed model. Optimization studies are then carried out to maximize volume velocity at resonance by varying PZT/structure parameters.

The following Chapter starts with a brief review on the theory of acoustic radiation from plates. Next, the vibration of PZT actuators/plate radiators is investigated using a Finite Element analysis. Current models for actuator/plate configurations are reviewed. The modeling assumptions for the FEM analysis are described and the analytical results are compared against experimental results so as to validate the developed model.

Actuator/plate optimization studies are then carried out, using the insight gained from the analytical work on beams (Chapter 2). In order to ensure structural integrity, the maximum dynamic stresses developed in the plate are investigated for the optimized radiator configuration. In addition, fatigue life for the plate is estimated based on "stress versus number of cycles to failure" curves published by ASTM. Experimental results on fifteen plates with different size, thickness, material, and with various actuators are presented.

Chapter 4 describes work done on adaptive tuning methods to increase the bandwidth of plate radiators. Several adaptive tuning concepts are discussed and analyzed at length and experimental results are presented using one of the most promising approach.

Finally, the concluding chapter reviews the work performed and makes recommendations for the next development phase.

2. Structural Actuation Using Piezoelectric Materials: Fundamental Principles - Beam Study

In the present chapter a brief review of piezoelectric constitutive relations for linear materials is presented. Next the existing models for actuator/structure interface and their influence on structural performance are reviewed. The present analytical formulation underlying resonance frequency and forced response for the actuator/beam configuration is presented. A further generalization of the analysis of the actuator/beam configuration through FEM is undertaken. Experimental results are presented and compared with the analysis. Optimization studies are then carried out to maximize volume velocity at resonance with actuator and beam thickness, actuator number and location, material properties and support conditions are presented.

2.1. Linear PZT Constitutive Relations

The strain $\{S\}$, stress $\{T\}$, electric field $\{E\}$ and the electric displacement $\{D\}$ have the following relationship for a linear Piezoelectric material.

$$\begin{aligned}\{T\} &= [C^E]\{S\} - [e]\{E\} \\ \{D\} &= [e]^T\{S\} + [\epsilon^S]\{E\}\end{aligned}$$

Here, $\{S\}$, $\{T\}$, $\{E\}$ and $\{D\}$ are represented component-wise as follows:

$$\begin{aligned}\{S\}^T &= \{S_1 S_2 S_3 S_4 S_5 S_6\} \quad ; \quad \{T\}^T = \{T_1 T_2 T_3 T_4 T_5 T_6\} \\ \{E\}^T &= \{E_1 E_2 E_3\} \quad ; \quad \{D\}^T = \{D_1 D_2 D_3\}\end{aligned}$$

Where S_1 through S_6 are the six independent strain components, T_1 through T_6 are the six independent stress components, E_1 , E_2 , E_3 , D_1 , D_2 , and D_3 are the 3 components of electric field and displacements respectively. $[e]$ is the piezoelectric stress constant and $[C^E]$ and $[\epsilon^S]$ represent the short-circuit stiffness and clamped dielectric permittivity (i.e. $\{S\}=0$) respectively.

Similarly, the open-circuit representation (i.e. $\{D\}=0$) takes the following form :

$$\begin{aligned}\{T\} &= [C^D]\{S\} - [h]\{D\} \\ \{E\} &= -[h]^T\{S\} + [\beta^S]\{D\}\end{aligned}$$

$[h]$ is the electromechanical coupling matrix. $[C^D]$ and $[\beta^S]$ represent the open-circuit stiffnesses and elastic constants, respectively.

It should be noted here that if one equation pair is known, then the other pair can be derived easily (Tiersten [28]). It should also be noted that the Poisson's ratio as well as the Young's Modulus depend on the electrical condition. Their variation can be significant depending on the variation of the piezoelectric coupling coefficient d_{31} .

2.2. Analytical Formulation for a PZT Actuator/Beam Configuration

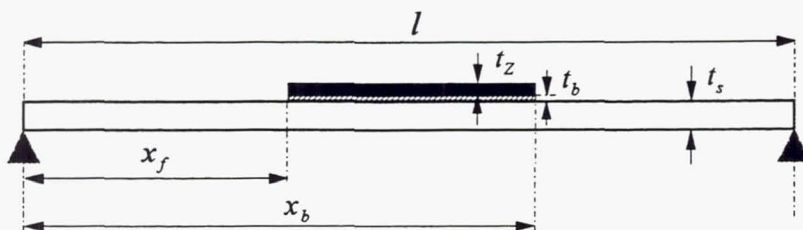
Baz and Poh [13] and Kim and Jones [17] investigated theoretically the effect of piezoceramic actuator thickness on the performance of one dimensional beams. They demonstrated that thicker actuators resulted in lower deflection amplitudes which was primarily attributed to the increase in the stiffness of the original beam. The optimal thickness of the one-sided surface-bonded piezoceramic actuator approaches the thickness of steel beams. This work however did not take into consideration the effect of size of the piezoceramic actuator, the overall beam parameters and the mode to be controlled or excited.

In this chapter, a fundamental investigation is carried out which provides a foundation for more general design guideline for piezoceramic plate actuators. The effect of size of the piezoceramic actuators, beam size, and material properties is studied so as to maximize volume velocity of the beam at a specified frequency of interest.

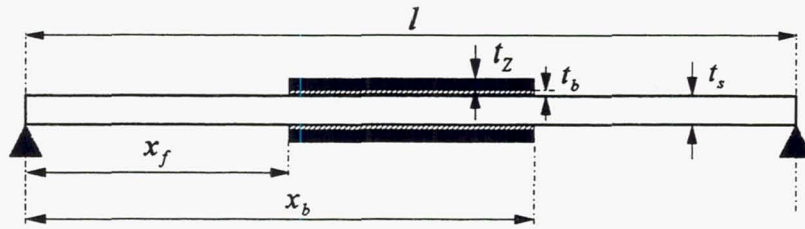
The work consists of two approaches : (i) an analytical approach to study a single piezoceramic actuator and beam configuration, (ii) A generalized finite element method (FEM) approach to study the effect of multiple segmented piezoceramic actuators. The analytical approach was initially adopted mainly because it sheds more light into the parameters governing actuator/beam interactions. Once the behavior for a single actuator/beam was understood a generalized FEM approach was adopted to investigate the effect of multiple segmented actuators in maximizing volume velocity.

2.2.1. Analytical Derivation of a Single PZT Actuator/Beam Configuration

A detailed formulation for a single piezoceramic actuator either bonded as a single-sided or double-sided configuration is presented in this section. Figure 2.1 shows a single-sided and a double-sided actuator/beam configuration compartmentalized into three segments.



(a) Single-sided configuration.



(b) Double-sided configuration.

Figure 2.1. Composite PZT actuator/beam configuration.

Governing Equations

A composite actuator/beam region is sandwiched between the two beam regions. The thickness of the bonding layer is also taken into consideration in the present analysis. Each segment is modeled as a Bernoulli-Euler beam and the overall beam equations are obtained by enforcing compatibility conditions at $x = x_f$ and at $x = x_b$ and enforcing the support boundary conditions at the ends of the beam.

The voltage is applied to the actuators so as to induce forces on the beam. As shown in Figure 2.2, in the case of the double-sided configuration the top and bottom actuators receive a voltage V which has a phase difference of 180 degrees.

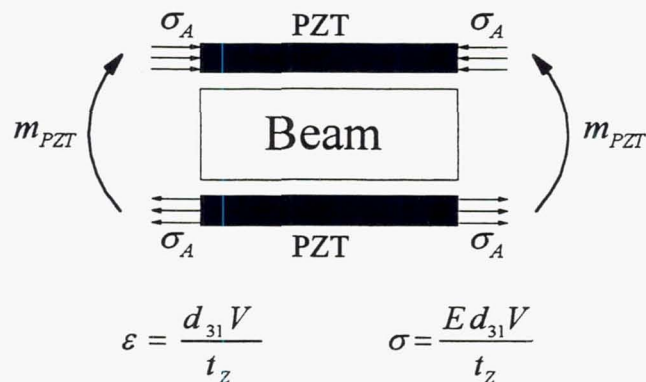


Figure 2.2. Free-body diagram with induced voltage V for a double-sided configuration.

This induces equal and opposite forces in the beam which result in a pure bending moment. In the case of a single-sided configuration however, the forces induced are a bending moment as well as an in-plane force. The effect of in-plane forces can be neglected in the current analysis, since in general in-plane forces do not significantly affect the bending motion of the beam.

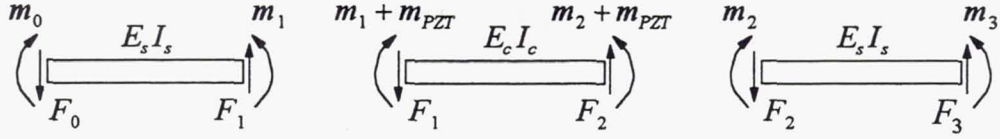


Figure 2.3. Free-body diagram with induced voltage V for a double-sided configuration.

Applying the governing equations of motion (damping is neglected for the time being, but will be included for the response analysis subsequently) to each segment of the beam (see Figure 2.3), we have:

$$\begin{aligned}
 E_s I_s \frac{\partial^4 U_1}{\partial x^4} + m_s \ddot{U}_1 &= 0 & 0 \leq x \leq x_f \\
 E_s I_c \frac{\partial^4 U_2}{\partial x^4} + m_c \ddot{U}_2 &= 0 & x_f \leq x \leq x_b \\
 E_s I_s \frac{\partial^4 U_3}{\partial x^4} + m_s \ddot{U}_3 &= 0 & x_b \leq x \leq l
 \end{aligned} \tag{2.1}$$

Here E_s and I_s represent the Young's Modulus and moment of inertia of the beam, I_c represent the moment of inertia of the composite actuator/beam structure, and m_s and m_c are the mass per unit length of the beam and of the composite structure respectively. U_1, U_2 , and U_3 are the vertical displacement components in the three segments, and l is the total length of the beam. Now I_s, I_c, m_s and m_c take the following form:

$$\begin{aligned}
 I_s &= \frac{b_s t_s^3}{12} \\
 I_c &= \frac{1}{E_s} \left[E_s I_s + \frac{1}{3} \alpha E_b b_b (\beta_{tb}^3 - \beta_{bb}^3) + \frac{1}{3} \alpha E_z b_z (\beta_{tz}^3 - \beta_{bz}^3) \right] \\
 m_s &= \rho_s t_s \\
 m_c &= \rho_s t_s + \alpha \rho_b t_b + \alpha \rho_z t_z
 \end{aligned} \tag{2.2}$$

Here b_s, b_b, b_z, t_s, t_b , and t_z are widths and thicknesses of the beam, bonding layer and actuator respectively. α takes the value of 1 or 2 depending on whether it is a single-sided or double-sided configuration. ρ_s, ρ_b and ρ_z are the densities of the beam, bonding layer and actuator respectively. The parameters $\beta_{tb}, \beta_{bb}, \beta_{tz}$ and β_{bz} are defined as:

$$\begin{aligned}
 \beta_{tb} &= \frac{t_s}{2} + t_b & ; & & \beta_{bb} &= \frac{t_s}{2} \\
 \beta_{tz} &= \frac{t_s}{2} + t_b + t_z & ; & & \beta_{bz} &= \frac{t_s}{2} + t_b
 \end{aligned} \tag{2.3}$$

The beam can be clamped, simply supported, or free depending on the type of support applied to the beam. Hence, depending on the support condition we have

$$\begin{aligned}
 U = \frac{\partial U}{\partial x} = 0 & \quad \text{for a clamped end} \\
 U = \frac{\partial^2 U}{\partial x^2} = 0 & \quad \text{for a simply supported end} \\
 \frac{\partial^2 U}{\partial x^2} = \frac{\partial^3 U}{\partial x^3} = 0 & \quad \text{for a free end}
 \end{aligned} \tag{2.4}$$

The compatibility conditions at the ends of each segment in the segmented beam must be met. At the interface $x = x_f$ the compatibility conditions for segments (1) and (2) (Figure 2.3) are as follows:

$$\begin{aligned}
 U_1 &= U_2 \\
 \frac{\partial U_1}{\partial x} &= \frac{\partial U_2}{\partial x} \\
 I_s \frac{\partial^3 U_1}{\partial x^3} &= I_c \frac{\partial^3 U_2}{\partial x^3} \\
 E_s I_s \frac{\partial^2 U_1}{\partial x^2} &= E_s I_c \frac{\partial^2 U_2}{\partial x^2} + m_{PZT}
 \end{aligned} \tag{2.5}$$

Here, m_{PZT} is the bending moment induced by the actuator and is given by;

$$m_{PZT} = \alpha b_z (\beta_{z^2}^2 - \beta_{bz}^2) \frac{E_z d_{31} V}{2 t_z} \tag{2.6}$$

The variables d_{31} and V represent the piezoelectric coupling coefficient and the applied voltage respectively. The compatibility condition at the interface $x = x_b$ between the segments (2) and (3) are as follows;

$$\begin{aligned}
 U_2 &= U_3 \\
 \frac{\partial U_2}{\partial x} &= \frac{\partial U_3}{\partial x} \\
 I_c \frac{\partial^3 U_2}{\partial x^3} &= I_s \frac{\partial^3 U_3}{\partial x^3} \\
 E_s I_s \frac{\partial^2 U_3}{\partial x^2} &= m_{PZT} + E_s I_c \frac{\partial^2 U_2}{\partial x^2}
 \end{aligned} \tag{2.7}$$

The voltage applied to the actuators induces the end moment m_{PZT} . Applying a harmonic excitation to the actuator results in a harmonic function for the forcing function m_{PZT} . The closed form solution for Equation 2.1 takes the following form;

$$\begin{aligned} U_1(x) &= C_1 \cos(\lambda_1 x) + C_2 \sin(\lambda_1 x) + C_3 \cosh(\lambda_1 x) + C_4 \sinh(\lambda_1 x) \\ U_2(x) &= C_5 \cos(\lambda_2 x) + C_6 \sin(\lambda_2 x) + C_7 \cosh(\lambda_2 x) + C_8 \sinh(\lambda_2 x) \\ U_3(x) &= C_9 \cos(\lambda_1 x) + C_{10} \sin(\lambda_1 x) + C_{11} \cosh(\lambda_1 x) + C_{12} \sinh(\lambda_1 x) \end{aligned} \quad (2.8)$$

where $\lambda_1^4 = \frac{m_s \omega^2}{E_s I_s}$, and $\lambda_2^4 = \frac{m_c \omega^2}{E_s I_c}$

Natural Frequencies and Mode Shapes

There are 12 unknown C coefficients in the above set of 3 equations. There are two boundary conditions each at the support conditions and four compatibility conditions each at the two beam-actuator/beam interfaces which yields a total of twelve conditions to solve for the 12 coefficients. The resulting matrix equation for the 12 unknown coefficients can be written as:

$$[A]\{C\} = \{B\} \quad (2.9)$$

Where $[A]$ is a 12×12 matrix involving trigonometric and hyperbolic coefficients, $\{B\}$ is a 12×1 vector containing the forcing function, and $\{C\}$ is a 12×1 vector representing the unknown coefficients C_1 through C_{12} . The resonant frequency of the combined actuator/beam configuration can be obtained by setting the determinant of the coefficient matrix to zero. The solution of the resulting transcendental equation leads to an expression involving trigonometric and hyperbolic terms of the form;

$$|[A]| = 0 \quad ; \quad f(\omega) = 0 \quad (2.10)$$

Equation 2.10 can be solved using Newton Raphson's method for ω , the natural frequency of the system.

The mode shape can be determined by setting one of the coefficients, namely C_{12} , to unity. This way the system matrix in the absence of a forcing function can be written as:

$$[A]\{C\} = 0. \quad (2.11)$$

which can be modified to

$$[A_M]\{C_M\} = \{f_M\} \quad (2.12)$$

$\{C_M\}$ is a vector containing coefficients C_1 through C_{11} , $\{f_M\}$ is the 11×1 right-hand side vector generated by setting $C_{12} = 1$, and $[A_M]$ is an 11×11 sub-matrix of $[A]$. M is the mode at which these coefficients are calculated.

Solving the matrix equation 2.12, we can determine the unknown coefficients C_1 through C_{11} . Hence the mode shape from Equation 2.8 for the actuator/beam configuration can be written as:

$$\begin{aligned}\Psi_M(x) &= U_1(x) & 0 \leq x \leq x_f \\ &= U_2(x) & x_f \leq x \leq x_b \\ &= U_3(x) & x_b \leq x \leq l\end{aligned}\quad (2.13)$$

Forced Response at Resonance

The forced response of a composite actuator/beam for a harmonic excitation frequency ω is obtained by the superposition of the modes in the system as (Flugge [29]):

$$U(x, t) = \sum_{n=1}^N q_n \psi_n(x) e^{i\omega t} \quad (2.14)$$

Where q_n is a complex modal constant (for the n^{th} mode) to be determined. The generalized forcing function Q_n in modal space is given by

$$Q_n(t) = \int_0^l P(x, t) \psi_n(x) dx + \int_0^l M(x, t) \psi'_n(x) dx \quad (2.15)$$

Where $P(x, t)$ and $M(x, t)$ are the forces and moments acting on the beam respectively. $\psi_n(x)$ and $\psi'_n(x)$ are the mode shape and the slope of the mode shape for the n^{th} mode respectively. Since the volume velocity is a maximum at resonance, we are interested in the response of the beam when driven at its natural frequency. Since undamped systems exhibit unbounded response at resonance, damping is introduced at this point in the system. It is assumed that the composite actuator/beam configuration exhibits uniform structural damping. Starting with the Lagrange's equations of motion for the whole system, and decomposing them into modal space, we obtain;

$$\ddot{q}_n + 2\xi_n \omega_n \dot{q}_n + \omega_n^2 q_n = \frac{Q_n}{m_n} \quad (2.16)$$

Where ξ_n is the structural damping coefficient for the overall structure, ω_n is the natural frequency for the n^{th} mode and m_n is defined as;

$$\begin{aligned}
m_n &= \int_0^l \mu \Psi^2(x) dx \\
&= \int_0^{x_f} \mu_s U_1^2(x) dx + \int_{x_f}^{x_b} \mu_c U_2^2(x) dx + \int_{x_b}^l \mu_s U_3^2(x) dx
\end{aligned} \tag{2.17}$$

where μ_s and μ_c are the mass per unit length for the beam and for the actuator/beam composite respectively.

The forcing function given in Equation 2.15 takes the following form for the composite actuator/beam configuration:

$$Q_n(t) = [\psi'_n(x_b) - \psi'_n(x_f)] m_{PZT} e^{i\omega t} \tag{2.18}$$

The steady state response is then given by;

$$U_{ss}(x, t) = \sum_{n=1}^N \frac{(\psi'_n(x_f) - \psi'_n(x_b)) \psi(x) m_{PZT} e^{i(\omega t - \varepsilon_n)}}{m_n \omega_n^2 \sqrt{\left(1 - \frac{\omega^2}{\omega_n^2}\right)^2 + \left(2\xi_n \frac{\omega}{\omega_n}\right)^2}} \tag{2.19}$$

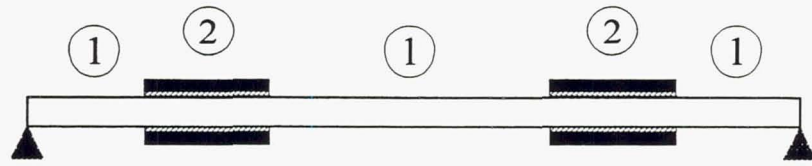
where

$$\varepsilon_n = \tan^{-1} \left[\frac{2\xi_n \frac{\omega}{\omega_n}}{\left(1 - \frac{\omega^2}{\omega_n^2}\right)} \right] \tag{2.20}$$

Where ω is the frequency of excitation, ξ_n is the structural damping ratio of the n^{th} mode and ω_n is the n^{th} natural frequency.

2.2.2. Generalized FEM Approach

The above mentioned analytical approach provides much insight into the parameters governing actuator/beam interactions. Such an analysis however, becomes quite cumbersome when dealing with segmented actuator/beam configurations. It is expedient at this point to resort to a generalized FEM approach in analyzing such configurations. The general purpose FEM package ANSYS [30] is used here.



(a) Multiple PZT actuator/beam configuration.



(b) FEM discretization of multiple PZT actuator/beam configuration for natural frequency analysis.

Figure 2.4. FEM discretization for a multiple PZT actuator/beam configuration.

Figure 2.4 depicts a FEM discretization of a multiple actuator/beam configuration where "STIF-3" beam elements were used. The actuator/beam composite region was modeled using the effective material properties defined as follows:

$$I_c = \frac{1}{E_s} \left[E_s I_s + \frac{1}{3} \alpha E_b b_b (\beta_{tb}^3 - \beta_{bb}^3) + \frac{1}{3} \alpha E_z b_z (\beta_{tz}^3 - \beta_{bz}^3) \right] \quad (2.21)$$

$$\rho_c = \rho_s + \frac{1}{t_s} (\alpha \rho_b t_b + \alpha \rho_z t_z)$$

Here α and β 's are the same as in Equation 2.2. The Young's Modulus and thickness of the composite section are the same as the bare section. The smeared moment of inertia and the density of the composite section however, is calculated according to the above equation. The natural frequency of the multiple segmented beam is found by employing the "KAN = 2" option. The response analysis is then performed at the previously computed natural frequency by employing the "KAN = 3" option, assuming that structural damping is present uniformly throughout the structure. The bending moments induced by the actuator segments are applied at the ends of the actuator segments as shown in Figure 2.5 and are computed using Equation 2.6.

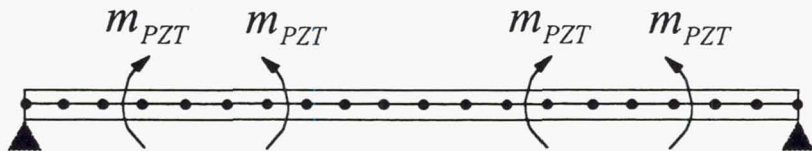


Figure 2.5. Forced response for multiple PZT actuator/beam configuration.

The bending moments in each segment can be either positive or negative depending on the polarity of the voltage applied to the actuators. The volume velocity is computed from the deflection which is easily obtained using ANSYS post processing features.

2.3. Experimental Validation - Beam Experiments

The main goal of the beam experiments was the validation of the analytical and FEM models. The beams were made using several materials: Lexan, aluminum, and steel with dimensions 300 mm × 30 mm as shown in Figure 2.6.

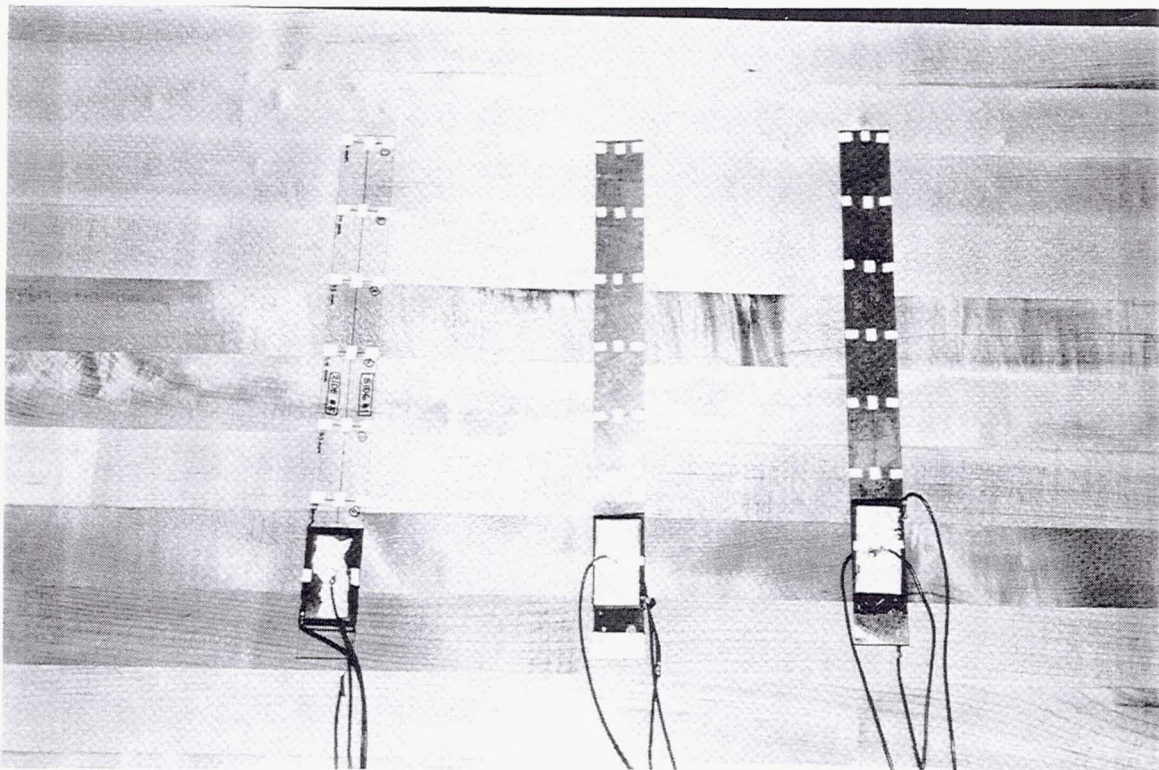


Figure 2.6. Beam samples.

Actuators were bonded at one end and on each side of each beam using the GA-2 epoxy adhesive as described in details Appendices A and B. 49 × 25 × 0.28 mm PKI-500 actuators from Piezo Kinetics were used for the tests. The PKI-500 material is a standard middle-of-the-line material with a dielectric constant d_{31} of $-175 \cdot 10^{-12}$ m/V and a Young's Modulus of $7.1 \cdot 10^{10}$ N/m².

2.3.1. Experimental Setup

The experimental setup is shown in Figures 2.7 and 2.8. The beam actuators are powered using a signal generator, amplifier, and matching network combination. The actuators are

connected "out of phase" such that they generate a pure bending motion in the beam. A laser velocimeter measures the beam velocity at 21 points on the beam (7 rows of 3 points). Both actuation and beam velocity signals are sent to a B&K 2032 FFT analyzer connected to a modal analysis workstation running the STAR modal analysis software. All test data are stored on the computer for archiving and analysis. The beam is clamped vertically in a vise to simulate a clamped boundary condition.

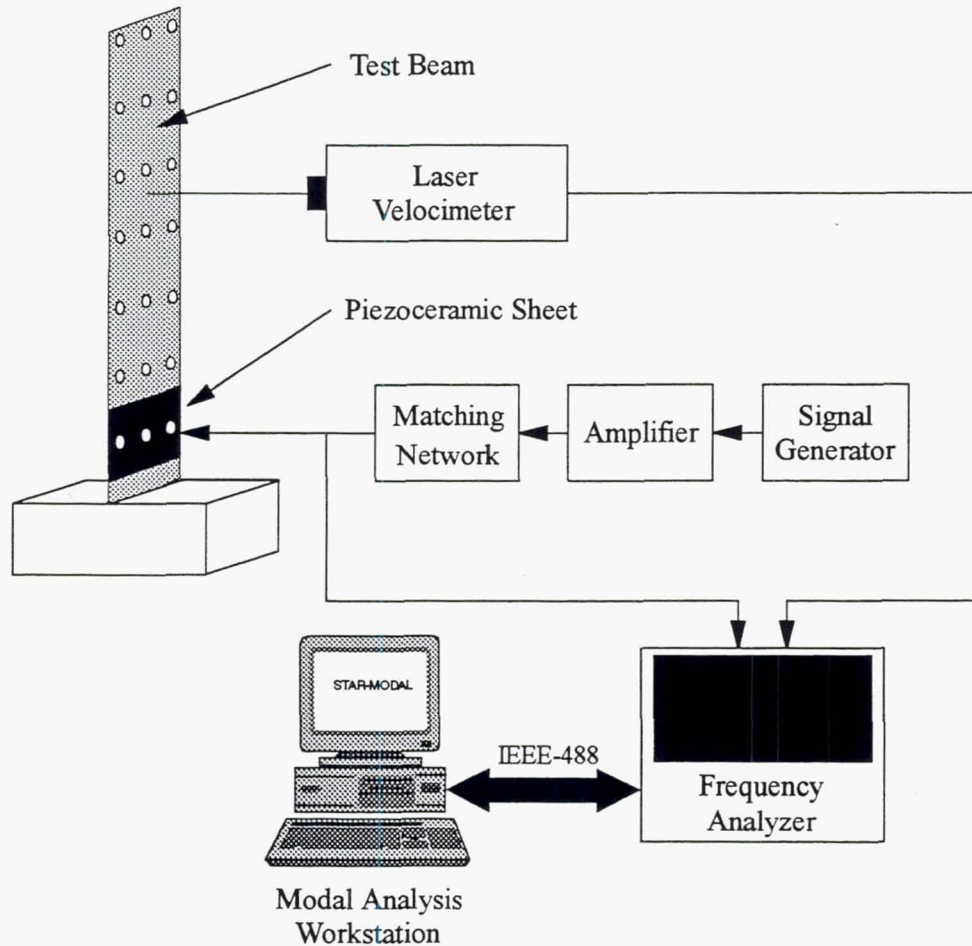


Figure 2.7. Beam experimental setup.

Two typical tests were carried out: Impulse hammer testing and self-powered testing. In the case of impulse hammer testing, the actuators are disconnected and an impulse hammer technique is utilized to identify the dynamic characteristics of the beam. In the self-powered test, broadband noise is sent to the actuators to extract the beam modal characteristics. The first method allows all modes to be identified but is difficult to implement, especially with light-weight, lightly-damped beams. The self-powered method is usually more accurate and easier to implement, but might miss some of the higher-order modes and prevent a full analysis of the system since the excitation moment provided by the actuators is unknown. The actuators were bonded near the clamped end of the beam

so that all lower modes of interest were excited. The self-powered method was used in most of the test cases.

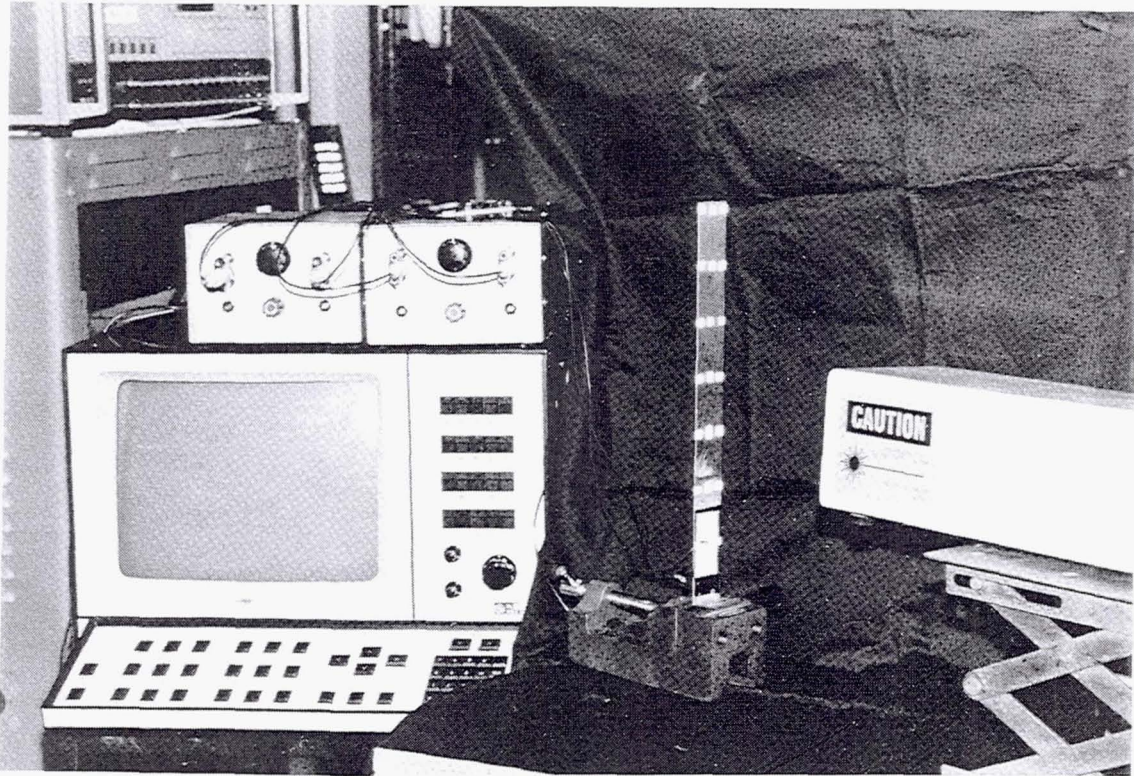


Figure 2.8. Beam experimental setup.

The purpose of the matching network is to boost up the amplifier voltage to a level usable by the actuator. The audio amplifiers used for these tests are designed to power mostly resistive and inductive loads at fairly low voltages. Piezoceramic actuators are typically low-resistance, low-power consumption capacitive loads which require high voltages. The matching network is essentially an audio transformer connected in such a way that it provides a step-up in voltage. Several matching networks were utilized for this project, including several custom-made networks, and two networks made by Wilcoxon Research, Inc.

2.3.2. Results

Testing was performed on Lexan, Aluminum, and Steel beams

2.3.2.1. Lexan Beam

The Lexan beam test was used to validate the analytical work and to develop the experimental methodology used for the rest of the tests. In addition, the stepped mechanical properties of the actuator/bond/beam composite as a result of the low stiffness

and density of Lexan allowed the validation of the analytical model with a high degree of confidence.

Two Lexan beams with dimensions $306 \times 32 \times 1.52$ mm were tested. One beam with no actuator and the other with actuators.

The location of the measurement points is shown in Figure 2.9. The GA-2 epoxy was used with a 0.076-mm copper electrode glued to back electrode of the actuator (electrode bonded to the beam) using a conductive silver epoxy bond. The bond thickness was mapped using a MAGNA-MIKE Hall-effect thickness probe. Accounting for the thickness of the copper strip, the bond thickness was quite irregular and varied between 0.08 and 0.18 mm with an average thickness of 0.13 mm.

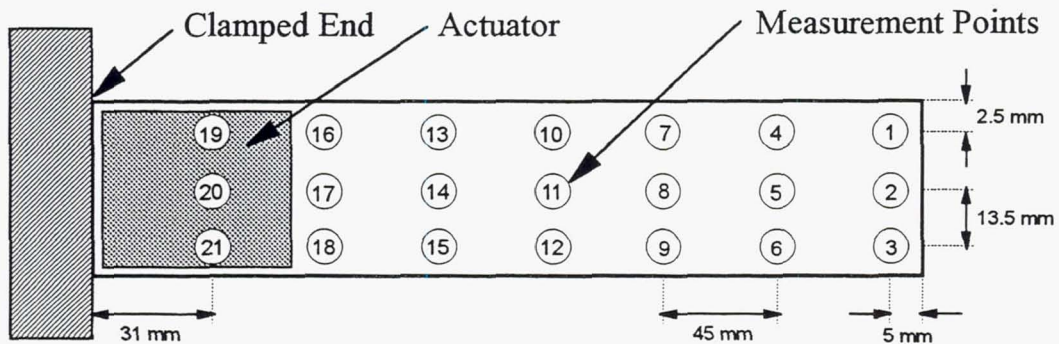


Figure 2.9. Beam setup.

Material properties for the beam, PZT actuator, and epoxy are given in the table below

	Density (kg/m ³)	Flexural Modulus (N/m ²)
Lexan	1,200	$2,300 \times 10^6$
Aluminum	2,700	$71,000 \times 10^6$
Steel	7,700	$195,000 \times 10^6$
GA-2 Epoxy	1,500	$6,000 - 4,000 \times 10^6$ *
PKI-500 PZT Actuator	7,600	$71,000 \times 10^6$

Table 2.1. Material properties

* depending on curing temperature.

As a result of the large difference in flexural modulus between the actuator and the beam (thirty times stiffer and six times heavier), the actuator mechanical properties dominate at the end of the beam. This is sufficient to alter the natural frequencies and mode shapes of the actuator/beam configuration compared to the bare beam.

Modal frequencies, damping, and amplitudes were estimated using three basic techniques: high resolution sine-sweep excitation, wideband random excitation, and narrowband random excitation using zoom analysis. The STAR MODAL modal analysis software was used to estimate modal parameters for the wideband random excitation tests. A 3-dB or 10-dB bandwidth method was used to estimate damping for the other two methods. 3,000 to 20,000 averages were taken when using the zoom analysis.

Natural Frequencies

The experimental and analytical natural frequencies for the beam with and without actuators are given below.

Mode #	Experimental (Hz)	Analytical with Actuator (Hz)	Analytical without Actuator (Hz)
1	5.05	4.89	3.58
2	29.4	27.9	22.4
3	69.5	67.7	62.8
4*	73.8		
5	126.1	121.2	123.1

* first torsional mode

Table 2.2. Natural frequencies - Lexan beam

Measured and analytical resonance frequencies are within 3 % to 5 % of each other. The actuators raise the resonance frequency by stiffening the beam since they are located next to the clamped end where the beam motion is small (inertial effects are low), but its curvature is high (bending stiffness effects are high). Similar to boundary condition effects, the actuator only affects the frequency of the lower order modes: 37 % difference for mode 1 while only 0.6 % difference for mode 5.

Damping Ratio and Displacement

Mode #	Sine Sweep		Wide band Random (STAR-MODAL)		Zoom Random	
	Damping (%)	Peak Disp. (mm/V)	Damping (%)	Peak Disp. (mm/V)	Damping (%)	Peak Disp. (mm/V)
1	0.86	1.36	--	--	--	--
2	0.88	0.195	0.96	0.236	0.74	0.227
3	--	--	1.20	0.0393	0.86	0.0423

Table 2.3. Experimental damping and beam tip response - Lexan beam

The damping ratio and beam displacement response at the tip center were measured experimentally using the three methods described above.

The analytical velocity and displacement magnitudes at the tip of the beam were calculated using the averaged measured damping factor. Analytical results are given in the table below:

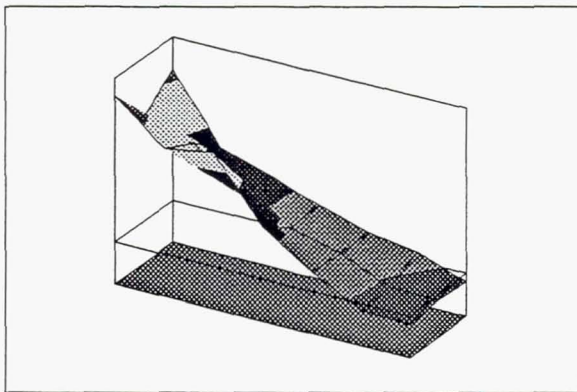
Mode #	Analytical Results		Experimental Results
	Damping (%)	Peak Disp. (mm/V)	Averaged Peak Disp. (mm/V)
1	0.86	1.11	1.36
2	0.85	0.183	0.219
3	1.03	0.0381	0.0408

Table 2.4. Experimental damping and beam tip response - Lexan beam

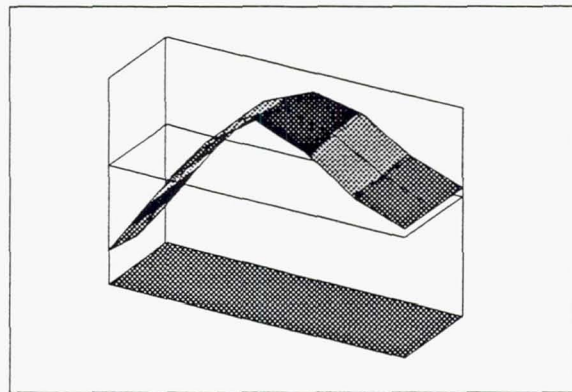
Measured and analytical responses are within 7 % to 22 % of each other.

Mode Shapes

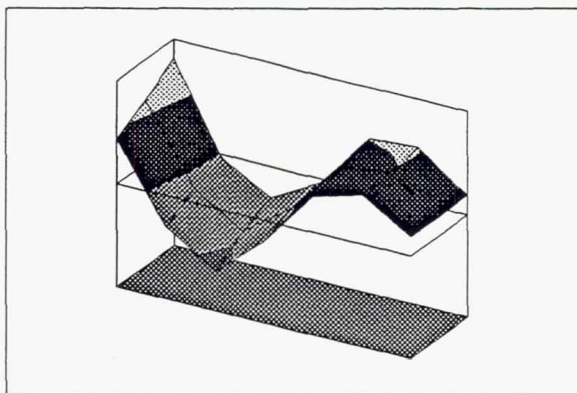
Measured mode shapes are as expected from simple beam theory as shown in Figure 2.10 which includes the first 4 beam modes and the first torsional mode (mode 4).



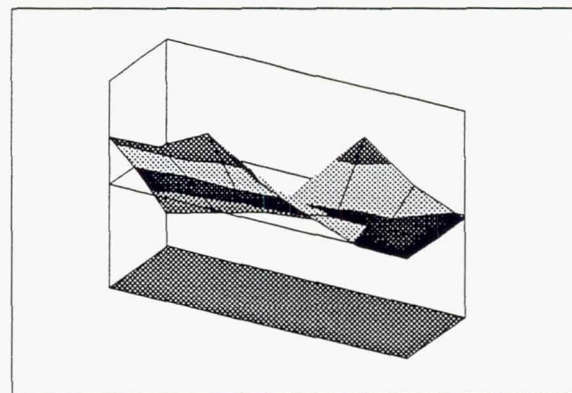
Mode 1



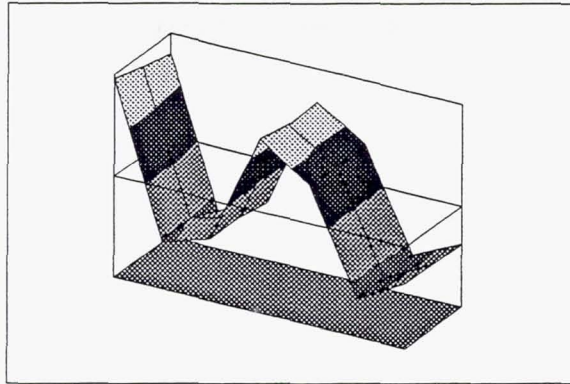
Mode 2



Mode 3



Mode 4



Mode 5

Figure 2.10. Experimental model shapes - Lexan beam.

The clamped part of the beam is on the right of each figure. Agreement between experimental and analytical mode shapes is very good as shown in Figure 2.11 for a beam with an actuator and for a bare beam. The stiffening effect of the actuator is clearly visible in the clamped-end region.

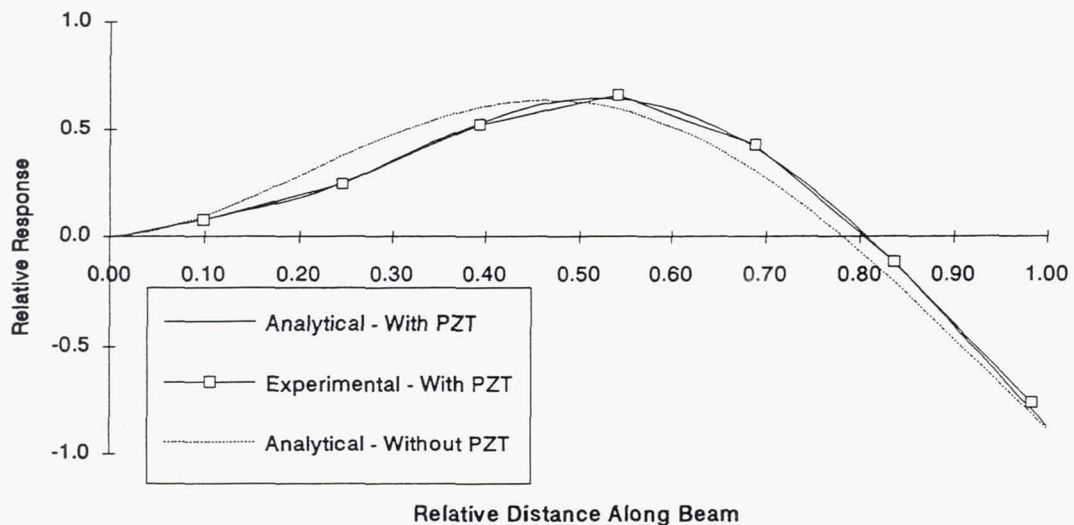


Figure 2.11. Mode shape for mode #2 - Lexan beam

Effect of PZT Actuator Number and Polarity

A series of tests was performed with each actuator (#1 and #2 in the table below) powered individually, in phase, and out of phase to evaluate the differences between actuators. This check, which was performed with all beam samples, is a good indicator of the quality and repeatability of the actuator bonding process.

Mode #	#1 Only	#2 Only	#1 and #2 Out of Phase	#1 and #2 in Phase
1	4.70	5.29	7.24	1.39
2	4.95	4.63	9.60	0.154
3	1.83	1.69	3.36	0.171

Table 2.5. Effect of actuator polarity on beam response - Lexan beam

The match between actuators is fairly good, but not perfect, due in part to imperfections in the bonds, actuator misalignment, and the fact that the mass and bending stiffness of the actuator are significant compared to the mass and stiffness of the beam.

2.3.2.2. Aluminum Beam

The aluminum beam design, fabrication, and testing procedure was the same as for the Lexan beam (exact beam dimensions: 294 × 29 × 0.76 mm). Bond thickness was mapped and averaged 0.11 mm to 0.19 mm. The bonding layer thickness now becomes more important as the flexural modulus of the bonding material is much less than the flexural modulus of the beam or the actuator.

Modal frequencies, damping, and amplitudes were estimated using the wideband random excitation and zoom random excitation methods described earlier.

Natural Frequencies

The experimental and analytical natural frequencies for the beams with and without actuators are given below.

Mode #	Exper. with Actuator (Hz)	Anal. with Actuator (Hz)	Exper. without Actuator (Hz)	Anal. without Actuator (Hz)
1	9.41	9.65	6.81	7.30
2	53.2	55.1	42.8	45.8
3	130.7	137.0	119.5	128.2
4	-	247.5	235	251.1
5	-	411.7	389.5	415.1

Table 2.6. Natural frequencies - Aluminum beam

Measured and analytical resonance frequencies are within 2 % to 6 % of each other. The effect of the actuators on the resonance frequency is not as pronounced as with the Lexan beam but still significant: 32 % difference for mode 1 and 0.8 % difference for mode 5.

Damping Ratio and Displacement

Experimental and analytical beam responses are given in the table below:

Mode #	Damping (%)	Analytical Peak Disp. (mm/V)	Experimental Peak Disp. (mm/V)
1	0.35	3.4	4.8
2	0.65	0.29	0.36
3	0.60	0.078	0.080

Table 2.7. Experimental damping and beam tip response - Aluminum beam

As with Lexan, analytical responses are lower than experimental responses with better agreement for the higher order modes. The difference for the first mode is mostly a result of the large experimental error due to poor estimates of the damping ratio and peak displacement at low frequencies and due to the high Q of the beam, rather than due to inaccuracies of the analytical model.

Mode Shapes

Measured mode shapes are again as expected from beam theory with very good agreement between analysis and measured data. The stiffening effect of the actuator is still clearly visible although not as pronounced as with the Lexan beam.

Effect of PZT Actuator Number and Polarity

The effect of actuator number and polarity is shown on the table below:

Mode #	#1 Only	#2 Only	#1 and #2 Out of Phase	#1 and #2 in Phase
2	14.6	16.9	30.1	2.46
3	9.16	11.6	21.4	2.55

Table 2.8. Effect of actuator polarity on beam response - Aluminum beam

Mode 1 data are not shown due to the very high measurement error. For mode 2 and mode 3, the match between actuators is good.

2.3.2.3. Steel Beam

The dimensions of the steel beam are $300 \times 30 \times 0.76$ mm with an average bond thickness of 0.18 mm.

Modal frequencies, damping, and amplitudes were estimated using the wideband random excitation and zoom random excitation methods.

Natural Frequencies

Mode #	Exper. with Actuator (Hz)	Anal. with Actuator (Hz)	Exper. without Actuator (Hz)	Anal. without Actuator (Hz)
1	8.22	8.36	6.94	6.84
2	46.3	46.8	44.7	42.9
3	120.9	122.2	125.5	120.0
4	234.6	236.6	246.5	235.2
5	395.3	398.0	-	395.3

Table 2.9. Natural frequencies - Steel beam

Damping and Displacement

Mode #	Damping (%)	Analytical Peak Disp. (mm/V)	Experimental Peak Disp. (mm/V)
1	0.36	2.57	3.05
2	0.52	0.202	0.238
3	0.72	0.0172	0.0191

Table 2.10. Experimental damping and beam tip response - Steel beam

Effect of PZT Actuator Number and Polarity

Mode #	#1 Only	#2 Only	#1 and #2 Out of Phase	#1 and #2 in Phase
1	7.26	5.83	14.1	0.93
2	11.3	10.0	17.4	2.02
3	2.40	2.01	4.79	0.42

Table 2.11. Effect of actuator polarity on beam response - Steel beam

Measured and analytical resonance frequencies are very close to each other. As expected, the effect of the actuators on the resonance frequency is less significant than for both the Lexan and aluminum beams: 22 % difference for mode 1 and 0.7 % difference for mode 5. Analytical and experimental responses are within 10 % to 16 % from each other with better accuracy for the higher order modes. Measured mode shapes are also in very good agreement with the analysis.

2.3.3. Summary - Beam Experiments

Experimental beam results are summarized in Figure 2.12 for Lexan, aluminum, and steel beams. Results show that the analysis can be used to predict resonance frequencies, forced response, and mode shapes with a very good degree of confidence.

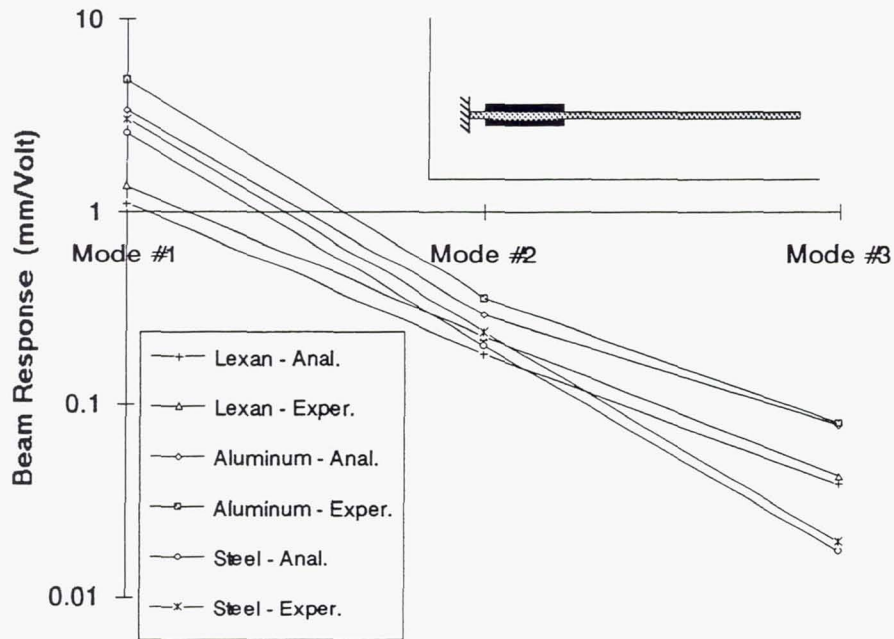


Figure 2.12. Beam analytical and experimental forced response - Summary

2.4. Optimization of Actuator/Beam Configuration for Maximum Volume Velocity.

The beam optimization study presented in this section provides a foundation for more general design guideline for piezoceramic plate actuators. Although one must be careful extrapolating beam results to plates, a thorough beam optimization casts much light on the behavior of PZT actuator/plate behavior. Another major reason for studying beams is the much faster turn-around time of the beam analytical solution compared to the plate FEM solution (a ratio of 200 to 1,000).

The emphasis in this section is on identifying the parameters which affect resonance frequency and volume velocity, and on finding the optimum combination of parameters which maximizes volume velocity for a given resonance frequency for the first beam mode.

Parameters optimized include: size, thickness, location, and number of the piezoceramic actuator, and beam material properties.

2.4.1. Beam Volume Velocity

Source strength for a plate radiator of size and frequency needed for aircraft engine noise cancellation is proportional to the plate volume velocity or equivalent piston velocity. Therefore, most beam results in this section are presented in terms of volume velocity Q_b (per beam unit width) which is defined as:

$$Q_b = \int_0^l U(x) dx \quad (2.22)$$

2.4.2. Effect of Actuator Location

The effect of actuator location on the response of a simply-supported and a clamped-clamped beams was studied using a $150 \times 29 \times 1.52$ mm aluminum beam with a double-sided $25 \times 25 \times 0.28$ mm PKI-500 actuator with a bond thickness of 0.13 mm. Material properties are as listed in Table 2.1.

Simply-Supported Beam

Volume velocity and resonance frequency as a function of actuator location are shown in Figure 2.13 for a simply-supported beam.

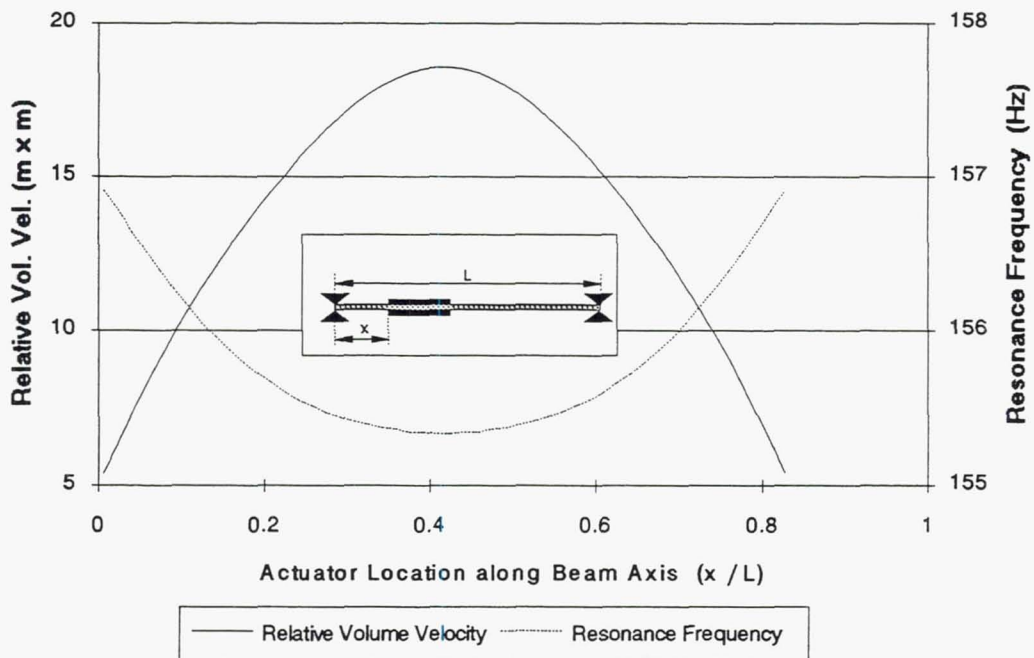


Figure 2.13 Volume velocity and resonance frequency for simply-supported aluminum beam as a function of actuator location - Mode 1.

The natural frequency is lowest as the actuator is located closest to the center of the beam as inertial effects becomes stronger due to the high beam deflection at its center. As the actuator is located closer to the ends of the beam, stiffness effects becomes more important and the resonance frequency rises. The volume velocity however reaches a maximum when the actuator is located at the center of the beam.

It is interesting to note at this point the similarity between the curvature of the beam (i.e. the second derivative of mode shape) and the volume velocity for the clamped-clamped actuator/Beam configuration. Figure 2.14 shows the curvature averaged over the actuator length as a function of beam location as well as the volume velocity as a function of actuator location. The maximum volume velocity occurs when the curvature of the beam is the highest, which is where the moment induced by the actuator couples best to the beam mode. This can also be inferred from the definition of the forcing function $Q_n(t)$ given in Equation 2.18 where the $[\psi'_n(x_b) - \psi'_n(x_f)]$ term can be looked at a "finite difference" approximation of the second derivative of the mode shape.

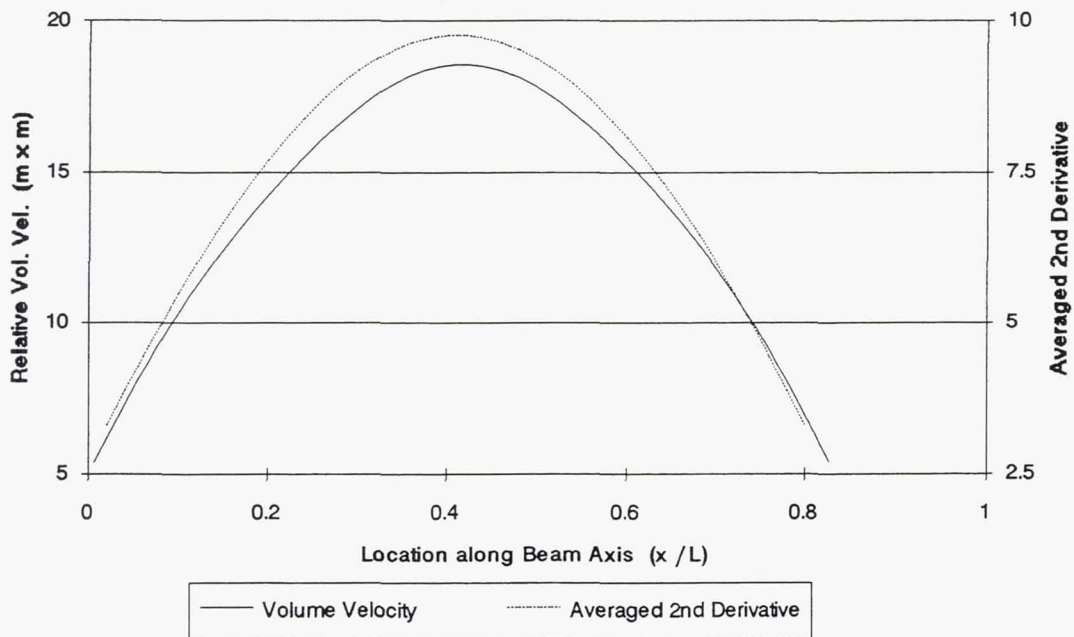


Figure 2.14 Volume velocity as a function of actuator location and averaged 2nd derivative as a function of beam location for simply-supported aluminum beam - Mode 1.

Clamped-Clamped Beam

Results for a clamped beam are shown in Figure 2.15. Again, the natural frequency is lowest as the actuator is located towards the center of the beam. Strong stiffness effects raise the resonance frequency when the actuator is located along the clamped edges where curvature is the highest and beam deflection (therefore inertial effects) is the lowest. As shown in Figure 2.16, the volume velocity follows the curvature of the beam and is

maximum when the actuator is located near a clamped edge or at the center of the beam (Figure 2.15).

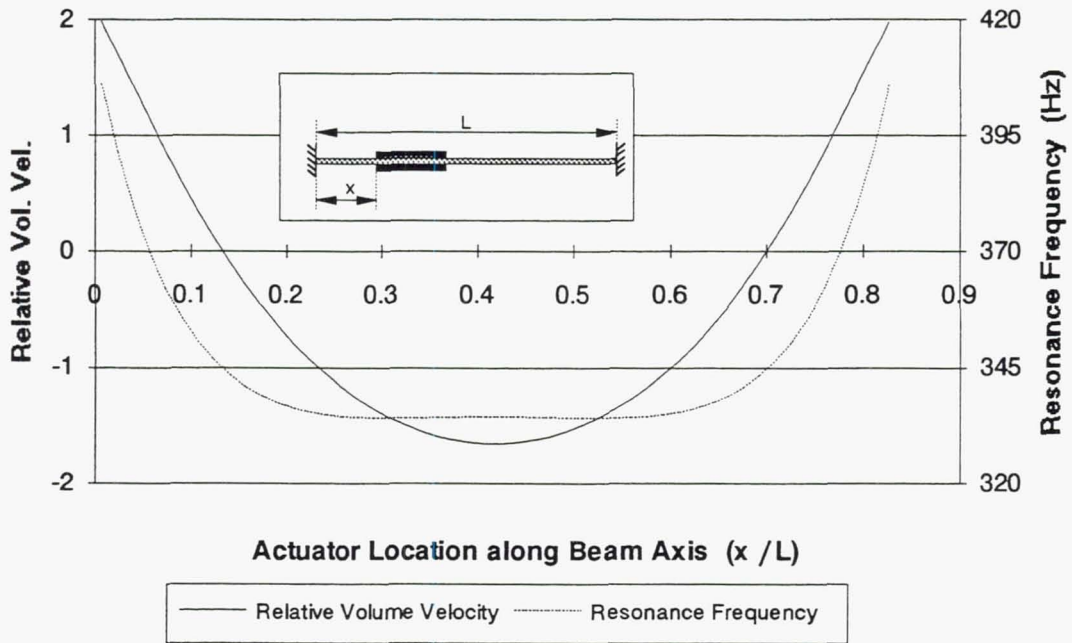


Figure 2.15 Volume velocity and resonance frequency for clamped aluminum beam as a function of actuator location - Mode 1.

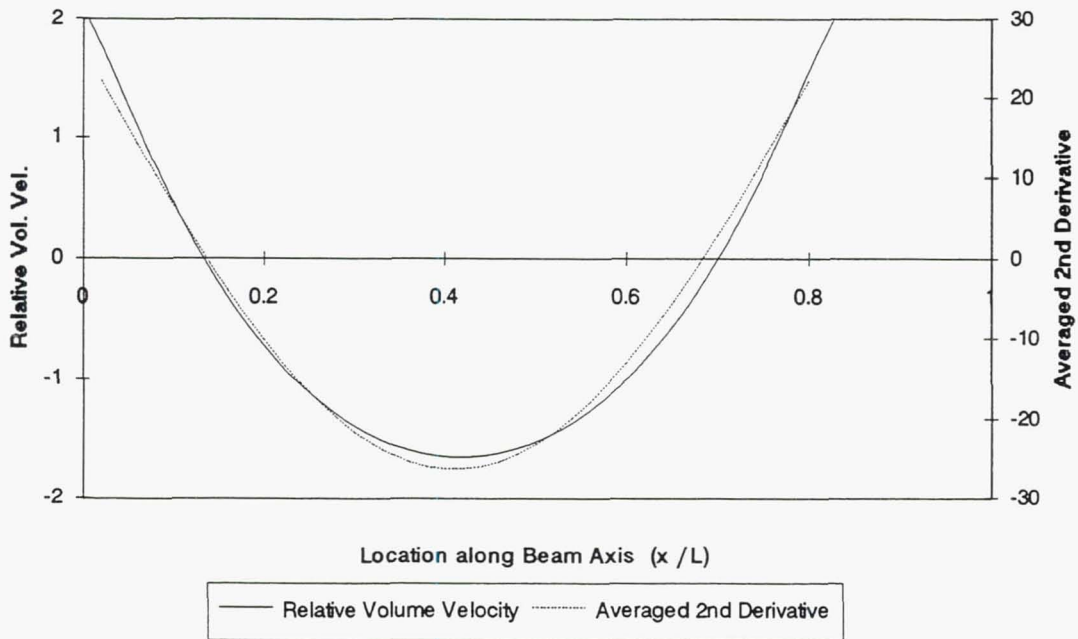


Figure 2.16 Volume velocity as a function of actuator location and averaged 2nd derivative as a function of beam location for clamped aluminum beam - Mode 1.

2.4.3. Effect of Boundary Conditions

Boundary conditions greatly affect the volume velocity and resonance frequency of plate and beam systems. Table 2.12 shows that the relative volume velocity for a simply supported steel beam is much higher than for a clamped beam of similar thickness. However, resonance frequencies are also very different. Since a specific resonance frequency is required for this application, comparison between boundary conditions should be performed at similar frequencies as shown in Table 2.13. In that case, beam thickness is adjusted so that the beams yield similar frequencies. The clamped beam now has a higher volume velocity than the simply-supported one. This simple result shows that boundary conditions are not extremely critical when dealing with a fixed frequency requirement.

Boundary Conditions	Beam Thickness (mm)	Resonance Frequency (Hz)	Relative Volume Velocity
Simply Supported	1.52	155	4.20
Clamped	1.52	334	1.66

Table 2.12. Effect of boundary conditions on beam response - Constant beam thickness - Mode 1 - Steel beam.

Boundary Conditions	Beam Thickness (mm)	Resonance Frequency (Hz)	Relative Volume Velocity
Simply Supported	3.924	405	0.96
Clamped	1.834	407	1.26

Table 2.13. Effect of boundary conditions on beam response - Constant resonance frequency - Mode 1 - Steel beam.

2.4.4. Effect of Actuator Length

Next, the optimum actuator length was determined by varying its length while maintaining all other parameters constant. A clamped aluminum beam similar to the beam used in Section 2.4.2. was used for this study with the actuator symmetrically located at the center of the beam. The actuator length ratio (ratio of actuator length to beam length) was varied from 25% to 92% .

Figure 2.17 shows the deflection at the beam center as a function of actuator length ratio for two actuator thicknesses (0.28 mm and 0.51 mm). The deflection at the beam center which is roughly proportional to the volume velocity and reaches a maximum for a ratio of about 65% for the 0.28-mm actuator, and about 75% for the 0.51-mm actuator. The

decrease in response at the higher ratios occurs because the actuator extends past the point where the second derivative of the mode shape changes sign (beam curvature changes from concave to convex).

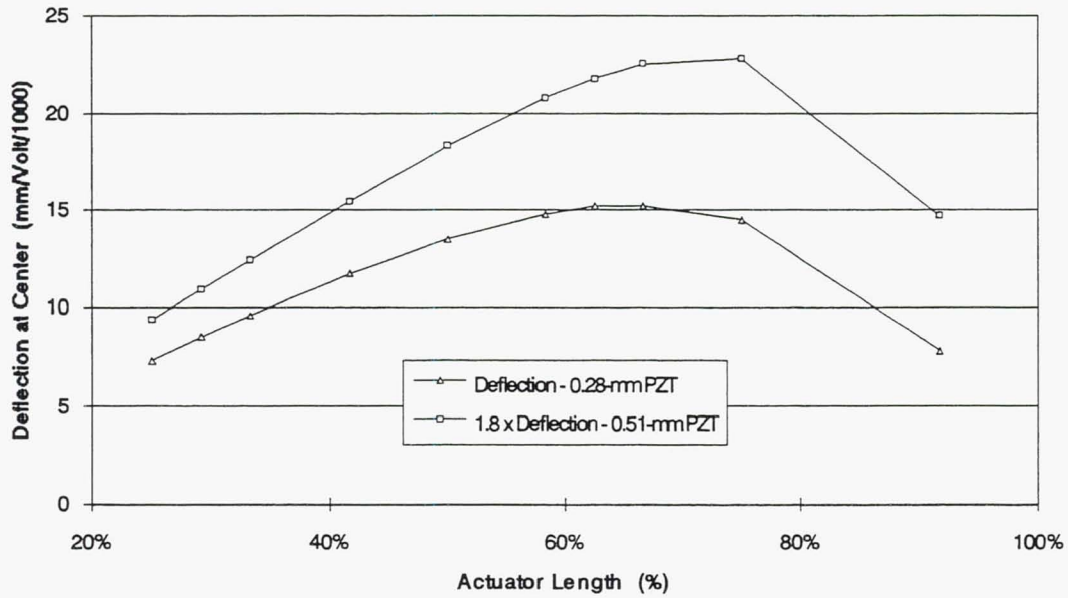


Figure 2.17 Deflection at beam center versus actuator length ratio for two actuator thicknesses (0.28 mm and 0.51 mm) - Aluminum beam.

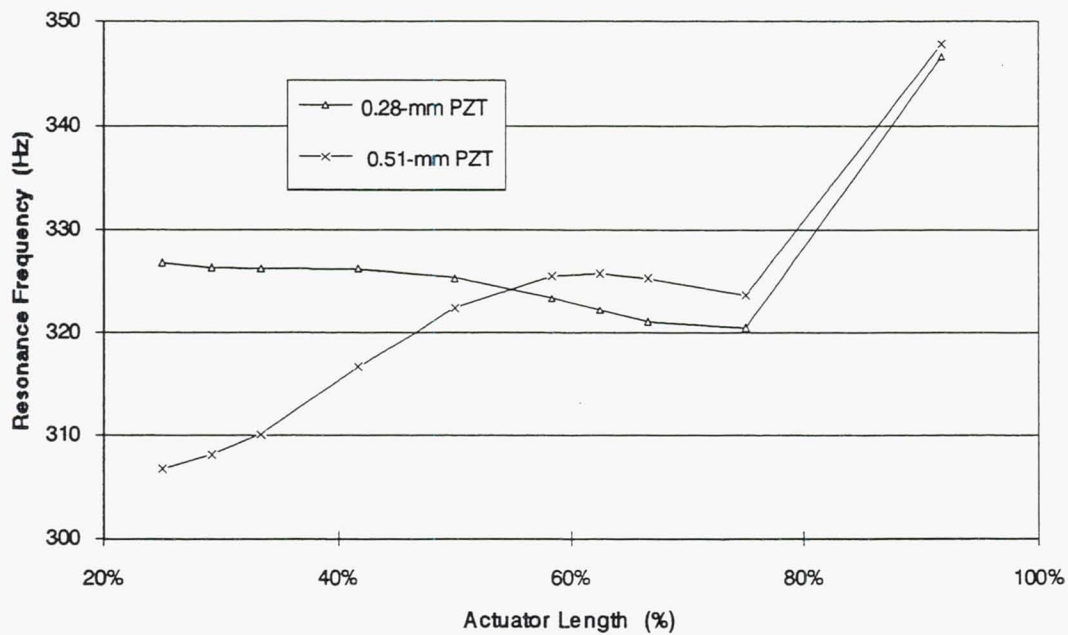


Figure 2.18 Resonance Frequency versus actuator length ratio for two actuator thicknesses (0.28 mm and 0.51 mm) - Aluminum beam.

The "1.8" multiplier in Figure 2.17 is applied to keep the (voltage/thickness) ratio across the actuator constant as the actuator voltage limit is proportional to its thickness (see Appendix D).

The resonance frequencies are shown in Figure 2.18. At high actuator length ratios, both resonance frequencies increase due to increased stiffening effects. At low actuator length ratios, the behavior of each beam differs substantially. For the thinner actuator, the mass and stiffness effects are of the same order and the resonance frequency is largely unaffected. For the thicker actuator, mass loading effects decrease the resonance frequency for short actuator lengths.

It should be pointed out that if the analysis was corrected to keep the resonance frequency constant, the beam deflections would be somewhat different than shown in Figure 2.17

2.4.5. Effect of Actuator Thickness

Increasing the actuator thickness t_z also increases the bending moment m_{PZT} induced by the double-sided actuator configuration as clearly seen by expanding the expression for m_{PZT} given in Equation 2.6.

$$m_{PZT} = E_z(t_z + t_s + 2t_b) b_z d_{31} V \quad (2.23)$$

However, since the structure is usually thicker than the actuator $t_s > t_z$, the increase in the moment is limited. The main advantage in using a thicker actuator is in the higher allowable actuator voltage V which is proportional to the actuator thickness.

The effect of actuator thickness is shown in Figure 2.19 for a clamped aluminum beam (similar to the beam in Section 2.4.2). For a constant voltage across the actuator, the beam deflection decreases as the actuator thickness increases. However, for a constant (voltage/thickness) ratio across the actuator which accounts for the fact that the actuator maximum voltage is proportional to actuator thickness, the (deflection \times actuator thickness) is maximum when the actuator thickness reaches 0.52 mm.

The effect of actuator thickness on the resonance frequency is that of a mass loading for thicknesses below 0.254 mm, and that of a stiffening for thicknesses above 0.254 mm. In addition, as in the previous section, the optimum actuator thickness would be slightly different (higher in this case) if the resonance frequency was kept constant.

A similar analysis was performed on a 1.52-mm Lexan beam yielding an optimum actuator thickness of 0.13 mm.

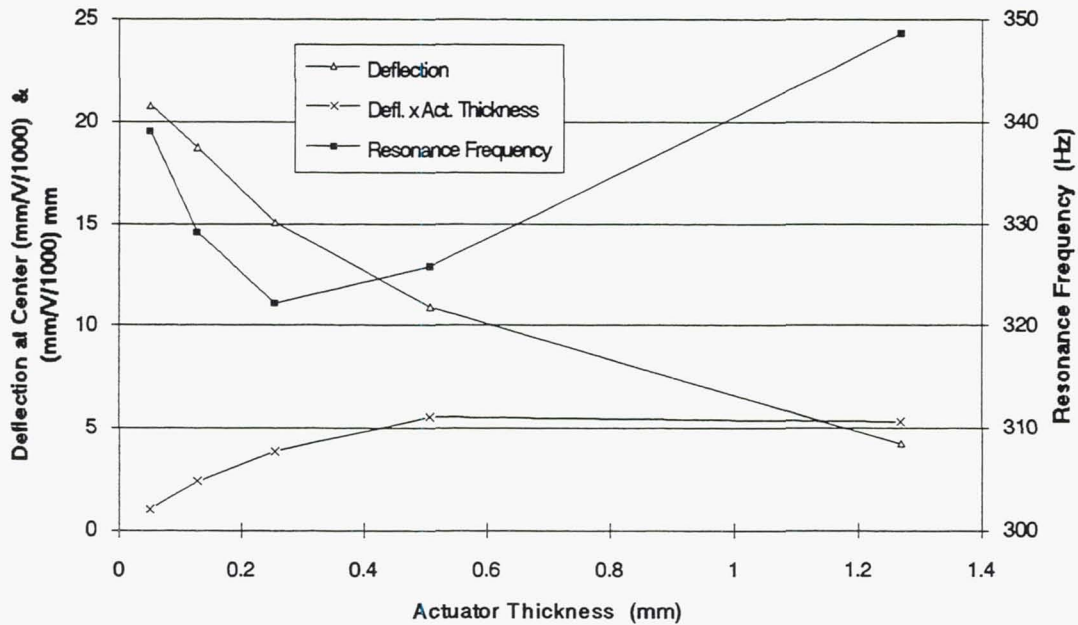


Figure 2.19 Deflection at beam center, deflection at beam center \times actuator thickness, and resonance frequency versus actuator thickness - Aluminum beam.

2.4.6. Multiple Actuator Configuration

A multi-segmented actuator approach was considered next order to take advantage of the change in curvature between the center of the beam and the clamped ends (see Figure 2.16). The clamped aluminum beam of Section 2.4.2 was used for this study.

End Actuators Only

Figure 2.20 shows the deflection and resonance frequency of the clamped aluminum beam as a function of "combined actuator length". Each double-sided actuator is positioned with one end at a fixed distance $b = 6.25$ mm to the clamped end. As the size of the actuators increases, they extend towards the center of the beam. The combined actuator length is defined as the ratio of the length of both actuators to the length of the beam: $(2a/L)$. The optimum "combined actuator length" is about 40% with the deflection dropping for larger actuators as they extend past the inflexion point of the beam mode shape.

Center and End Actuators

Figure 2.21 shows three different configuration compared: (1) Central actuator only (actuator length: 58%), (2) two end actuators (combined actuator length: 25%), (3) and both central and two end actuators.

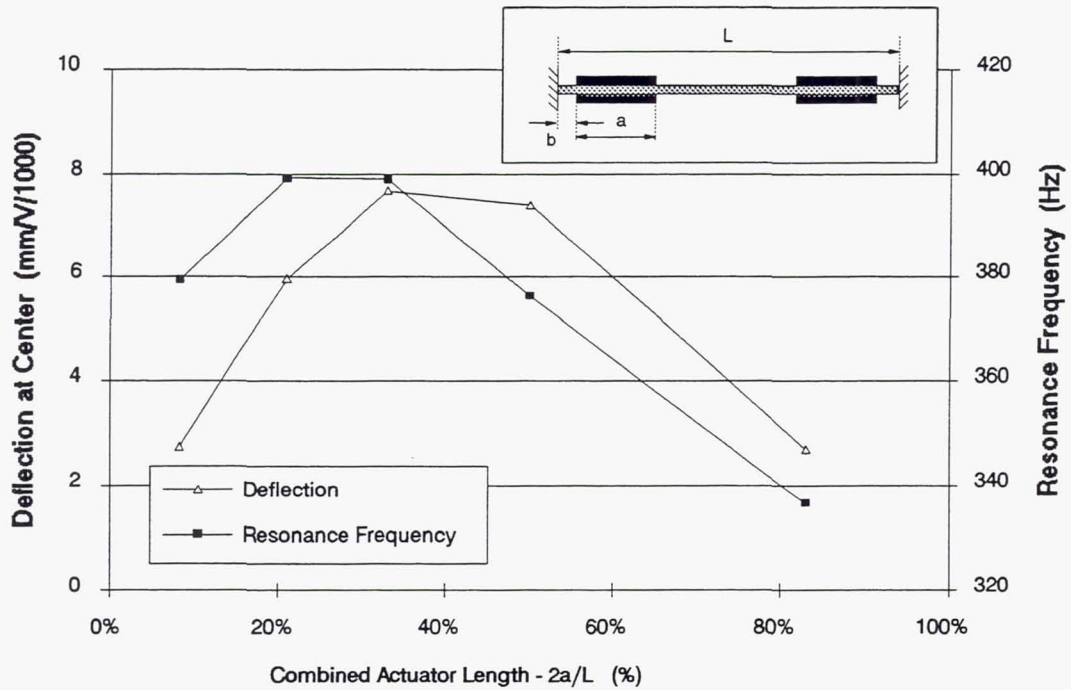


Figure 2.20 Deflection at beam center and resonance frequency versus combined actuator length - End Actuators - Aluminum beam.

Each configuration is fairly close to the optimum one and was obtained after optimizing the response for a beam with center and end actuators. The two polarity combinations between end and center actuators were tried to ensure that the proper polarity was used.

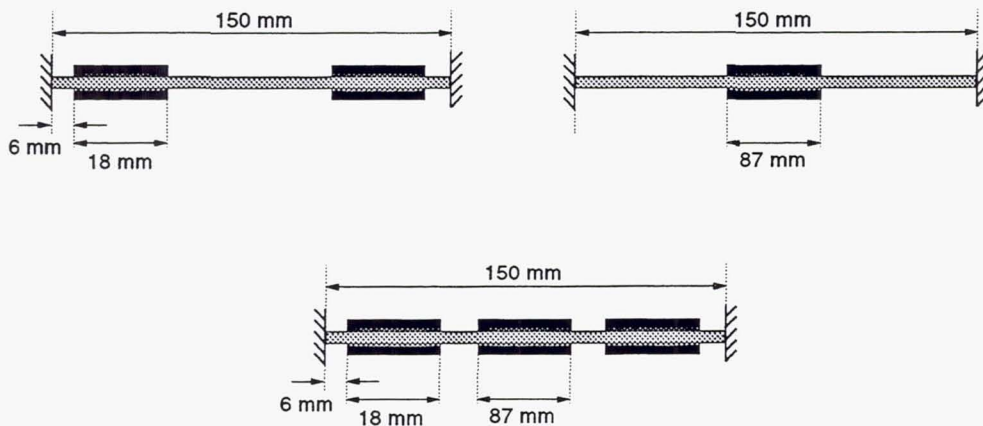


Figure 2.21 Center and end actuator configurations- Aluminum beam.

As expected, the central actuator configuration has the lowest resonance frequency (high inertial effects), while the end actuator combination has the highest (high stiffness effects). The central and end actuator combination has the highest deflection: 16.4 mm/V/1000,

although it is 24% lower than the sum of the two other configurations and only 11 % higher than the central actuator combination (without the frequency correction).

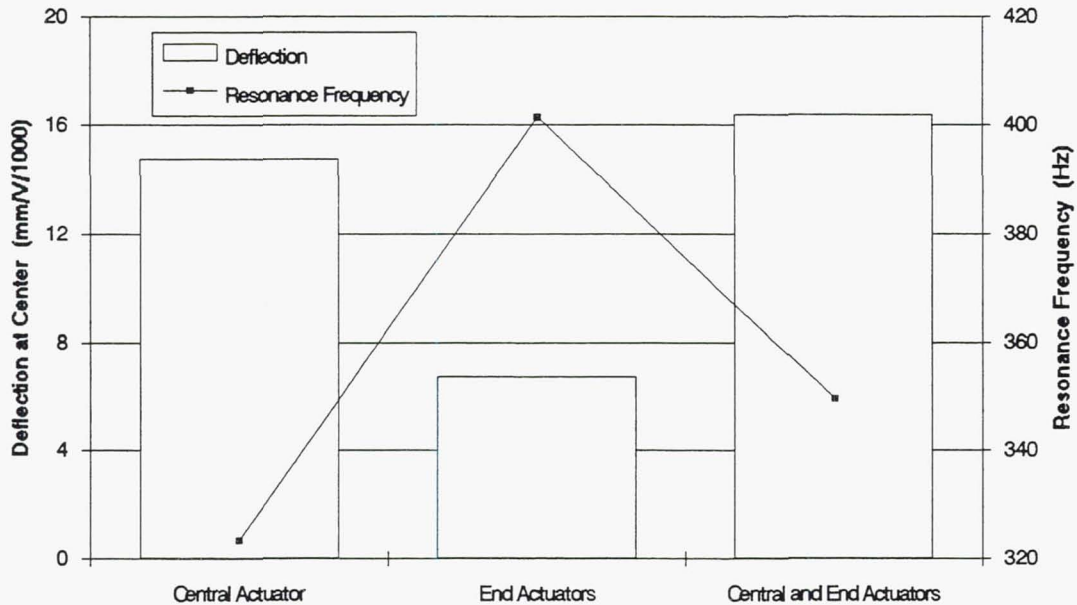


Figure 2.22 Deflection at beam center and resonance frequency for several actuator combinations - Aluminum beam.

2.4.7. Effect of Beam Material Properties

In this section, the effect of beam material properties is summarized by looking at the response of several clamped beams of dimension $150 \times 29 \times 0.762$ mm with $112 \times 25 \times 0.51$ mm double-sided actuators bonded at the beam center (actuator size is 75 % of the total length of the beam). Two actuator thicknesses are investigated: 0.14 mm and 0.762 mm. Material properties are given in Table 2.14.

	Density (kg/m ³)	Flexural Modulus (N/m ²)
Aluminum	2,700	$71,000 \times 10^6$
Carbon	1630	$98,000 \times 10^6$
Titanium	4600	$11,500 \times 10^6$
Steel	7,700	$195,000 \times 10^6$
Lexan	1,200	$2,300 \times 10^6$
PKI-500 Actuator	7,600	$71,000 \times 10^6$

Table 2.14 Material properties

Results shown in Figure 2.23 show how deflection and resonance frequency are affected by material properties and actuator thickness.

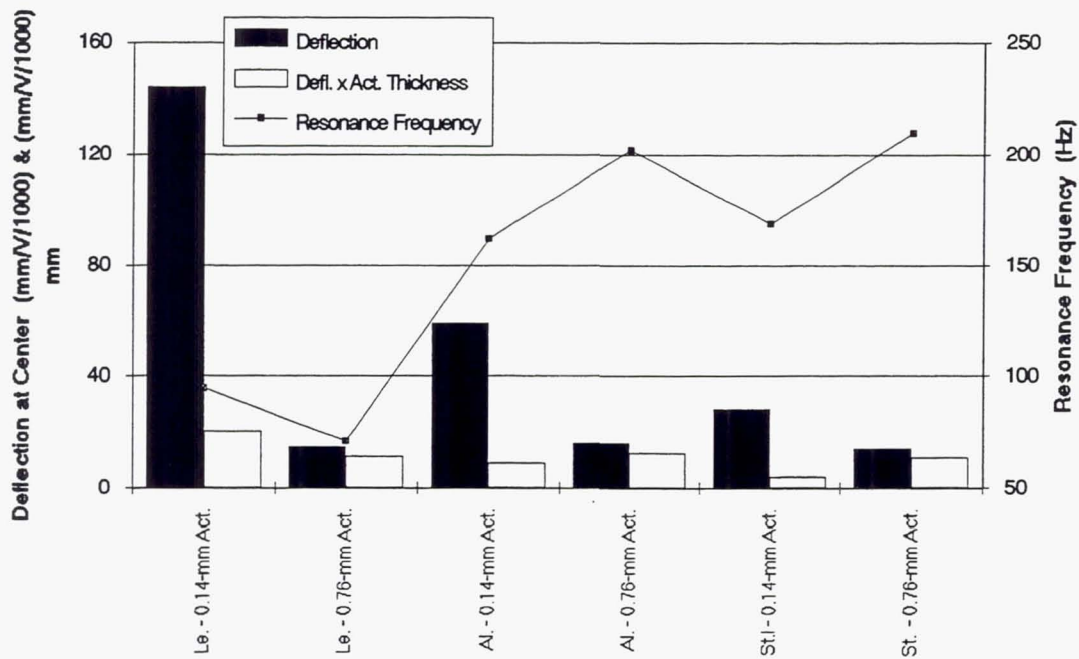


Figure 2.23 Deflection at beam center and resonance frequency for Lexan, aluminum, and steel beams.

Although the Lexan beam has the highest deflection, it also has the lowest resonance frequency. Compensating for frequency, Lexan would yield a lower deflection than the other materials due to its higher damping. As expected, the effect of actuator thickness is most important when actuator and beam mechanical properties are furthest apart such as with Lexan. When compensating for the fact that thicker actuators have a higher voltage limit and therefore can generate higher moments, the Lexan beam response actually drops for the thicker actuator as stiffness and inertial effects dominate. The "compensated response" increases for the aluminum and steel beams. Overall, aluminum and steel have responses and resonance frequencies that are fairly close, with aluminum having a slightly higher response. Compensating for the difference in resonance frequency would bring the responses even closer.

Finally, the responses of three clamped beams made of materials commonly used in aerospace applications: aluminum, titanium, and a third "ideal" material with the properties of pure carbon are presented (see Table 2.14). The dimensions of the beams are $150 \times 29 \times 0.762$ mm with $100 \times 25 \times 0.51$ mm double-sided actuators bonded at the center (actuator size is 67% of the total length of the beam).

The frequency and response for the three materials are plotted in Figure 2.23 and show that differences in deflection and resonance frequency between materials are small. However, these results must be taken with caution since the individual configurations were

not optimized and since the thickness of the beams are of the same order as the thickness of the actuators.

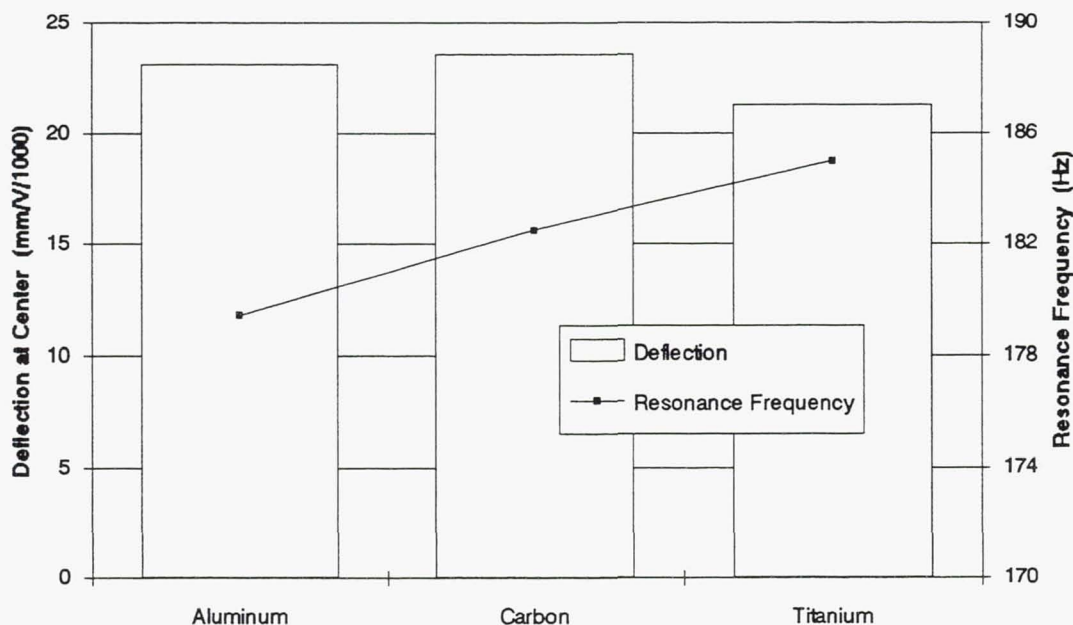


Figure 2.24 Deflection at beam center and resonance frequency for aluminum, carbon, and titanium beams.

2.5. Conclusions

The studies required for the proper design and testing of PZT actuator-based acoustic plate radiator design were performed in this Chapter. Analytical and FEM models of the actuated beam were developed and validated experimentally. An extensive optimization of the actuator and beam mechanical properties and geometry was performed to maximize the volume velocity of the first beam mode. Optimum configurations were identified and shown to vary depending on the resonance frequency requirement. These configurations were used as the starting point for the acoustic plate radiator design study presented in the next Chapter.

3. Acoustic Plate Radiator Design Using PZT Actuators

3.1. Introduction

The PZT actuator-based acoustic plate radiators investigated in this Chapter are designed to vibrate at the resonance frequency of their first mode where all points on the plate vibrate in phase ((1,1) mode).

Goals of Plate Radiator Study

The source configuration studied in this chapter is consistent with the piston-type sources used by Kraft and Kontos [7] in their analysis of active control systems for aircraft engines. Many results in this chapter are presented in terms of an "equivalent piston velocity" which relates the volume velocity of the plate radiators tested to the volume velocity of a plane piston source such as used by Kraft's analysis. This analogy, which is appropriate for this study, allows plate experimental results to be compared against the requirements set by Kraft's analysis.

As a result of Kraft's analysis, the target and goals of this study were made clear and quantifiable: Maximize equivalent piston velocity for a given frequency. This translates into a plate radiator which vibrates such that all points on the plate are in phase, thus at a frequency below the resonance frequency of the (1,2) or (2,1) plate modes. In addition, maximizing plate velocity means that the plate radiator frequency should probably be at or close to the resonance frequency of the first plate mode ((1,1) mode).

Design Approach

Much can be learned about acoustic plate radiator design from the beam optimization study presented in the previous Chapter. Rather than starting from the very beginning, the plate analysis and optimization presented in this section are a direct extension of the beam findings. However, since plate and beam results can differ significantly, optimization studies were performed when warranted to identify the optimum plate configuration for this application.

The plate design process proceeded as follows: From the beam results, it was determined that a double-sided actuator configuration bonded at the center of the beam was a good compromise in terms of maximizing beam response at a fixed natural frequency, and in terms of ease of fabrication. Optimum actuator thicknesses and lengths were identified and a number of materials were tested. Since aluminum offers a good compromise in terms of performance, cost, and ease of fabrication, a double-sided actuator configuration bonded at the center of an aluminum plate was chosen as the starting point for this study. Actuator size and thickness were then optimized to maximize plate volume velocity at a given resonance frequency for the first plate mode. plates were then fabricated and tested.

Content of Chapter

This Chapter begins with a short review of the theory of acoustic radiation by flexural modes in plates. Next, a brief survey of past work on plate actuation using PZT actuators is presented. The moments induced by the actuators on to the plates are discussed and a generalized FEM approach is presented as well as the various assumptions of the model. The analysis is carried out using the FEM software ANSYS [30]. Numerical results are then validated against experimental results. Next, PZT actuator/plate optimization studies are performed starting out from the insight gained from the actuator/beam configuration results. Computations for the maximum dynamic stress developed in the actuator are also presented for the optimized actuator/plate configuration so as to ensure structural integrity of the assembly. Fatigue life estimates are also presented for the plate. Finally, experimental results are presented which were obtained using 15 optimized and non-optimized plates.

3.2. Acoustic Radiation by Flexural Modes in a Finite Plate

As discussed earlier, the reasons for operating the plate radiator around its (1,1) mode are clear from Kraft's analysis of the cancellation of acoustic modes in fan ducts. This section briefly recalls some results from free-field plate acoustic radiation theory which shed additional light on the behavior of acoustic plate radiators for aircraft engines.

The dependence of the far-field acoustic pressure and intensity on plate size and modal parameters is investigated using Rayleigh's integral. Conditions for optimum radiation are then described and shown to correspond to a plate radiating in its (1,1) mode.

A similar conclusion can be reached in the wavenumber domain where it is easy to show that at low frequency the radiation efficiency is highest for the first mode as the structural wavenumber spectrum of the (1,1) mode is maximum at zero (corresponding to zero frequency) [31].

Normal Velocity at the Plate

For simplicity, the case of a simply-supported plate in an infinite baffle is considered since it has a simple solution for its mode shapes. The normal velocity for a plate of length a and width b is given by Blevins [32]:

$$v_n(x, y) = v_{pq} \sin\left(\frac{p\pi x}{a}\right) \sin\left(\frac{q\pi y}{b}\right) \quad (3.1)$$

where, $0 \leq x \leq a$, $0 \leq y \leq b$, and p and q are the modal numbers in the x and y directions respectively.

Acoustic Pressure Away From a Plate Vibrating in a (p, q) Mode

The sound pressure away from a plate vibrating in a (p, q) mode can be obtained using Rayleigh's integral [33]:

$$p(r, t) = \frac{j\omega\rho_0}{2\pi} e^{j\omega t} \int_S \frac{v_n(r_s) e^{-jkR}}{R} dS \quad (3.2)$$

where, r is the position vector for the observation point, r_s is the position vector for the plate surface dS , $v_n(r_s)$ is the normal velocity of dS , and $R = |r - r_s|$ is the distance between the observer point and the surface dS .

The acoustic pressure in the far-field can be obtained by replacing $v_n(r_s)$ in Equation 3.2 by its expression in Equation 3.1 [34]:

$$p(r, \theta, \phi) = j v_{pq} k \rho_0 c \frac{e^{-jkR}}{2\pi r} \frac{ab}{pq \pi^2} \left[\frac{(-1)^p e^{-j\alpha} - 1}{(\alpha/p\pi)^2 - 1} \right] \left[\frac{(-1)^q e^{-j\beta} - 1}{(\beta/q\pi)^2 - 1} \right] \quad (3.3)$$

where the time dependence of the acoustic pressure has been omitted for simplicity. r is the distance between the observation point and the origin of the coordinate system as shown in Figure 3.1. α and β are given by:

$$\alpha = ka \sin \theta \cos \phi, \quad \beta = kb \sin \theta \sin \phi \quad (3.4)$$

where θ and ϕ are defined in Figure 3.1.

Acoustic Intensity Away From the Plate

The far field acoustic intensity can then be obtained from Equation 3.3 as [34]:

$$\frac{|p(r, \theta, \phi)|^2}{2\rho_0 c} = 2\rho_0 c |v_{pq}|^2 \left(\frac{kab}{r pq \pi^3} \right)^2 \left\{ \frac{\cos\left(\frac{\alpha}{2}\right) \cos\left(\frac{\beta}{2}\right)}{\left[(\alpha/p\pi)^2 - 1\right] \left[(\beta/q\pi)^2 - 1\right]} \right\}^2 \quad (3.5)$$

where $\cos(\alpha/2)$ is used when p is odd, $\sin(\alpha/2)$ is used when p is even, $\cos(\beta/2)$ is used when q is odd, and $\sin(\beta/2)$ is used when q is even.

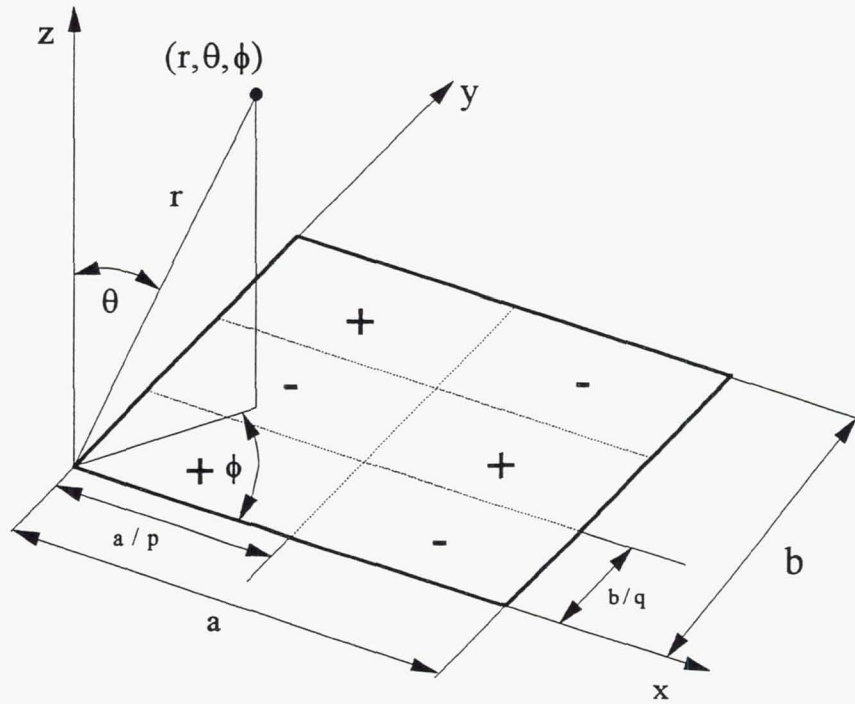


Figure 3.1 Coordinate system for plate radiation [31].

High Frequency Solution

The maximum intensity occurs for $\alpha = p\pi$ and $\beta = q\pi$ (i.e. at a specific angle), and if the frequency is high enough so that the acoustic wavelength is smaller than the structural wavelength [31]:

$$\frac{|p(r, \theta, \phi)|_{\max}^2}{2\rho_0 c} = \rho_0 c \frac{|v_{pq}|^2}{2} \left(\frac{kS}{8\pi r} \right)^2 \quad (3.6)$$

This result implies that at high frequency, the acoustic power radiated is independent of the plate modal numbers.

Low Frequency Solution

The low frequency situation occurs when the acoustic wavelength is larger than the structural wavelength (or larger than the plate) which is more typical of the aircraft engine situation. The plate radiates like a point volume source with a volume velocity Q equal to $\int_S v_n(x, y) dS$. Assuming that $(\alpha/p\pi)^2 \ll 1$ and $(\beta/q\pi)^2 \ll 1$, the acoustic intensity is obtained from Equation 3.5 as:

$$\frac{|p(r, \theta, \phi)|_{LM}^2}{2\rho_0 c} = 2\rho_0 c |v_{pq}|^2 \left(\frac{kS}{r p q \pi^3} \right)^2 \quad (3.7)$$

As expected, at low frequency the plate radiation is omnidirectional and inversely proportional to the product of the plate modal numbers because of cancellation between modal cells. This fundamental result implies that the lowest order mode is the most efficient radiator at low frequency.

Acoustic intensity levels obtained from Equations 3.6 and 3.7 are shown Table 3.1 for the first few plate modes showing again that a small plate vibrating in its (1,1) mode is the most efficient acoustic radiator.

Mode Number	Acoustic Intensity Level Low Frequency (dB)	Acoustic Intensity Level High Frequency (dB)
(1,1)	0.0	-4.2
(1,2) ; (2,1)	-6.0	-4.2
(2,2)	-12.0	-4.2
(1,3) ; (3,1)	-9.5	-4.2

Table 3.1. Far-field acoustic intensity level as a function of plate mode number (with (1,1) mode as reference) - Low frequency and high frequency approximations.

3.3. Plate Actuation Using Piezoelectric Actuators - Literature Survey

The behavior of two-dimensional patches of piezoelectric material bonded to the surface of elastic plates for use as vibration actuators was first studied by Dimitriadis et. al. [16]. A static analysis was employed to estimate the loads induced by the PZT actuator to the supporting elastic structure. The theory was then applied to develop an approximate dynamic model for the vibration response of a simply-supported elastic rectangular plate excited by a PZT patch of variable rectangular geometry. It was demonstrated that it is possible to tailor the shape of the actuator to either excite or suppress particular modes.

Kim and Jones [17] extended the previous work of Dimitriadis et. al. [16] to include the bonding layer in the effective moment imparted by the PZT actuators. It was shown that the effective bending moments induced by the piezoceramic actuators increase with a decreasing bonding layer thickness. Moreover, it was shown that the influence of Young's Modulus, Poisson's ratio and the damping of the bonding layer are not important factors in optimizing the PZT actuator/plate coupling.

3.4. FEM Approach - Effective Moment Computation

The current analysis uses a numerical FEM-based approach in modeling the plate as opposed to the approaches described previously [16,17] where closed form expressions

were derived for simply-supported plates. The advantage of the FEM approach is the generality found in modeling plates of various configurations and support conditions.

Element "type 63" was used in ANSYS. This element has both bending and membrane capabilities and has 4 nodes per element. There are 6 degrees of freedom at each node: translations in the x , y , and z directions, and rotations about nodal x , y , and z axes. The plate radiator configuration modeled is shown in Figure 3.2.

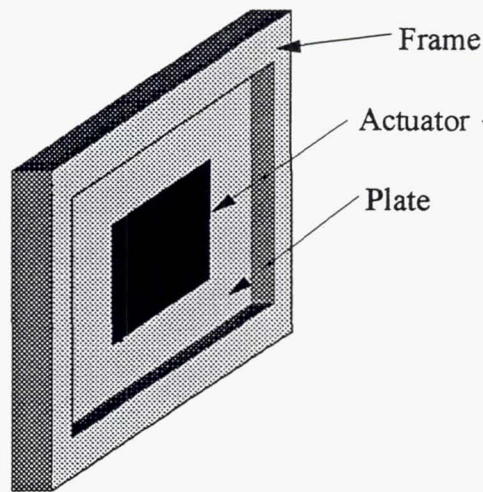


Figure 3.2 Plate radiator in frame with PZT actuator bonded at center.

Modeling boundary conditions is crucial when comparing frequency and forced response results with experiments. The boundary conditions are modeled through linear and torsional springs as shown in Figure 3.3.

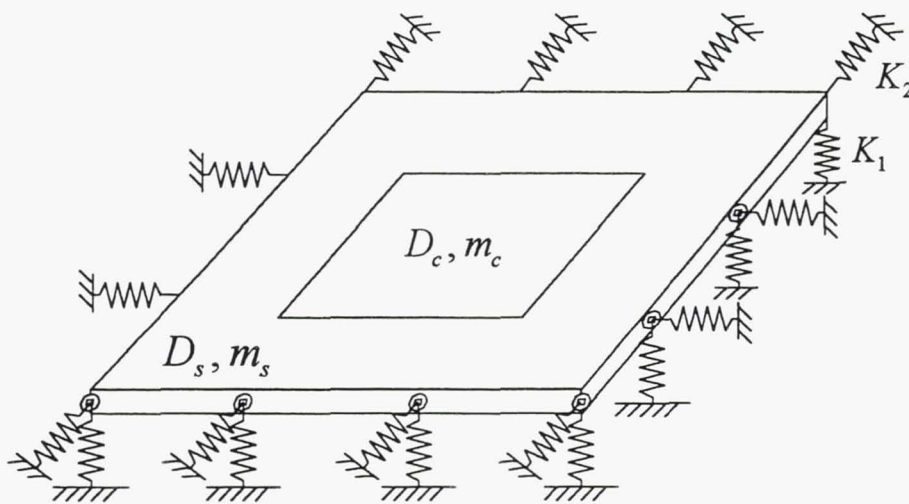


Figure 3.3 Plate radiator with linear and torsional spring boundary conditions.

Where K_1 and K_2 are the linear and torsional springs stiffnesses respectively. D_s and m_s are the flexural stiffness and density per unit area of the structure, and D_c and m_c are the effective stiffness and density of the PZT-structure composite area.

The effective moments induced by the actuator are shown in Figure 3.4.

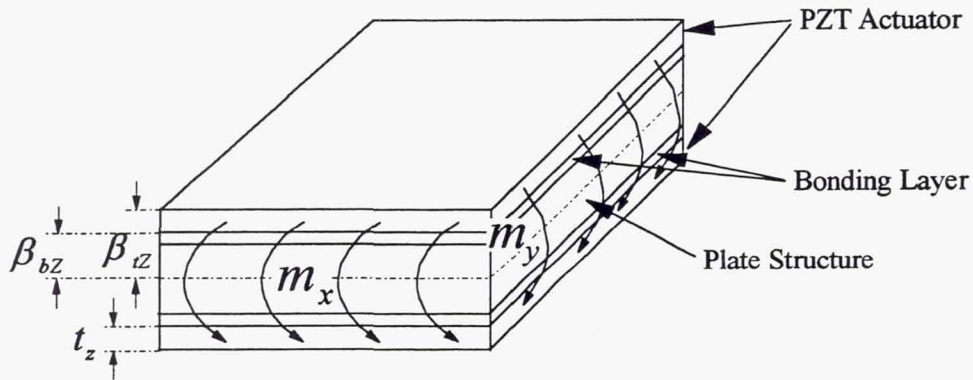


Figure 3.4 Effective moments induced in the plate by the PZT actuators.

The (edge moments/unit length) induced in the structure are denoted by m_x and m_y . An extension of the moment transfer model developed for the beam in Chapter 2 is used in this analysis. Following the same convention as used for the beam (see Equation 2.3), β_{tz} is the distance from the upper surface of the actuator to the plate neutral axis, β_{bz} is the distance from the lower surface of the actuator to the plate neutral axis, and t_z is the actuator thickness. The biaxial unrestrained state of strain in the actuators is depicted in Figure 3.5.

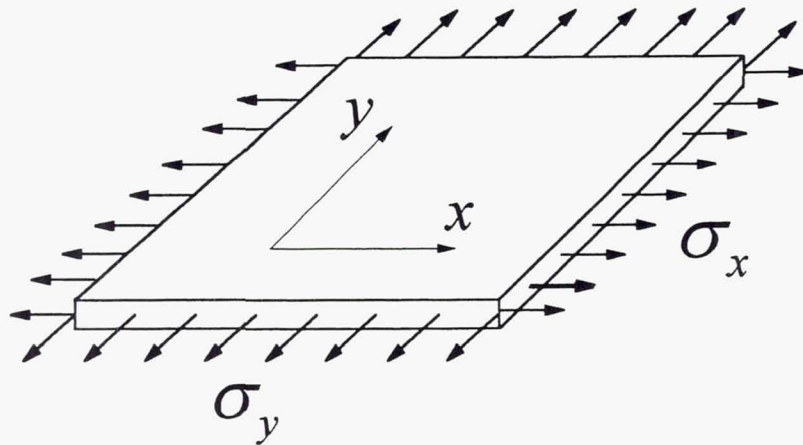


Figure 3.5 Stresses in the actuators.

Hook's Law is applied to compute the stress field (σ_x and σ_y) assuming a plane stress condition.

$$\begin{aligned}
\sigma_x &= \sigma_y \\
&= \frac{E_z}{(1-\nu_z^2)} (\varepsilon_x + \nu_z \varepsilon_y) \\
&= \frac{E_z}{(1-\nu_z)} \frac{d_{31} V}{t_z}
\end{aligned} \tag{3.8}$$

where ε_x and ε_y are the strain components in the x and y directions, E_z is the actuator Young's Modulus, ν_z is the actuator Poisson's ratio, d_{31} is the piezoelectric coupling coefficient, and V is the voltage applied across the actuator. The induced moment per unit length of actuator edge is then given by:

$$\begin{aligned}
m_x &= m_y \\
&= 2 \sigma (\beta_{xz} - \beta_{bz}) \frac{(\beta_{xz} + \beta_{bz})}{2} \\
&= \frac{(\beta_{xz}^2 - \beta_{bz}^2)}{(1-\nu_z)} \frac{E_z d_{31} V_0}{t_z}
\end{aligned} \tag{3.9}$$

The moment relationship given above is used for the forced response analysis of plate radiators. The expressions D_c and m_c are computed by taking the effective averaged properties. Assuming an arbitrary thickness t_{eff} (in the neighborhood of the plate thickness) for the composite plate, the effective Young's Modulus for the composite plate is given by:

$$E_{eff} = \frac{1}{t_{eff}^3} [E_s t_s^3 + E_b ((2\beta_{bz})^3 - t_s^3) + E_z ((2\beta_{xz})^3 - (2\beta_{bz})^3)] \tag{3.10}$$

Where t_s is the beam thickness. The effective density of the composite section is given by:

$$\rho_{eff} = \frac{1}{t_{eff}} [\rho_s t_s + \rho_b (2\beta_{bz} - t_s) + 2\rho_z (\beta_{xz} - \beta_{bz})] \tag{3.11}$$

Where ρ_s , ρ_b , and ρ_z are the densities of the beam, bonding layer and actuator respectively.

3.5. Comparison Between Analysis and Experiment - Methodology

As opposed to beams, "good" clamped or simply-supported boundary conditions are practically impossible to attain with plates. In practice, plate radiators are neither clamped nor simply-supported, but somewhere in between. Since it is not possible to model the boundaries accurately, boundary conditions and damping used in the analytical model were

obtained from experimental results for the mode under study which is common practice in this kind of study.

The steps followed to obtain the forced plate response are as follows: (1) Adjust the linear and torsional spring constants K_1 and K_2 until the natural frequency obtained from the experimental results match that of the analytical results. (2) Using the spring constants determined in (1) and the measured damping ratio for the mode under study, calculate the forced response of the plate and compare to experimental results.

3.6. Experimental Validation

The validation of the analytical model was performed using one Lexan and two aluminum plates as shown in Figure 3.6.

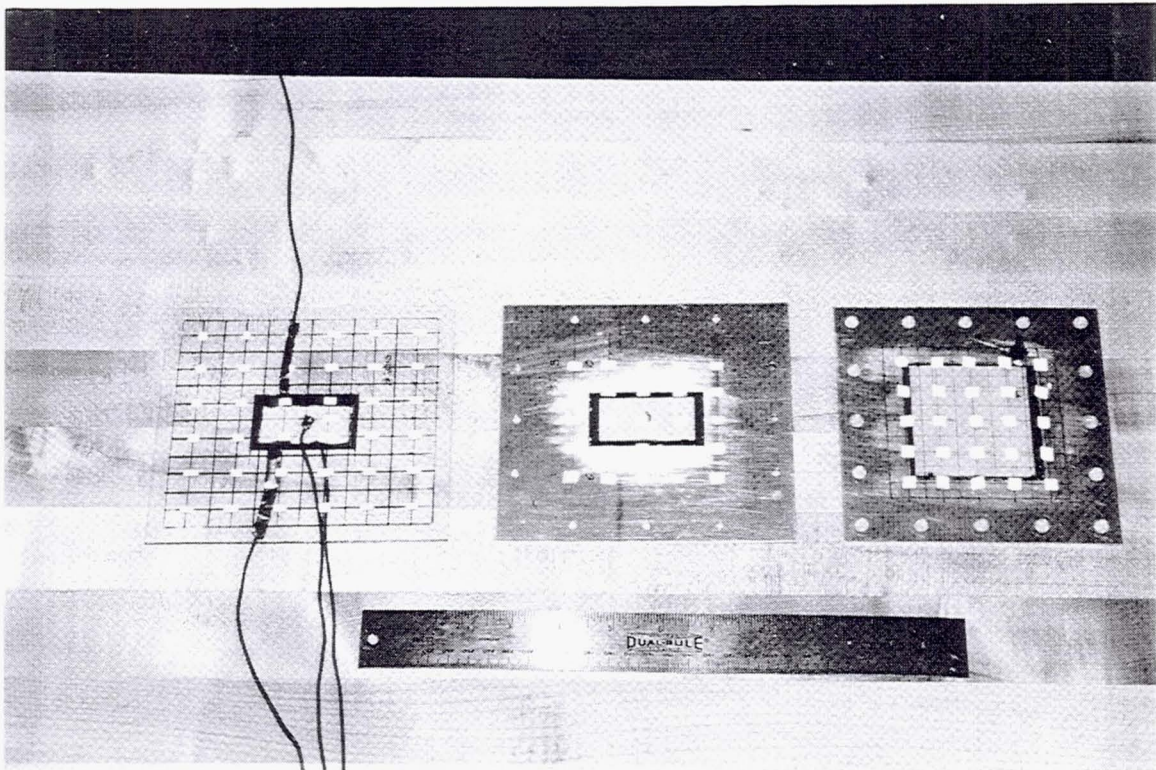


Figure 3.6. Plate samples used for experimental validation.

PKI-500 actuators from Piezo Kinetics with dimensions $49 \times 25 \times 0.28$ mm similar to the actuators used for the beam experiments were bonded to each plate using the GA-2 epoxy adhesive (see Appendices A and B). The actuator electrode bonded to the plate surface was connected to the power supply using a 0.076-mm copper electrode bonded to the actuator with conductive silver epoxy.

3.6.1. Plate Experimental Setup

The experimental setup shown in Figures 3.7 and 3.8 is similar to the beam setup. The plates are mounted in an aluminum frame which approximates a clamped boundary condition.

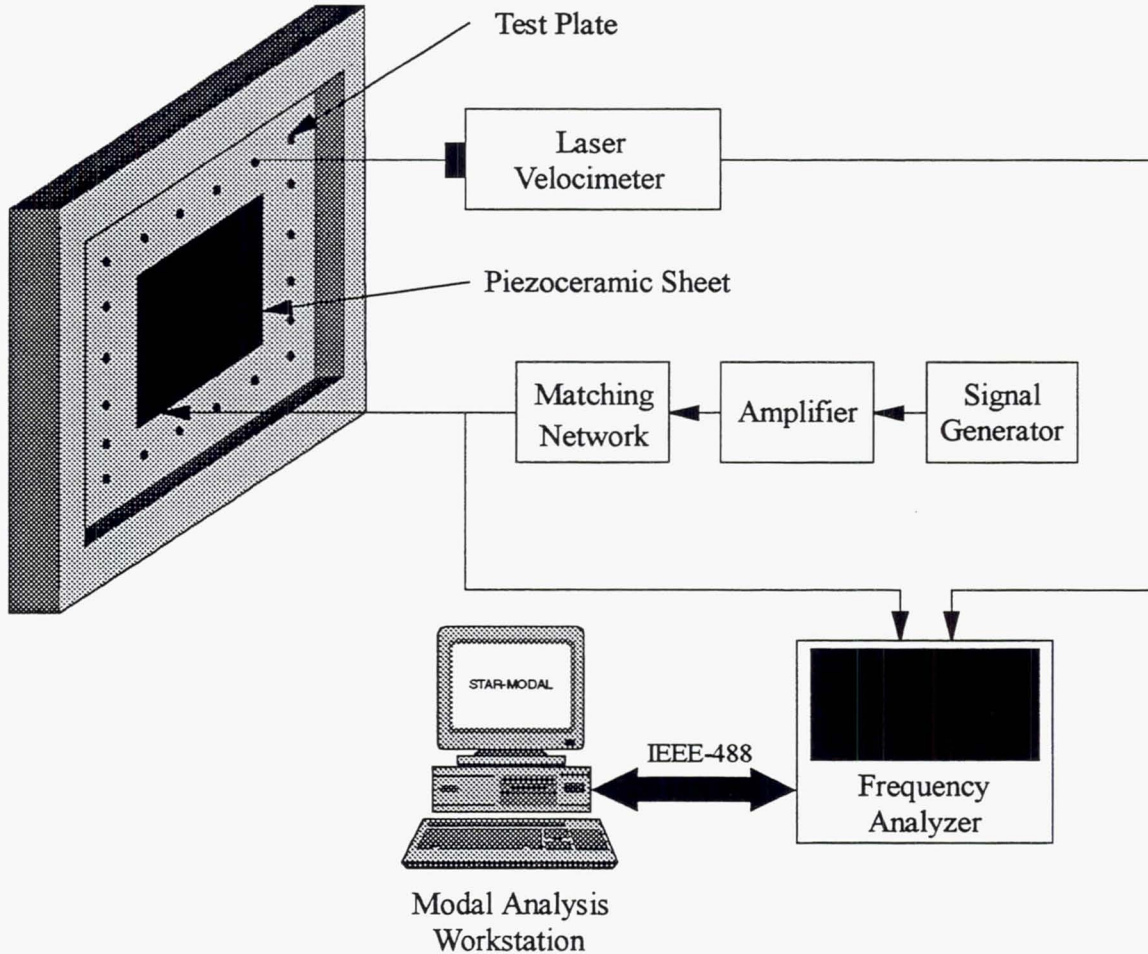


Figure 3.7. Plate experimental setup.

PZT actuators were bonded on either or both sides of the plates using GA-2 epoxy from Measurement Group, Inc. The actuators used were either a $49 \times 25 \times 0.28$ mm PKI-500 PZT actuators from Piezo Kinetics for the first two plates; or a 66×66 mm D3203HD actuators from Motorola for the third plate. The PKI-500 material is the same "middle of the range" material as used for the beam experiments with a $d_{13}Y_{11}$ product equal to 12.4 N/V-m. The D3203HD material had the second highest $d_{13}Y_{11}$ product of the 36 materials surveyed: 17.8 N/V-m with a fairly good Curie temperature of 260 degrees C and a high coercive field of 27 V/mil (see Appendix C). It was recommended for this application by Dr. Venkataramani from the Electrical Ceramics Program at GE CRD.

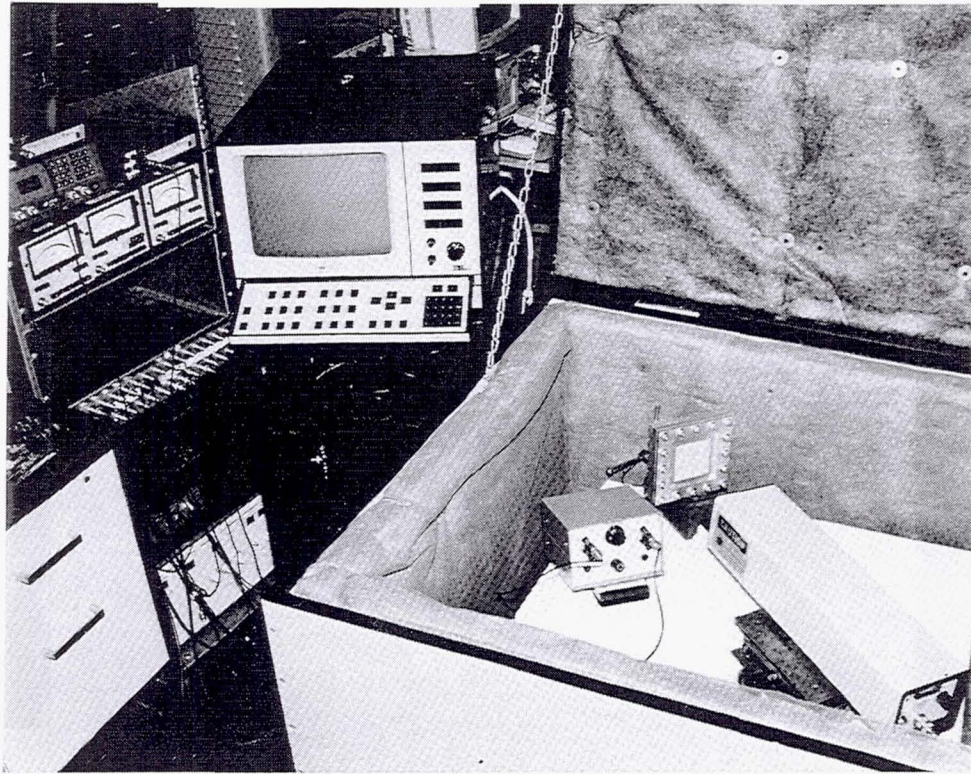


Figure 3.8. Plate experimental setup.

The actuators are powered using a signal generator, amplifier, and matching network combination. A laser velocimeter measures the plate velocity at several points on the plate. Both actuator voltage and plate velocity signals are sent to a B&K 2032 FFT analyzer connected to a modal analysis workstation running the STAR modal analysis software. All test data are stored on the computer for archiving and analysis.

3.6.2. Experimental Validation - $140 \times 127 \times 1.6$ mm Lexan Plate

A $140 \times 127 \times 1.6$ mm Lexan plate with a $49 \times 25 \times 0.28$ mm PKI-500 actuator bonded at its center using GA-2 epoxy was used for the first test. Thirty-six measurement points were used as shown in Figure 3.9.

As with the Lexan beam experiment, the actuator properties dominate at the center of the plate.

Modal frequencies, damping, and amplitudes were estimated using high resolution sine sweep excitation, wideband random excitation, narrowband random excitation using zoom analysis, and impulse hammer excitation. The STAR MODAL modal analysis software

was used to estimate modal parameters when using wideband random excitation. A 3-dB or 10-dB bandwidth method was used to estimate damping for the other methods.

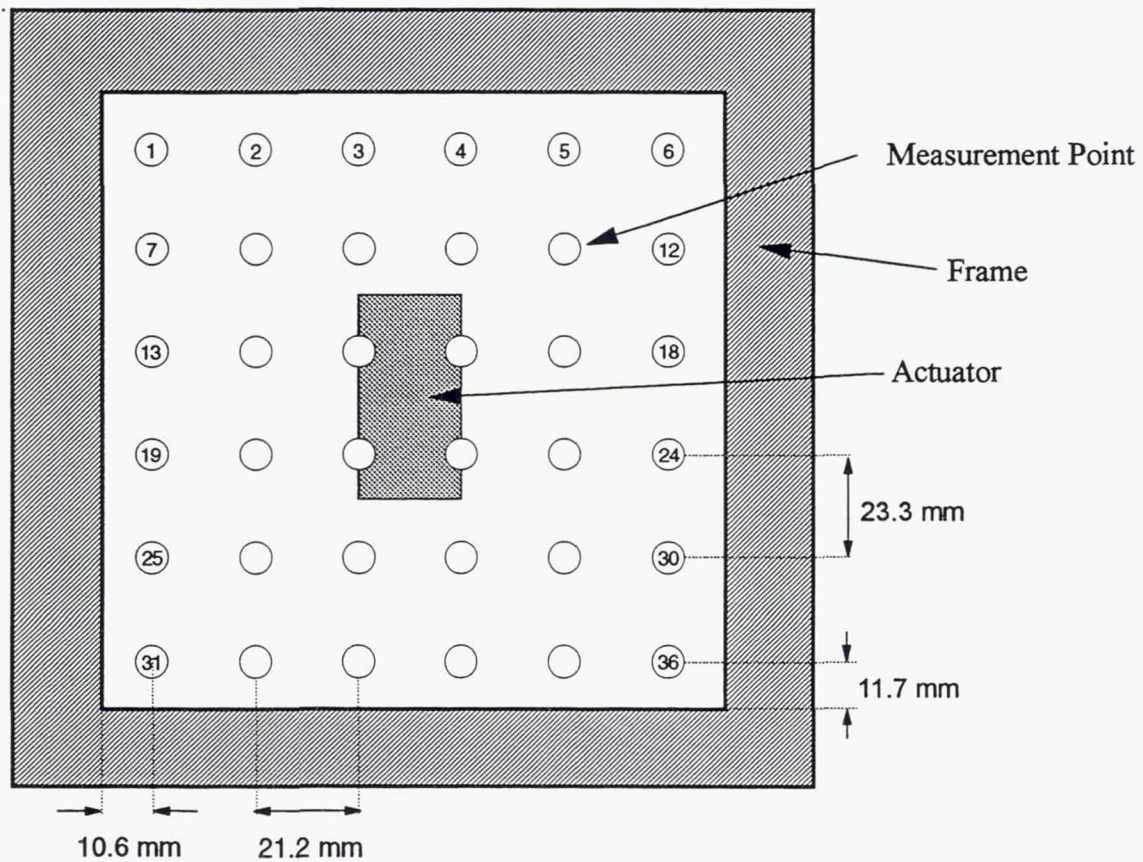


Figure 3.9. Plate setup - Lexan

Natural Frequencies

The experimental and analytical natural frequencies are given in Table 3.2:

Mode	Experiment		Analysis - With Actuator				Analysis - Without Actuator	
	Test 1 (Hz)	Test 2 (Hz)	Simply Supported (Hz)	Test 1 Compliant Boundary (Hz)	Test 2 Compliant Boundary (Hz)	Clamped (Hz)	Simply Supported (Hz)	Clamped (Hz)
1,1	162	170	109	164	171	193	121	221
1,2	338	349	259	330	344	384	284	425
2,1	396	397	293	375	389	433	319	478

Table 3.2. Natural frequencies - Lexan plate

Test 1 and Test 2 were performed two months apart in similar conditions. The differences between tests can most probably be attributed to slight differences in clamping pressures and plate position in the frame.

The resonance frequencies "with actuator" were obtained using the Finite Element model. The resonance frequencies "without actuator" were calculated using the formulas for plate natural frequencies given in Chapter 4 [35]. Bonding the actuator to the plate increases the mass of the system and lowers the resonance frequencies of the plate.

The "compliant boundary" values were calculated by adjusting the linear and torsional spring constants of the boundaries until the resonance frequency of the (1,1) mode was within 1.5% of the experimental frequency as described in Section 3.5. The higher mode resonance frequencies were then calculated using the same spring constants. Although this technique usually gives accurate results, it is very time consuming since it requires several iterations to identify the proper boundary conditions.

Damping and Displacement

The damping and plate displacement response at the center measured using high resolution sine sweep excitation, wideband random excitation (0-400 Hz), and narrowband random excitation (50 Hz bandwidth) are all within 5% of each other with average values listed in Table 3.3.

Mode	Experiment - Peak Response at Center		Analysis - Peak Response at Center				Experiment - Damping	
	Test 1 (mm/V) / 1000	Test 2 (mm/V) / 1000	Simply Supported (mm/V) / 1000	Test 1 Compliant Boundaries (mm/V) / 1000	Test 2 Compliant Boundaries (mm/V) / 1000	Clamped (mm/V) / 1000	Test 1 (%)	Test 2 (%)
1,1	7.34	5.08	7.43	5.63	5.57	5.401	2.23	2.37

Table 3.3. Peak response at plate center and damping - Experimental and analytical data - Lexan plate.

Where the peak response at the plate center is expressed in millimeters per Volt input to the PZT actuator. The displacement magnitudes at the plate center were calculated using the averaged measured damping factor and the linear and torsional spring constants at the plate boundary listed in Table 3.4.

	Linear Stiffness (N/m)	Torsional Stiffness (N/rad)
Test 1	8.5×10^4	1.1
Test 2	8.0×10^5	1.7

Table 3.4. Linear and torsional spring constants at plate boundary.

The plate center displacement measured in Test 1 is substantially higher than the plate displacement measured in Test 2. Again, this is most probably due to a difference in clamping pressure and plate position in the frame.

Measured and analytical responses are 9 % and 30 % apart from each other.

Mode Shapes

Mode shapes were obtained using the STAR MODAL modal analysis software. As a result of the actuator having a much higher density and Young's Modulus than the Lexan plate, the mode shapes of the system are substantially different from those of a simple plate with several additional modes occurring, and only the first four plate modes being clearly identifiable as shown in Figure 3.10.

Equivalent Piston Velocity

In order to simplify comparison between tests, results are presented in terms of a single number: the equivalent piston velocity response which characterizes the acoustic source strength for this particular application.

The equivalent piston velocity V_p is given by:

$$V_p = \frac{Q_p}{A} \quad (3.12)$$

where A is the plate area and Q_p is the volume velocity response. Q_p is equal to the vectorial sum of the complex velocity responses $v_k e^{j\theta_k}$ measured at k discrete points over the plate:

$$Q_p = \frac{A}{k} \left| \sum_{i=1}^k v_k e^{j\theta_k} \right| \quad (3.13)$$

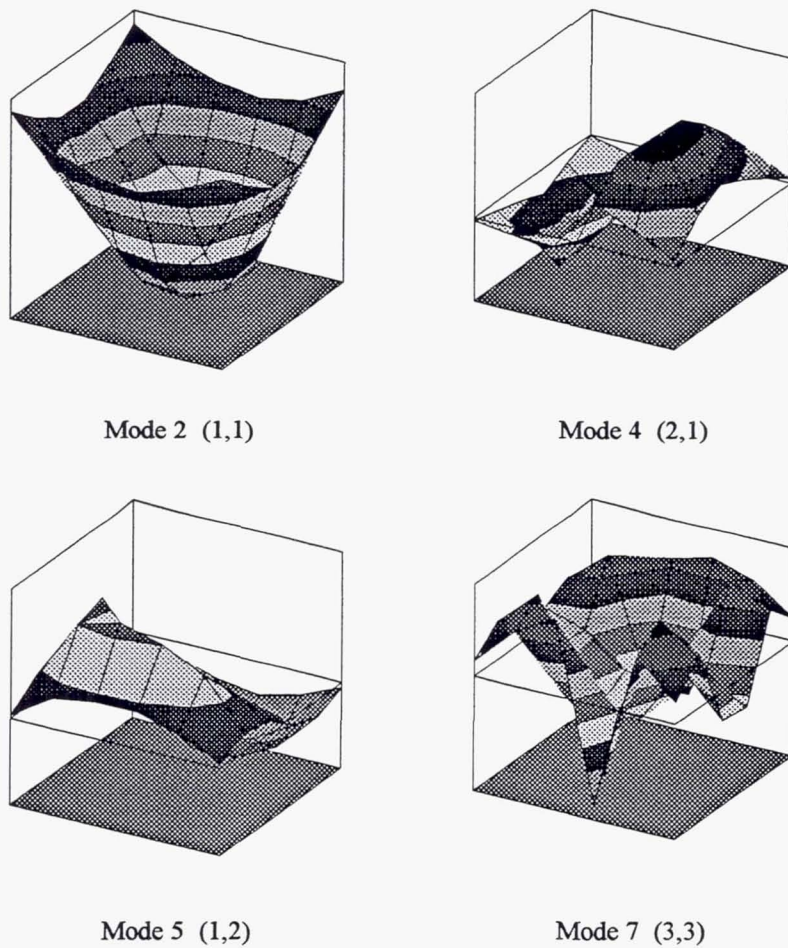


Figure 3.10. Experimental mode shapes - Lexan plate.

Figure 3.11 shows the equivalent piston velocity response for the Lexan plate.

Mode 1 is the first bending mode of the frame/plate assembly. As shown in figure 3.10, modes 2, 4, 5, and 7 correspond to the plate (1,1), (2,1), (1,2), and (3,3) modes with the other modes not clearly corresponding to conventional plate modes due to the actuator mass and stiffness effects.

Modes 2 and 7 have a large equivalent piston velocity V_p and therefore radiate noise efficiently. Modes 4 and 5 are "self-canceling" due to their dipole-type radiation which results in poor radiation efficiency.

Although mode 7 has the largest equivalent piston velocity response, it occurs at the expense of large velocities at some plate locations which can result in large stress levels in the plate and the actuator. In order to take this factor into account, Figure 3.12 shows the ratio of the equivalent piston velocity by the maximum velocity measured on the plate for

each mode. Discarding the first mode (frame bending mode), it is clear that (1,1) mode is best at generating a high equivalent piston velocity with minimum plate motion.

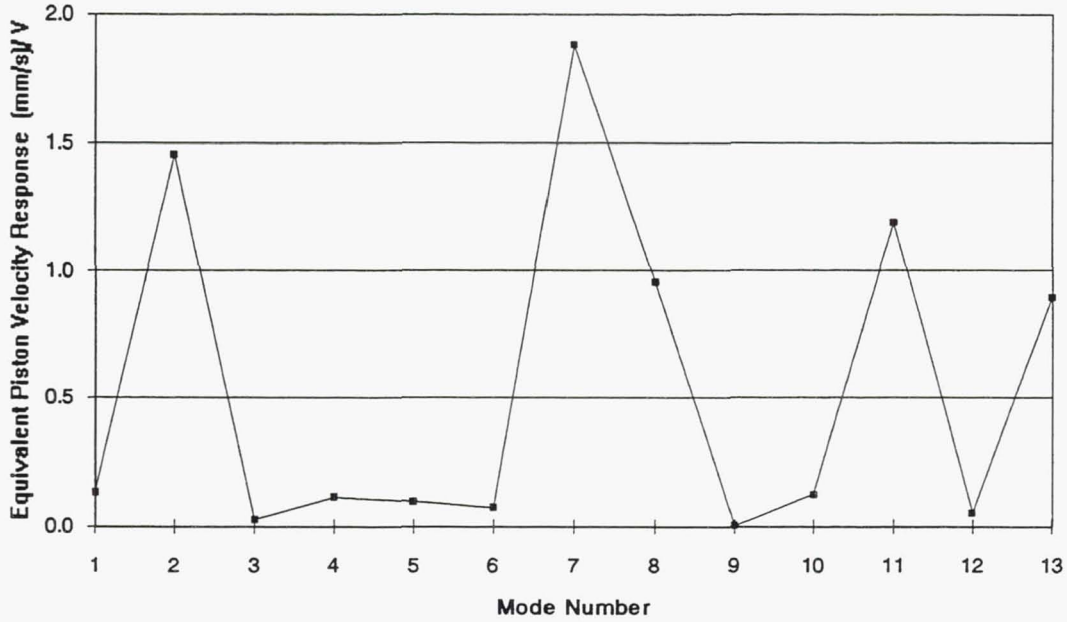


Figure 3.11. Equivalent piston velocity response - Lexan plate.

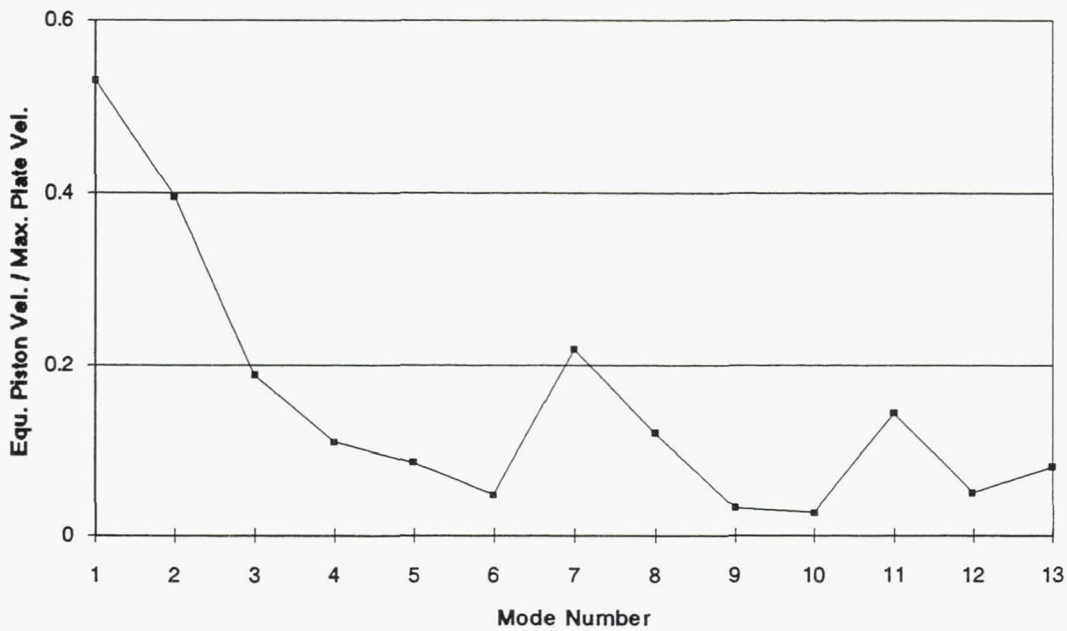


Figure 3.12. Ratio of equivalent piston velocity response by maximum plate velocity - Lexan plate.

3.6.3. Experimental Validation - 100 × 115 × 0.76 mm Aluminum Plate

Next, a 100 × 115 × 0.76 mm aluminum plate was tested with 49 × 25 × 0.28 mm PKI-500 PZT actuators bonded at the center of each side of the plate using GA-2 Epoxy. The actuators were powered out-of-phase with each other. Twenty five measurements points were located at regular intervals on the plate for modal analysis.

Natural Frequencies

The experimental and analytical (FEM) natural frequencies are given in Table 3.5:

Mode	Experiment		Analysis - With Actuator	Analysis - Without Actuator	
	Resonance Frequency (Hz)	Damping (%)	Compliant Boundary (Hz)	Simply Supported (Hz)	Clamped (Hz)
1,1	500	1.44	503	326	600
2,1	1023	0.78		748	1119
1,2	1230	0.68		883	1324
2,2	1903	0.64		1305	1803

Table 3.5. Natural frequencies - 100 × 115 × 0.76 mm aluminum plate.

Damping and Displacement

The plate displacement response at the center was measured using a low-level, 2.4 Volt pure-tone signal powering the actuator.

Mode	Peak Response At Center	
	Experiment (mm/V) / 1000	Analysis (mm/V) / 1000
1,1	8.91	8.97

Table 3.6. Peak response at plate center - Experimental and analytical data - 100 × 115 × 0.76 mm aluminum plate.

Measured and analytical responses are within 1% of each other. It should be noted that the extreme goodness of the match has more to do with coincidence than great model

accuracy. Although the model is thought to be fairly accurate, it does not have the capability to predict plate response with such precision.

Mode Shapes

In the case of the aluminum plate, the added stiffness and mass due to the PZT actuators do not greatly affect the properties of the bare plate. The first four modes of vibration of the composite plate are similar to the first four modes of a bare plate and are shown in Figure 3.13.

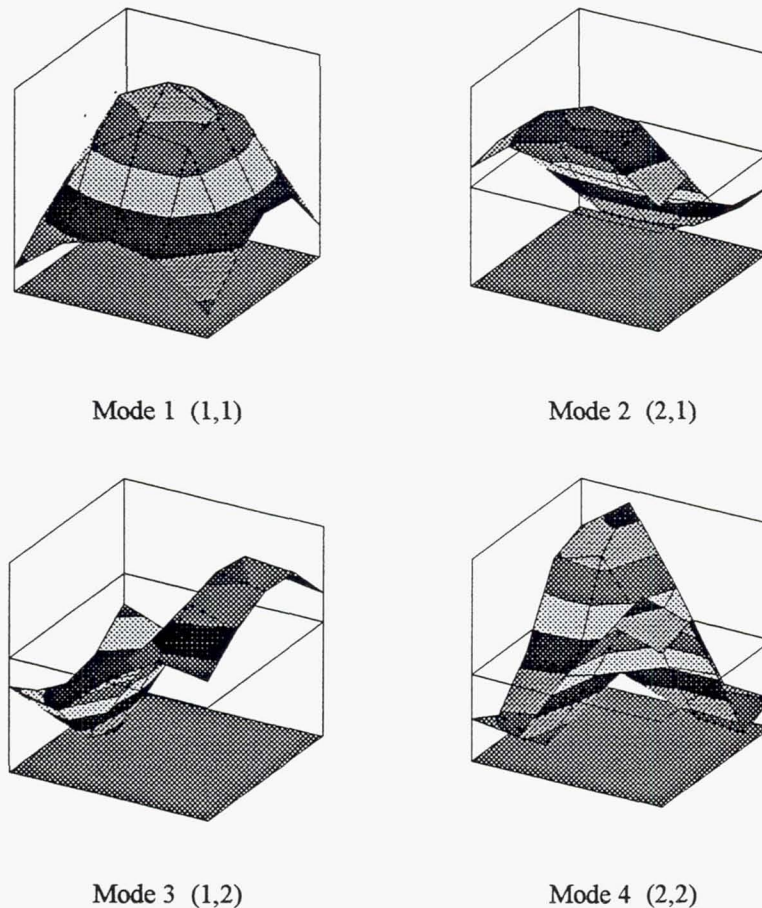


Figure 3.13. Experimental mode shapes - $100 \times 115 \times 0.76$ mm aluminum plate.

Equivalent Piston Velocity

Figure 3.14 shows the equivalent piston velocity response for the $100 \times 115 \times 0.76$ mm aluminum plate.

As expected, the (1,1) and (3,1) modes have large equivalent piston velocity responses and the overall modal response is very close to the response expected from a bare plate.

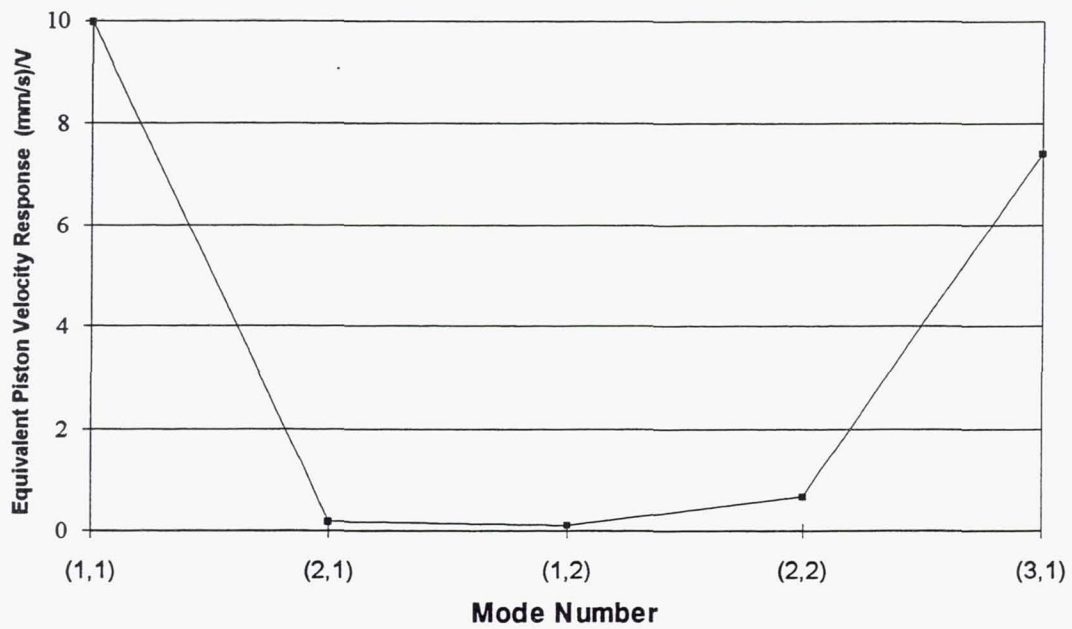


Figure 3.14. Equivalent piston velocity response - $100 \times 115 \times 0.76$ mm aluminum plate.

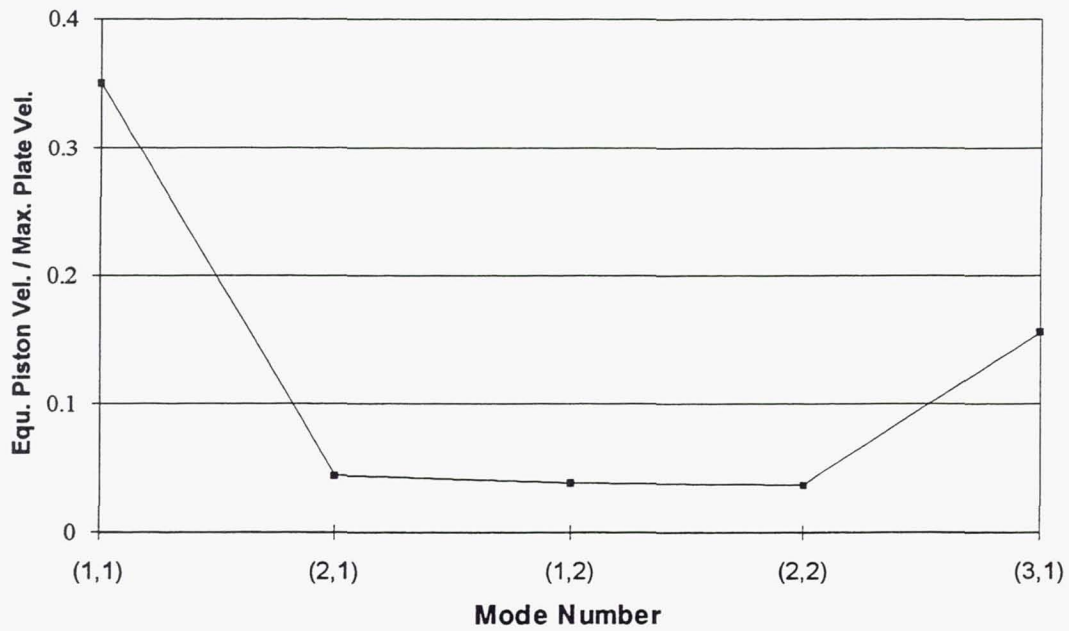


Figure 3.15. Ratio of equivalent piston velocity response by maximum plate velocity - $100 \times 115 \times 0.76$ mm aluminum plate.

3.6.4. Experimental Validation - 90 × 90 × 1.524 mm Aluminum Plate

A 90 × 90 × 1.524 mm aluminum plate was tested next. As discussed later in Section 3.7, these dimensions represent a good compromise between plate size, available thicknesses, resonance frequency, and performance. 66 × 66 × 0.51mm Motorola D3203HD PZT actuators were bonded on each side of the plate using GA-2 epoxy. Connection between the power supply and the actuator electrode bonded to the plate was through a 0.025-mm copper electrode soldered to the actuator surface.

The actuators were powered out-of-phase with one another. Twenty five measurement points were located at regular intervals on the plate for modal analysis.

Natural Frequencies

The experimental and analytical (FEM) natural frequencies are given in the table below:

Mode	Experiment		Analysis - With Actuator	Analysis - Without Actuator	
	Resonance Frequency (Hz)	Damping (%)	Compliant Boundaries (Hz)	Simply Supported (Hz)	Clamped (Hz)
1,1	1333	0.94	1335	917	1679
2,1	2755	0.78		2293	3427
1,2	2841	0.79		2293	3427

Table 3.7. Natural frequencies - 90 × 90 × 1.52 mm aluminum plate.

Damping and Displacement

The plate displacement response at the center was measured using a low-voltage pure-tone signal powering the actuator.

Mode	Peak Response At Center	
	Experiment (mm/V) / 1000	Analysis (mm/V) / 1000
1,1	7.05	7.29

Table 3.8. Peak response at plate center - Experimental and analytical data - 90 × 90 × 1.52 mm aluminum plate.

Again, measured and analytical responses are very close to each other.

Mode Shapes and Equivalent Piston Velocity

Although they are not presented in this report, mode shapes were measured and are essentially the same as those obtained for the $100 \times 115 \times 0.76$ mm aluminum plate. The added stiffness and mass due to the PZT actuators do not greatly affect the properties of the bare plate.

The equivalent piston velocity response and the ratio of equivalent piston velocity to velocity at the plate center for the (1,1) mode were determined from mode shape and plate center velocity measurements and are shown in Table 3.9.

Equivalent Piston Velocity Response (mm/s)/V	21.04
$\frac{\text{Equivalent Piston Velocity}}{\text{Velocity at Plate Center}}$	0.36

Table 3.9. Velocity data for (1,1) mode - $90 \times 90 \times 1.52$ mm aluminum plate.

3.6.5. Summary - Experimental Validation

The analytical model was validated using experimental results obtained with Lexan and aluminum plates. The analysis is shown to predict plate response very accurately within the low actuator voltage levels investigated. Since the accuracy of the analysis also depends on how well the plate boundary condition and damping ratio are modeled, an iterative procedure is used to obtain the proper boundary condition.

The differences between analytical and experimental responses are 9 % and 30 % for the Lexan plate, and 1 % and 3 % for the aluminum plates.

3.7. Optimization of Actuator/Plate Configuration for Maximum Volume Velocity

As mentioned at the beginning of this Chapter, the plate analysis and optimization presented in this section are direct extensions of the beam study where optimum actuator thicknesses and lengths were identified and a number of materials were tested.

Due to the length of each analysis, only a limited number of configurations could be investigated numerically and it was decided to concentrate the optimization study on a double-sided actuator configuration bonded at the center of an aluminum plate. From the beam analysis, this configuration represents a good compromise in terms of maximizing

beam response at a fixed natural frequency, and in terms of ease of fabrication. Actuator size and thickness was optimized to maximize plate volume velocity at a given resonance frequency for the first plate mode. The properties of the PKI-500 material were used for this study as well as a plate damping ratio of 1.5%.

3.7.1. Effect of Actuator Size

The effect of actuator size was investigated using a $114 \times 114 \times 0.76$ mm clamped aluminum plate with 0.28-mm actuators bonded on each side of the plate at the center using epoxy glue (bond thickness: 0.13 mm).

Resonance frequency and deflection at the plate center (proportional to volume velocity) are shown in Figure 3.16 as a function of actuator size ratio (ratio of actuator area to plate area).

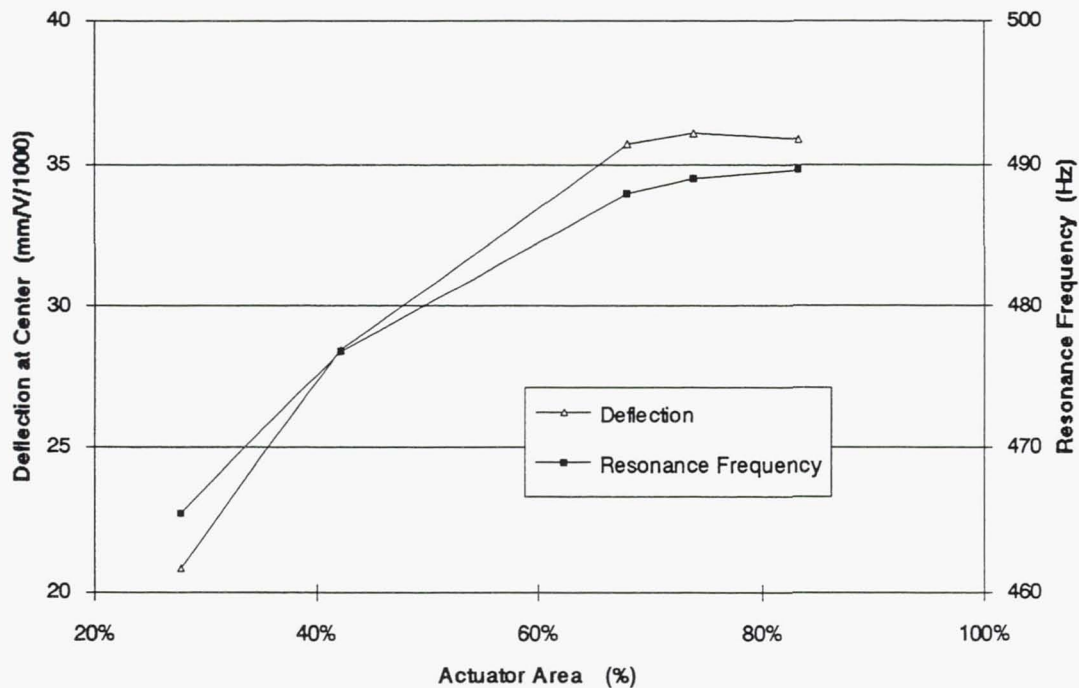


Figure 3.16. Deflection at plate center and resonance frequency versus actuator size ratio - Aluminum plate.

Deflection results for the plate follow the same trend as for the beam with the deflection reaching a maximum for an actuator area ratio of about 75%. Since the resonance frequency increases with actuator area, the change in plate deflection with actuator area would even be greater if the resonance frequency was kept constant by adjusting the plate thickness.

Since the frequency of interest is in the 500 Hz to 2 KHz range, it was decided to continue the optimization using 90×90 mm aluminum plates which represents a good compromise

between plate size, available thicknesses, resonance frequency, and performance. A 66 × 66 mm Motorola D3203HD actuator (54 % area ratio) similar to the actuator utilized during testing was used for the rest of the optimization study. This ratio is lower than the optimum ratio, but represents the largest size actuator that was available for this test. Figure 3.17 shows the resonance frequency and deflection for three 90 × 90 mm plates having thicknesses of 0.762 mm, 1.52 mm, and 2.29 mm. The actuator thickness is 0.51 mm.

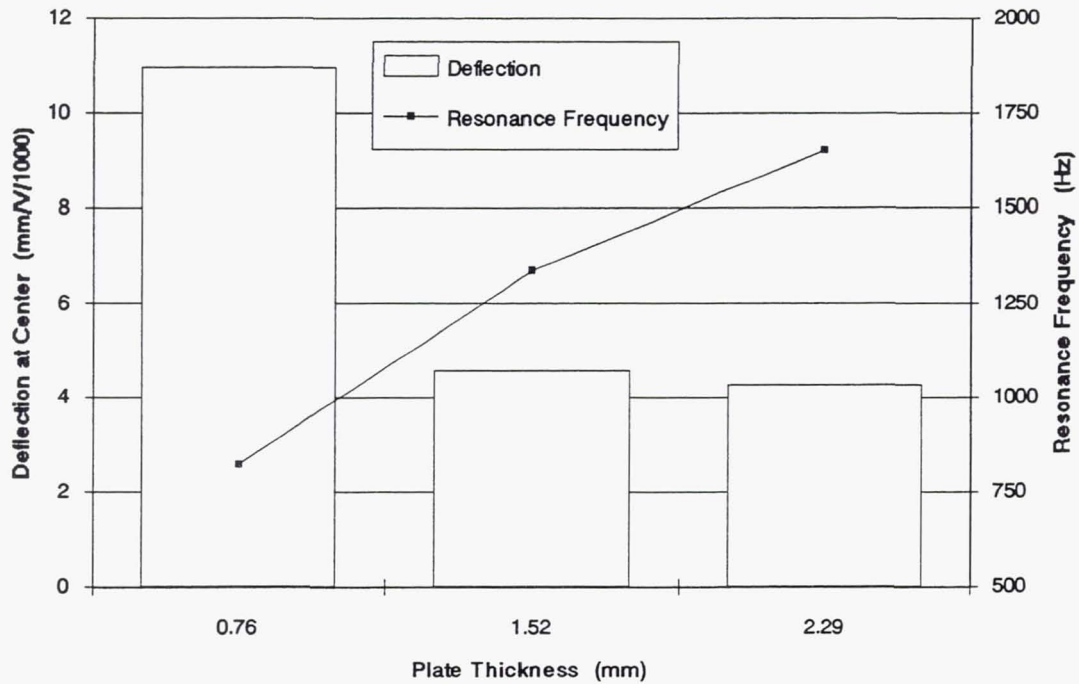


Figure 3.17 Deflection at plate center and resonance frequency versus plate thickness - Aluminum plate.

3.7.2. Effect of Actuator Thickness

The effect of actuator thickness is shown in Figure 3.18 for a 90 × 90 × 1.52 mm clamped aluminum plate with a 66 × 66 mm actuator.

Again, deflection results for the plate follow the same trend as for the beam. For a constant voltage across the actuator, the plate deflection decreases as the actuator thickness increases. However, for a constant voltage/thickness ratio across the actuator, the deflection × actuator thickness is maximum for an actuator thickness of roughly 0.28 mm which is about half the optimum actuator thickness obtained an aluminum beam of similar thickness (see Section 2.4.5).

The effect on the resonance frequency of increasing actuator thickness is for the most part that of a stiffening.

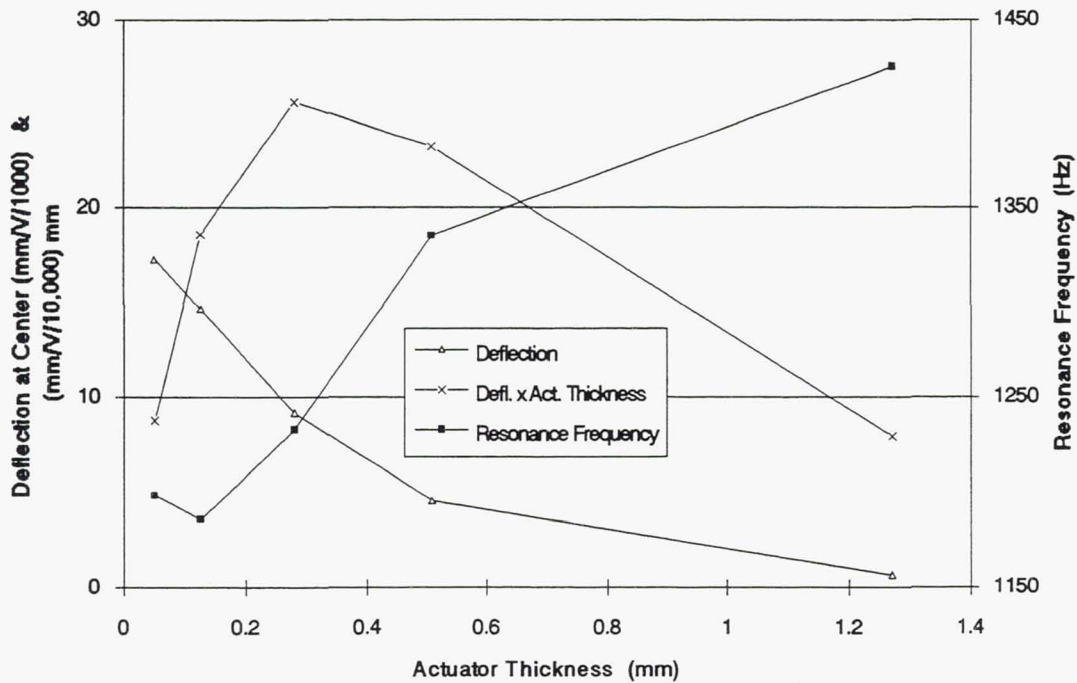


Figure 3.18. Deflection at plate center, deflection at beam center \times actuator thickness, and resonance frequency versus actuator thickness - Aluminum plate.

According to this analysis, the center deflection for a $90 \times 90 \times 1.52$ mm clamped aluminum plate with a 1% damping ratio and a $66 \times 66 \times 0.28$ mm Motorola D3203HD actuator is 1.97 mm for an actuator voltage of 100 Volts RMS (or an equivalent piston displacement of about 0.7 mm), and 3.93 mm for a voltage of 200 Volts RMS (an equivalent piston displacement of about 1.4 mm).

3.7.3 Conclusions

The plate optimization study points to an optimum aluminum plate design having a large double-sided actuator configuration (75 % actuator area ratio). The actuators are bonded at the plate center and have an optimum thickness of about 0.28-mm for a 1.52-mm thick plate. A compromise design was derived which should result in an equivalent piston displacement of 1.4 mm for an actuator voltage of 200 Volts RMS.

3.8. Experimental Evaluation of Optimized Acoustic Plate Radiators

This section describes additional results obtained with the $115 \times 100 \times 0.76$ mm and $90 \times 90 \times 1.52$ aluminum plates used for the validation of the analytical model, as well as results from a series of tests performed on 12 additional aluminum plates.

In addition to velocity response and resonance frequency measurements, the following items were investigated: plate behavior at high-voltages, harmonic distortion levels, effect of actuator number and actuator polarity, and effect of plate and actuator thickness.

3.8.1. Introduction

Plate configurations are summarized in Table 3.10 and shown in Figures 3.19 a and b.

Plate Number	Plate Material	Plate Size (mm)	PZT Actuators	Actuator Size (mm)	Bonding Material
1	Lexan	140 × 127 × 1.6	PKI-500 (×1)	49 × 25 × 0.28	GA-2
2	Aluminum	115 × 100 × 0.76	PKI-500 (×2)	49 × 25 × 0.28	GA-2
3	Aluminum	90 × 90 × 1.52	D3203HD (×2)	66 × 66 × 0.51	GA-2
4	Aluminum	90 × 90 × 1.52	D3203HD (×2)	66 × 66 × 0.51	GA-2
5	Aluminum	90 × 90 × 1.52	D3203HD (×1)	66 × 66 × 0.51	GA-2
6	Aluminum	90 × 90 × 1.52	D3203HD (×1)	66 × 66 × 0.51	Epotek 301
7	Aluminum	90 × 90 × 1.52	D3203HD (×1)	66 × 66 × 0.51	Epotek 301
8	Aluminum	90 × 90 × 1.52	D3203HD (×1)	66 × 66 × 0.25	GA-2
9	Aluminum	90 × 90 × 1.52	D3203HD (×1)	66 × 66 × 0.25	M-Bond 200
10	Aluminum	90 × 90 × 1.52	D3203HD (×1)	66 × 66 × 0.25	Epotek 301
11	Aluminum	90 × 90 × 1.52	D3203HD (×1)	66 × 66 × 0.25	Epotek 301
12	Aluminum	90 × 90 × 0.76	D3203HD (×1)	66 × 66 × 0.25	GA-2
13	Aluminum	90 × 90 × 0.76	D3203HD (×1)	66 × 66 × 0.25	M-Bond 200
14	Aluminum	90 × 90 × 0.76	D3203HD (×1)	66 × 66 × 0.25	Epotek 301
15	Aluminum	90 × 90 × 0.76	D3203HD (×1)	66 × 66 × 0.25	Epotek 301

Table 3.10. Plate configurations for experimental study.

Thirteen plates of dimensions 90 × 90 mm were fabricated and tested. As mentioned in Section 3.7.1, the plate size was chosen so that the resonance frequency of the (1,1) mode would occur between 750 Hz (0.76-mm thick plates) or around 1500 Hz (1.52-mm thick plates) which is typical of the frequencies required to cancel aircraft engine fan noise.

Most of the plate configurations tested are close to the optimal configuration derived in Section 3.7. For all plates, three bonding techniques were investigated (see Appendix A and B). In addition, tests were performed using two actuator thicknesses for the thicker plate. In several cases, two plates with similar configurations were fabricated and tested to increase the confidence in the accuracy of the results.

The actuators used were either 49 × 25 × 0.28 mm PKI-500 PZT actuators from Piezo Kinetics, or 66 × 66 mm D3203HD actuators from Motorola with thicknesses of 0.254

mm and 0.508 mm. As mentioned previously, the D3203HD material has the second highest $d_{31}Y_{11}$ product of the 36 different materials surveyed and is 43 % higher than the PKI-500 material (see Appendix C). Since the moment transmitted into the structure by the actuator is proportional to $d_{31}Y_{11}$ (see Equation 3.8), the D3203HD material should result in a plate deflection 43 % higher than the deflection obtained with PKI-500 actuator. In addition, the 250 % size difference between actuators will also translate into a higher plate deflection for the larger actuator.

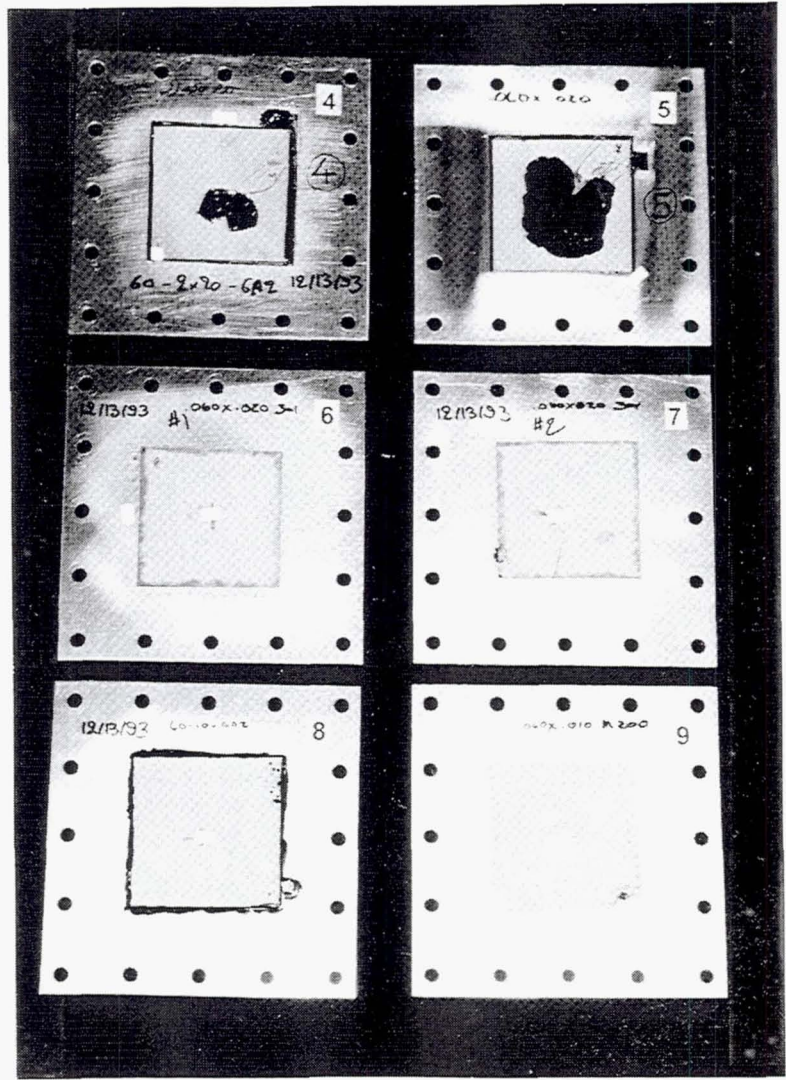


Figure 3.19a. Plate configurations for experimental study - Plates 4 to 9.

A modal analysis was performed on the plates 1, 2, and 3 only. For subsequent plates (4 to 15), only plate center and corner velocity were measured and the equivalent piston velocity was estimated using mode shape data from plates 2 and 3. During most tests, the actuator voltage was cycled several times, and then increased until actuator failure occurred to determine the plate upper voltage limit.

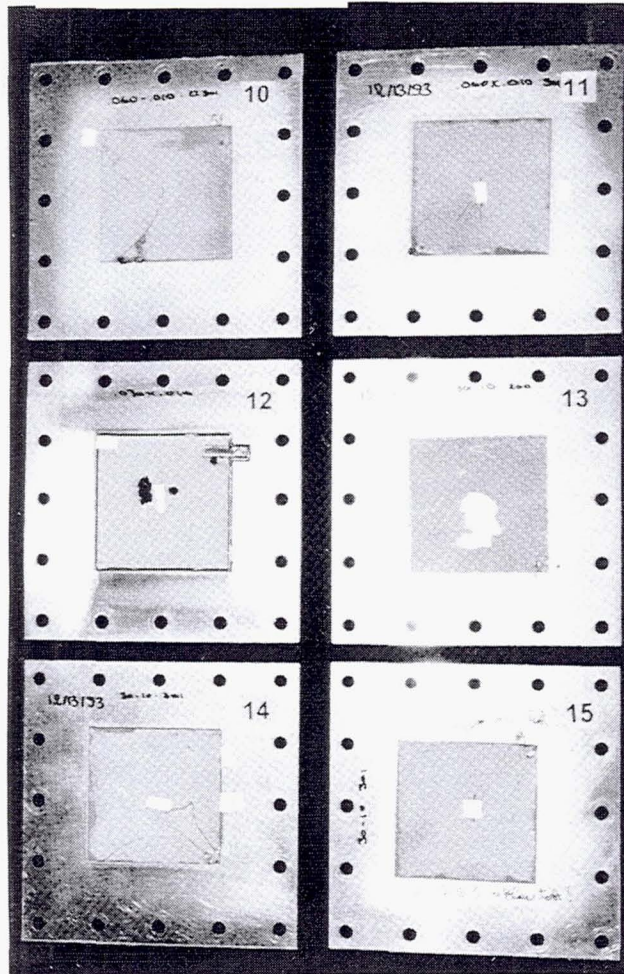


Figure 3.19b. Plate configurations for experimental study - Plates 10 to 15.

3.8.2. 100 × 115 × 0.76 mm Aluminum Plate - Plate 2

Several additional results are presented for the 100 × 115 × 0.76 mm aluminum plate.

3.8.2.1. High Actuator Voltage Tests - Plate 2

Measurements were taken with all plates to determine the equivalent piston velocity as a function of the voltage input to the actuator for the (1,1) mode.

Tests were carried out with the plate sample and laser velocimeter enclosed in an anechoic test box. A pure tone signal at the frequency of the (1,1) mode of the composite plate was sent to the actuator. Measurements of the plate velocity were taken as the voltage was cycled up and down several times. At the end of the test, the voltage was increased to the point where the actuator failed (about 100 Volts RMS).

Due to the limited dynamic range of the laser velocimeter (1 m/s), plate velocity was measured at the center and at the corner of the plate. Low-level measurements (center plate velocity lower than 1 m/s) were used to establish the ratio between center and corner velocities. This ratio was then used during high-level measurements to estimate the velocity at the plate center from corner velocity data. Equivalent piston velocity was also estimated using the (1,1) mode shape information.

At high voltage levels, the plate response was shown to have a "break-in" period and to be nonlinear.

The "break-in" period occurred as the plate center velocity response (velocity at plate center / actuator voltage) varied substantially when the actuator voltage was first increased as the composite plate "aged" as shown in Figures 3.20 and 3.21 (Test 1). The plate velocity response dropped substantially due to changes in boundary conditions, plate position, small-scale physical changes in the bond structure, and variations in the actuator electrical properties. In subsequent tests, the plate response was more stable and repeatable (within the experimental error).

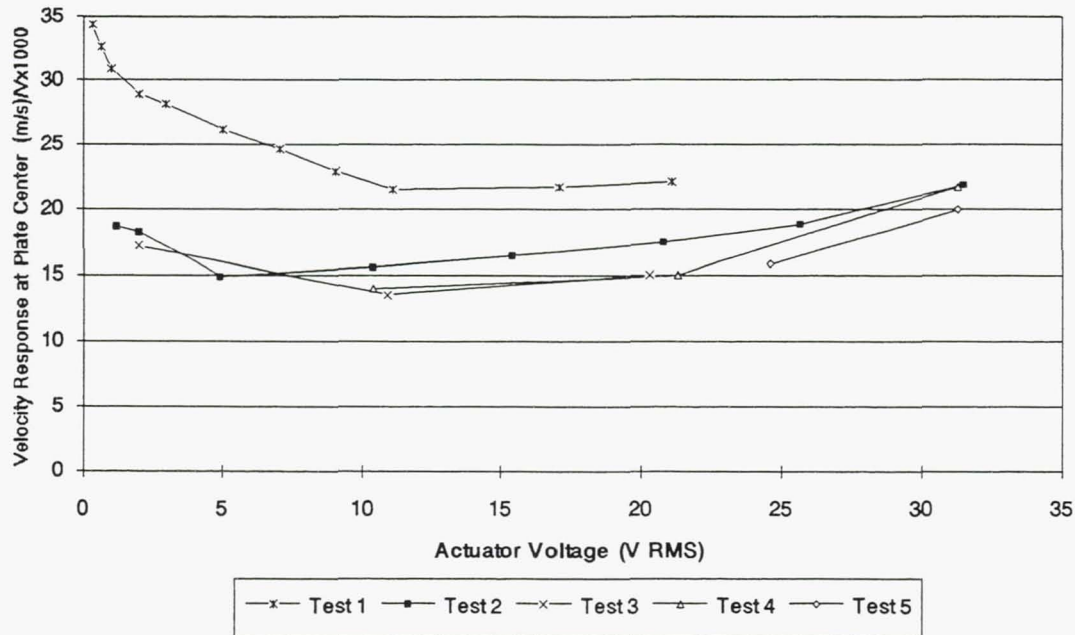


Figure 3.20. Velocity response at plate center versus actuator voltage - 100 × 115 × 0.76 mm aluminum plate.

The plate velocity response is nonlinear and often drops as the actuator voltage increases (see Figures 3.20 and 3.22). This is a result of the nonlinear behavior of the ceramic which exhibits variations in dielectric properties, coupling coefficient, and losses with temperature, voltage, and stress level. These variations can be very large with drops of up to 75 % in d_{31} for lateral stresses of $3 \cdot 10^7$ N/m² [36,37]. The magnitude of the nonlinearities is affected by the type of material used and the transducer design and

operating conditions. Some of the parameters affecting d_{31} are documented in the literature mainly for sonar transducer applications [36-41]. Parameters investigated include the direction of stresses with respect to the poling axis, whether the stresses are tensile, compressive, static, or dynamic, the magnitude of the applied electric field, and the bonding process. However, no information is available for plate transducers and limited information is available for bimorph transducers [42]. Future work on plate transducer designs should address the issues of nonlinearities at high voltage and stress levels.

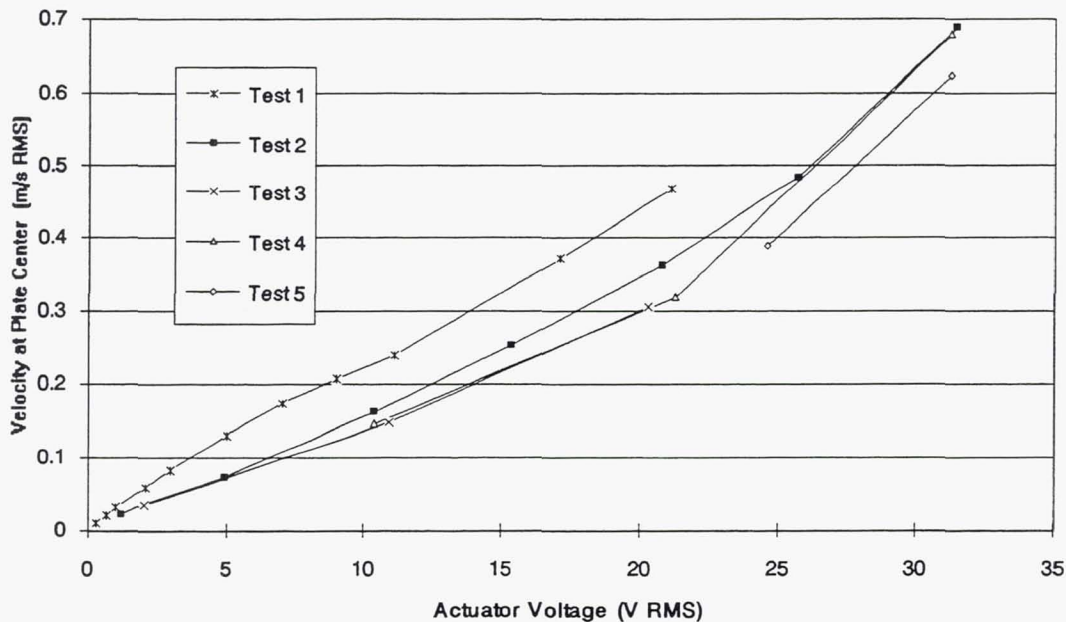


Figure 3.21. Velocity at plate center versus actuator voltage - $100 \times 115 \times 0.76$ mm aluminum plate.

The strong nonlinearity in the plate average response with actuator voltage does not translate into such a strong nonlinearity in the plate velocity waveform as shown later in this section. This points to the fact that the nonlinearities in the plate average response are due mainly to changes in the average properties of the ceramic such as temperature and do not result into the generation of harmonics of the excitation frequency.

Repeatability and measurement accuracy were a challenge as a result of: errors due to the plate "center and corner" measurement approach; small differences between plate samples such as clamping pressure and bond thicknesses; and finally the fact that a high frequency accuracy is required to measure the response of a low-damping system using pure tone excitation. Measurements on the later plate samples were more accurate than measurements on the early samples as experience was gained and as the test methodology was improved.

Plate center velocity and velocity response measurements taken at higher voltages are shown in Figures 3.22 and 3.23, with the center velocity estimated from measurements at

the plate corner. Trends are similar to the previous tests (Figure 3.20 and 3.21) with the response dropping slightly at the higher voltages.

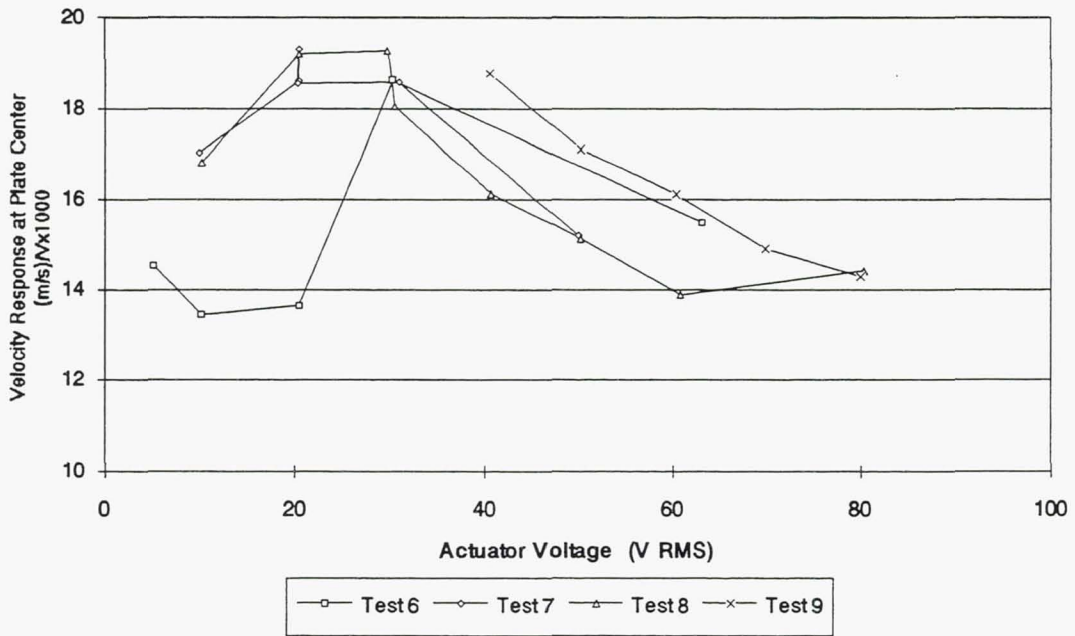


Figure 3.22. Velocity response at plate center versus actuator voltage - 100 × 115 × 0.76 mm aluminum plate.

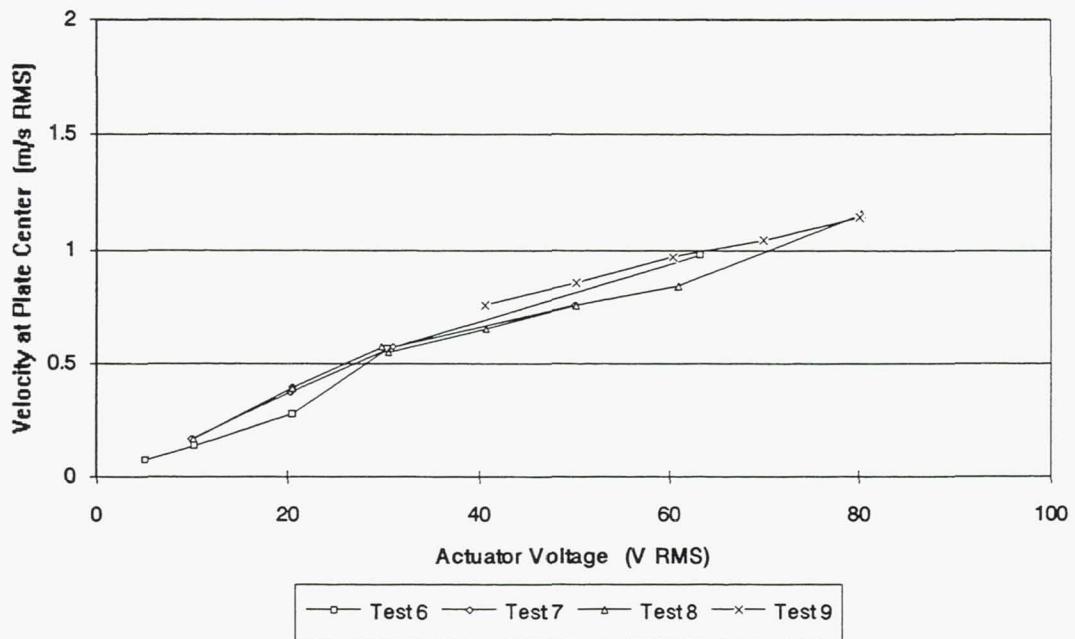


Figure 3.23. Velocity at plate center versus actuator voltage - 100 × 115 × 0.76 mm aluminum plate.

The plate response is summarized in terms of plate center velocity and equivalent piston displacement in Figure 3.24 where the response has been extrapolated to an actuator voltage of 200 Volts RMS. The equivalent piston displacement was obtained assuming a ratio of equivalent piston velocity to velocity at the plate center equal to 0.35 (see Figure 3.15) and using a conservative estimate for the velocity response at the plate center equal to 0.016 (m/s)/V.

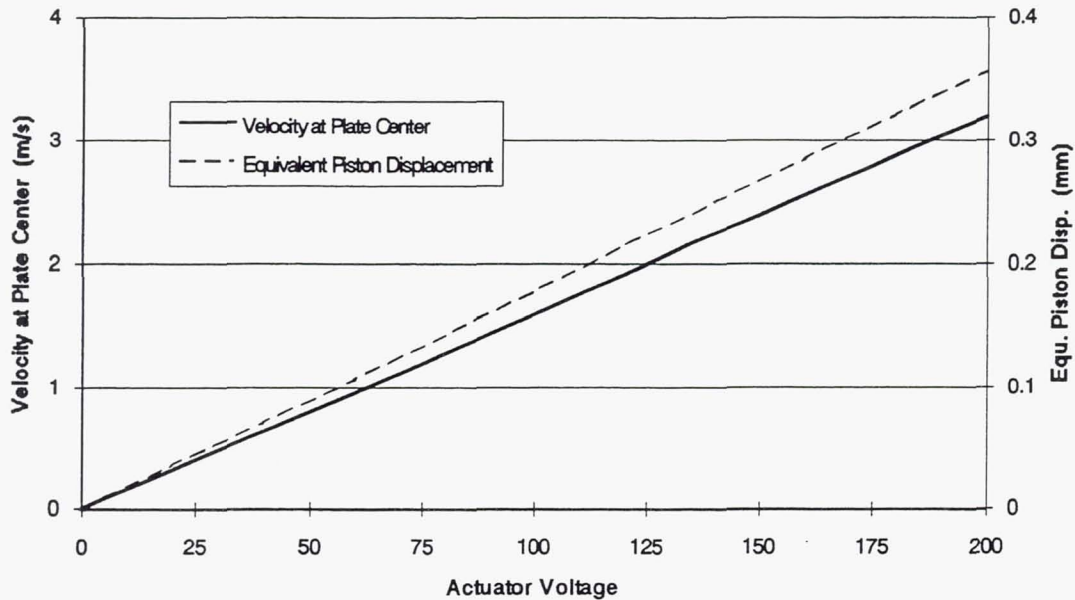


Figure 3.24. Velocity at plate center and equivalent piston displacement versus actuator voltage - $100 \times 115 \times 0.76$ mm aluminum plate.

3.8.2.2. Effect of Actuator Number and Actuator Polarity - Plate 2

Tests were performed with each PZT actuator (1 and 2 in the table below) powered individually, with both actuators powered in phase, and with both actuators powered out of phase. As with the beam experiment, this test is a good indicator of the quality and repeatability of the bonding process and of the additive effect on the response of each actuator.

Mode	Peak Response at Plate Center (mm/V) / 1000			
	1 Only	2 Only	1 and 2 Out of Phase	1 and 2 in Phase
(1,1)	2.77	2.78	5.78	0.07

Table 3.11. Effect of actuator polarity on plate response - $100 \times 115 \times 0.76$ mm aluminum plate.

The match between actuators is better than 0.5 % with the combined effect of each actuator slightly more than doubling the total response.

3.8.2.3. Harmonic Distortion - Plate 2

Harmonic distortion must be kept to a minimum since it limits the usefulness of the cancellation process by adding unwanted and uncanceled harmonics to the total noise.

Actuator Voltage (V RMS)	Peak Response at Plate Corner (Point 1)		
	Fundamental (500 Hz)	1st Harmonic (1 KHz)	2nd Harmonic (1.5 KHz)
	(m/s)	(dB)	(dB)
40.5	0.107 (0 dB)	-19	-36
80.3	0.163 (0 dB)	-17	-38

Table 3.12. Harmonic distortion - 500 Hz Excitation - 100 × 115 × 0.76 mm aluminum plate.

Harmonic distortion is only significant for high actuator voltages. For an actuator RMS voltage of 80 Volts, the level of the first harmonic is 17 dB below the level of the fundamental which effectively puts a 17-dB limit on the maximum noise cancellation achievable with this source at this particular actuator voltage. In general, the lower the noise level to be canceled, the lower the actuator voltage and harmonic distortion, and the higher the maximum noise cancellation achievable.

3.8.3. 90 × 90 × 1.52 mm Aluminum Plate - Plate 3

Several additional results are presented for the 90 × 90 × 1.52 mm aluminum plate.

3.8.3.1. High Actuator Voltage Tests - Plate 3

The overall response of plate 3 is similar to plate 2 with a strong variation of the resonance frequency of mode (1,1) with actuator voltage, and a definite drop in plate velocity response with increasing actuator voltage.

The actuator voltage, velocity at the plate center, and velocity response at the plate center are shown in Figures 3.25 and 3.26. Results were obtained by taking measurements at discrete frequency points with the amplifier settings unchanged. As opposed to the previous tests using the PKI 500 actuator, the high capacitance of the Motorola actuator results in a voltage drop around the plate resonance frequency and limits the maximum voltage available to power the actuator. As shown in Figure 3.26, the maximum response occurs at the same frequency as the minimum actuator voltage.

Figure 3.27 shows the plate resonance frequency as a function of actuator voltage with each actuator powered individually. For each data point, the resonance frequency was identified by slightly varying the excitation frequency until a minimum in the actuator voltage was found. The resonance frequency and velocity at the plate center were then recorded.

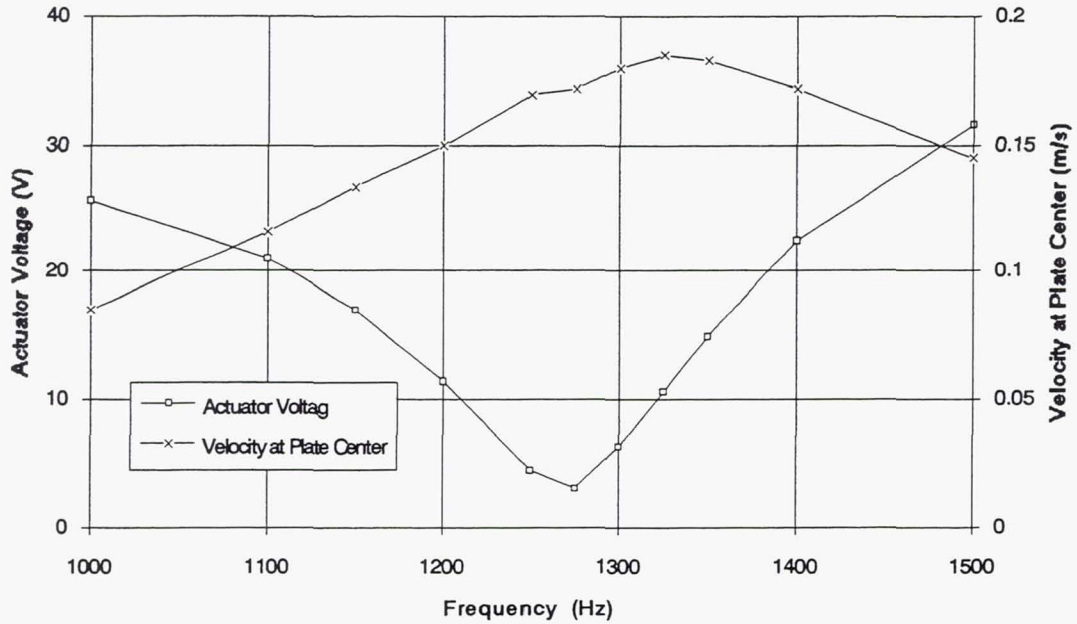


Figure 3.25. Actuator voltage and velocity at plate center versus frequency - Plate 3.

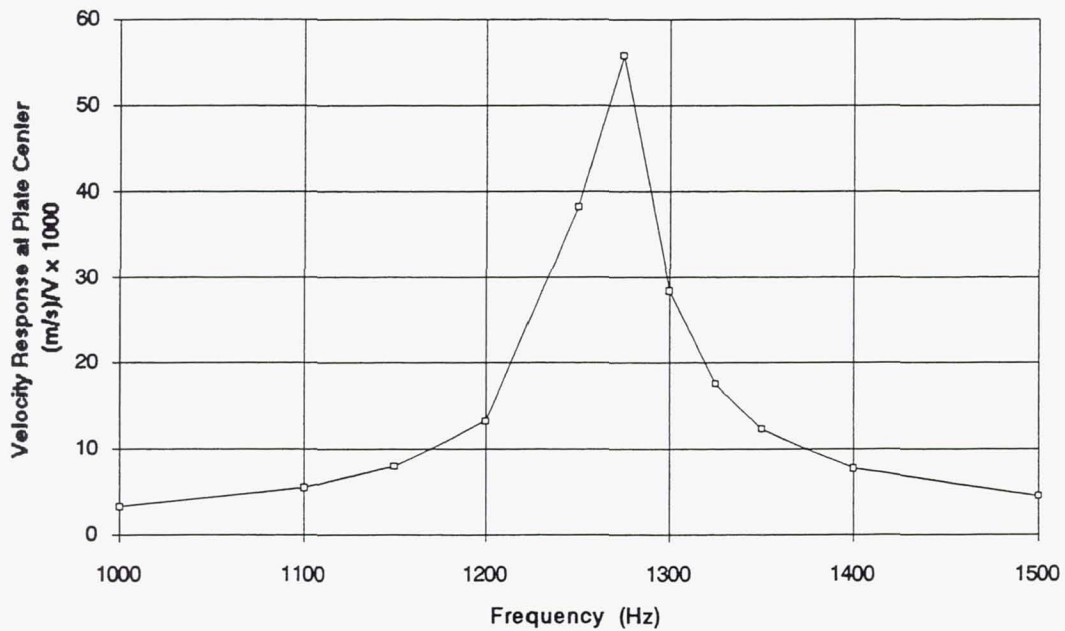


Figure 3.26. Velocity response at plate center versus frequency - Plate 3.

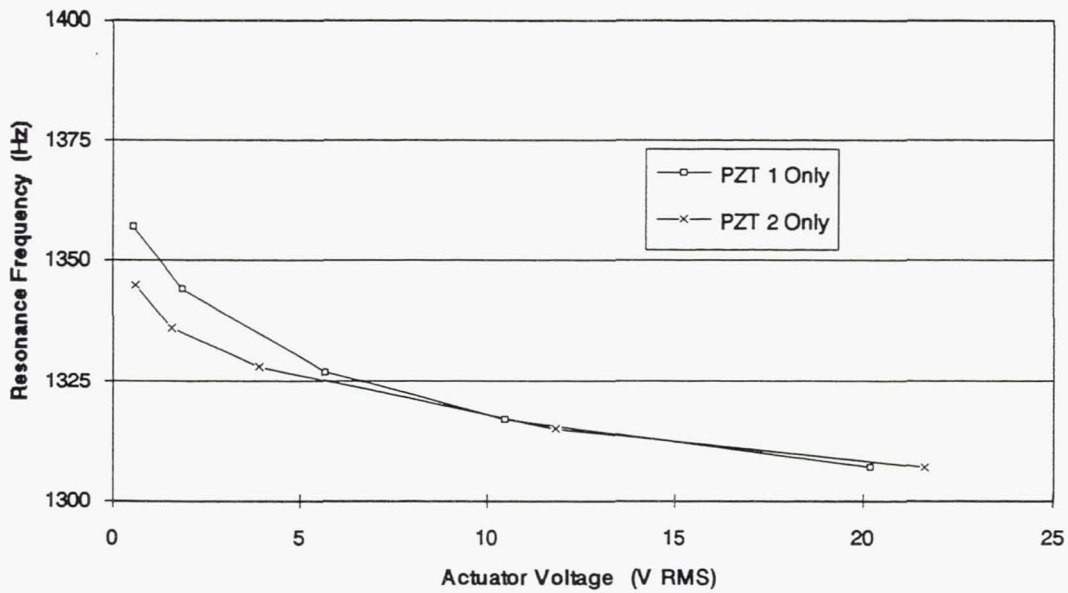


Figure 3.27. Plate resonance frequency versus actuator voltage - Plate 3.

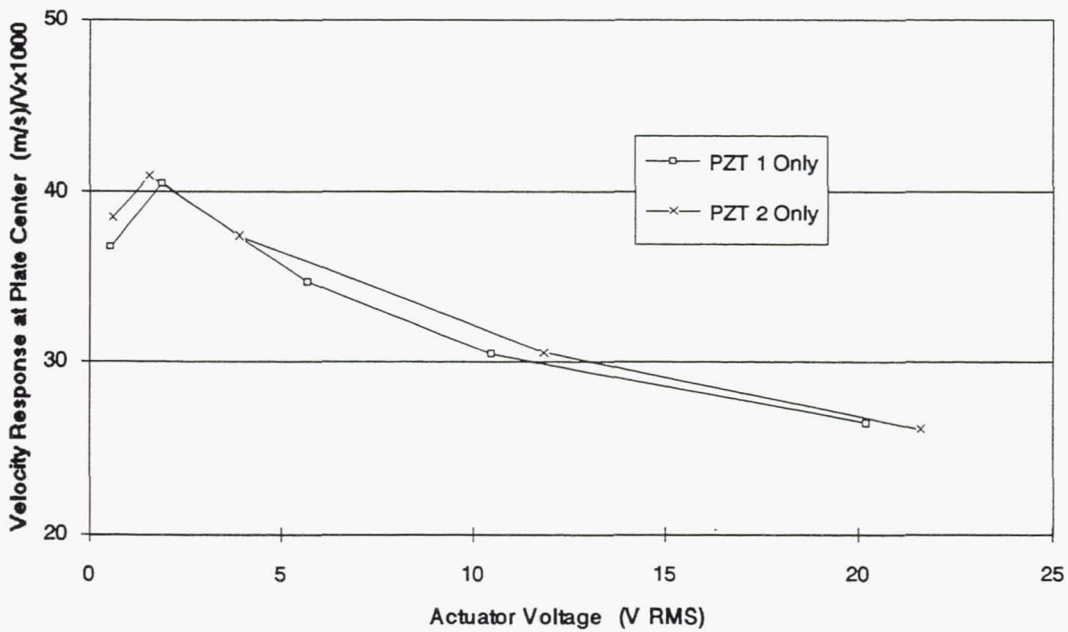


Figure 3.28. Velocity response at plate center versus actuator voltage - Plate 3.

The strong dependence of the resonance frequency on the actuator voltage as well as the change in resonance frequency depending on whether only one or both actuators are powered indicates that the electrical and mechanical properties of the actuator and power supply are strongly coupled for this system. This coupling is due in part to the fact that the Young's Modulus of the piezoceramic depends on the electrical field [43]. Therefore, the electronic circuitry driving the actuator affects its stiffness, which in turn affects the

resonance frequency of the plate. More work should be done in this area to quantify the magnitude of these changes.

As with plate 2, the velocity response drops substantially as the actuator voltage is increased as a result of the nonlinear behavior of the ceramic (Figure 3.28) [36-41].

3.8.3.2. Effect of Actuator Number and Actuator Polarity - Plate 3

Table 3.13 shows the individual and combined effect of each actuator measured at low actuator voltages:

	Peak Response at Plate Center (mm/V) / 1000
PZT 1 Only	5.01
PZT 2 Only	5.16
PZT 1 and 2 Out of Phase	9.80

Table 3.13. Effect of actuator polarity on plate response - Plate 3

The match between actuators is better than 3 % with the combined effect of each actuator equal to 96 % of the sum of the individual responses.

3.8.4. 90 × 90 mm Aluminum Plates - Plates 4 to 15

Plate Number	Plate Thickness (mm)	Number of Actuators	Actuator Thickness (mm)	Bonding Material
3	1.52	2	0.51	GA-2
4	1.52	2	0.51	GA-2
5	1.52	1	0.51	GA-2
6	1.52	1	0.51	Epotek 301
7	1.52	1	0.51	Epotek 301
8	1.52	1	0.25	GA-2
9	1.52	1	0.25	M-Bond 200
10	1.52	1	0.25	Epotek 301
11	1.52	1	0.25	Epotek 301
12	0.76	1	0.25	GA-2
13	0.76	1	0.25	M-Bond 200
14	0.76	1	0.25	Epotek 301
15	0.76	1	0.25	Epotek 301

Table 3.14. 90 × 90 mm aluminum plate configurations

Table 3.14 summarizes the 90 × 90 mm aluminum plate configurations tested. Plates 3 to 11 have resonance frequencies around 1500 Hz. Since the analytically determined optimum actuator thickness for this configuration is about 0.3 mm, actuator thicknesses of 0.51 mm and 0.25 mm (20 and 10 mils) were used for these tests. In most cases only one actuator was bonded to the plate to minimize fabrication time and cost, and to simplify testing. Plates 12 to 15 have resonance frequencies around 750 Hz.

3.8.4.1. Mode Shapes and Equivalent Piston Velocity

Since no modal analysis was performed for plates 4 to 15, equivalent piston velocity was estimated using velocity measurements at the plate center and mode shape information obtained with plates 2 and 3. Table 3.15 shows the ratio of equivalent piston velocity to velocity at the plate center for the (1,1) mode for plates 1,2, and 3 (experimental data), and for plates with clamped and simply-supported boundary conditions (approximate analytical model). After examination of the results listed in Table 3.15, an average ratio equal to 0.35 was chosen for plates 4 to 15.

	<u>Equivalent Piston Velocity</u> Velocity at Plate Center
1 - Lexan - 140 × 127 × 1.6 mm (Exp.)	0.40
2 - Al. - 100 × 115 × 0.76 mm (Exp.)	0.35
3 - Al. - 90 × 90 × 1.52 mm (Exp.)	0.36
Simply Supported Plate (Anal.)	0.41
Clamped Plate (Anal.)	0.17
Plates 4 to 15	0.35

Table 3.15. (Equivalent piston velocity / velocity at plate center) for (1,1) mode - Plates 1,2, 3, and clamped and simply-supported plates.

3.8.4.2. 1.52 mm Thick Aluminum - 0.51-mm Actuator - Plates 3 to 7

Figures 3.29 to 3.31 show the results for the 1.52-mm thick plates with 0.51-mm actuators.

The (1,1) mode resonance frequency varies substantially among plates even when identical bonding procedures and materials are used. This variation is due to small differences among plates and plate boundary conditions. Fine tuning through boundary condition and mass and stiffness adjustment might therefore be necessary to provide a homogeneous source array for an aircraft engine application. As mentioned in the previous section, the

resonance frequency and the plate velocity response drop with increasing actuator voltage (Figure 3.30). The velocity response becomes stable when the actuator voltage reaches 15 Volts RMS which is well below the maximum recommended voltage limit (the coercive field for D3203HD is 1063 V/mm).

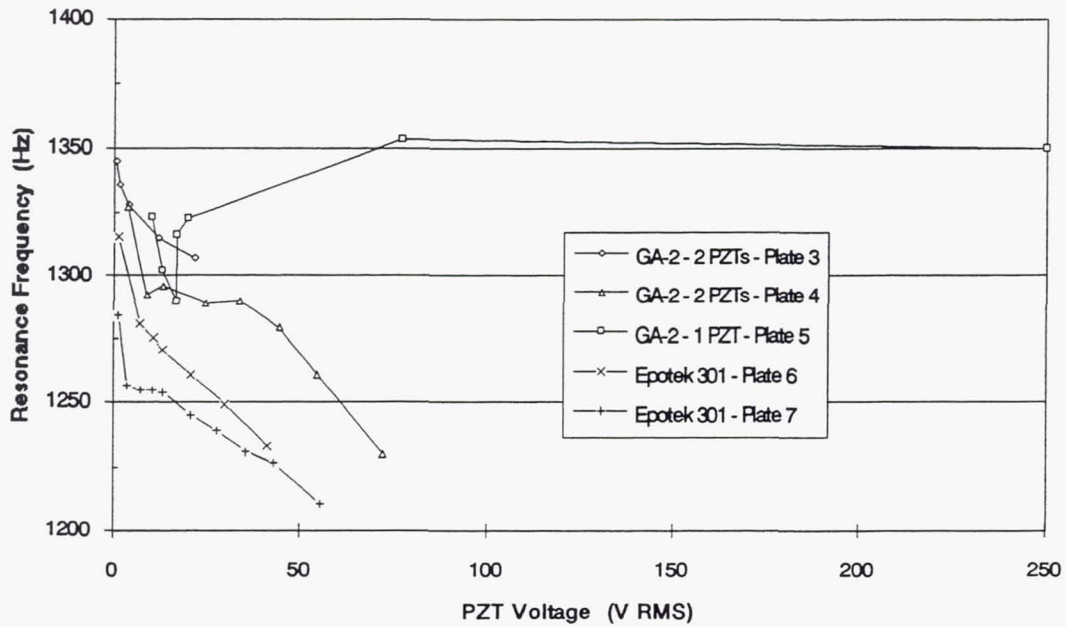


Figure 3.29. Resonance frequency versus actuator voltage - Plates 3 to 7.

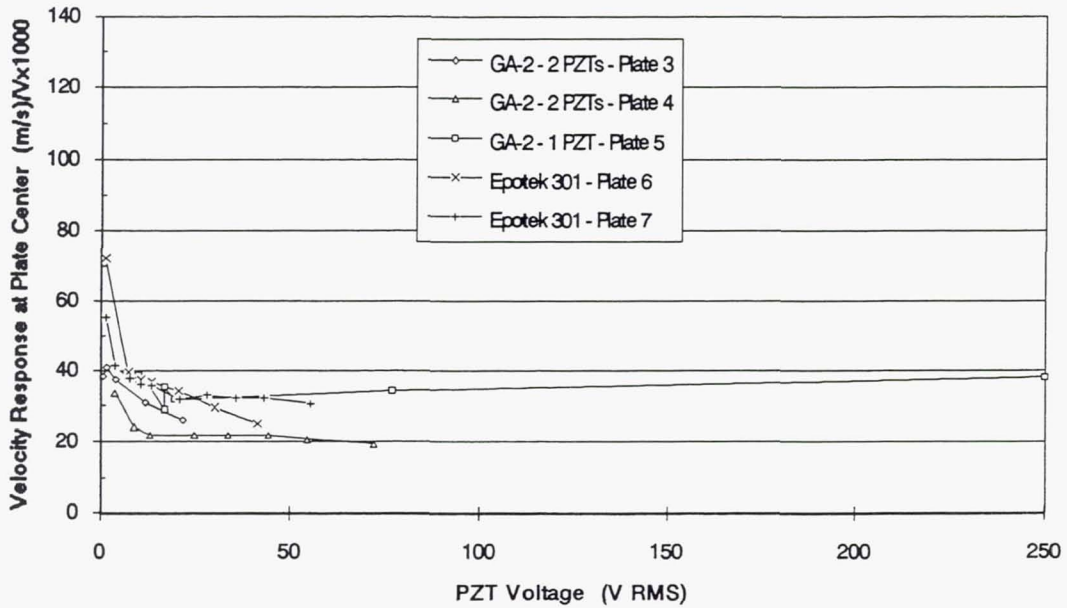


Figure 3.30. Velocity response at plate center versus actuator voltage - Plates 3 to 7.

Testing with plates 3 and 4 was performed with only one actuator powered which explains the lower velocity response for those plates. As shown previously, powering both actuators out of phase results in a doubling in velocity response at low voltages, although the advantage of using two actuators usually drops by as much as 30% for high actuator voltages.

For plate 5, the equivalent piston displacement was as high as 0.4 mm at 250 Volts RMS. However, this high displacement was not repeated with the other plates which failed for much lower actuator voltages. As can be seen in Figure 3.29, a sudden change occurred in the plate response when the actuator voltage reached 20 Volts. This is most probably due to a crack in the actuator ceramic which effectively reduced the actuator "powered" area and capacitance, allowing the power supply to provide the high voltages resulting in the large plate displacements.

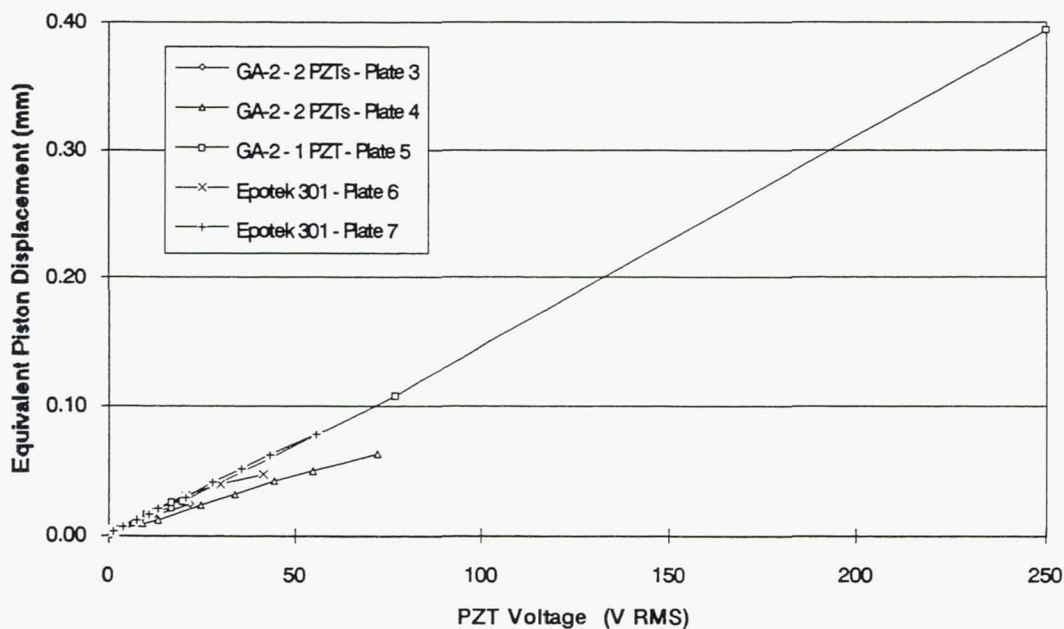


Figure 3.31. Equivalent piston displacement versus actuator voltage - Plates 3 to 7.

Failure occurred for different actuator voltages, and in different manners for each plate. Plate 3 was not tested at high voltages since it was also to be used in the adaptive tuning test rig. Plates 4 and 5 used the GA-2 epoxy and failed around 80 Volts RMS and 250 Volts RMS respectively. In both cases, large cracks developed and the actuator shattered with debonding occurring at the center. Plate 6 failed around 50 Volts RMS when the copper electrode broke. No cracks developed in the actuator. Plate 7 failed around 80 Volts RMS when two large cracks formed from one corner of the actuator to its center. The failure voltages are only approximate. An "actuator failure" diagnostic was made when a sudden change in response or electrical properties occurred due to cracks or sudden debonding of the actuator.

Since the maximum voltage applied to the actuator was always below the maximum recommended voltage limit (except for plate 5), failure is a result of stresses in the ceramic being too high, with cracks usually occurring along parabolic lines going from one corner of the ceramic to the other through its center.

3.8.4.3. 1.52 mm Thick Aluminum - 0.25-mm Actuator - Plates 8 to 11

Figures 3.32 to 3.34 show results for 1.52-mm thick plates with a one-sided 0.25-mm actuator configuration.

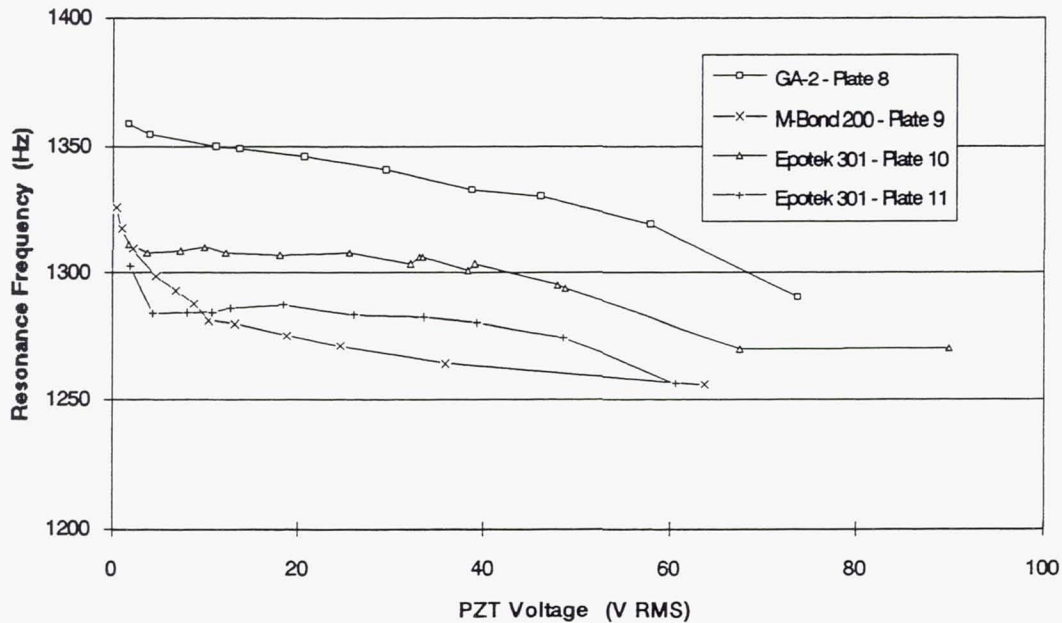


Figure 3.32. Resonance frequency versus actuator voltage - Plates 8 to 11.

Again, the resonance frequency varies substantially between plates, dropping with increasing actuator voltage. The velocity response (Figure 3.33) is fairly stable except for plate 9 (M-Bond 200). As expected and as predicted by the analysis, the velocity response is higher than with the 0.51-mm thick actuators. However, since in this configuration the plates are not "voltage limited" but "stress limited", there is no advantage in using the thicker actuators.

For plate 10, the equivalent piston displacement was as high as 0.3 mm at 90 Volts RMS. However, similar to plate 5, this high displacement was not repeated with the other plates and is a result of an unexplained sudden change in plate and actuator properties.

Plate 8 (GA-2) failed around 90 Volts RMS with multiple cracks developing at the center of the actuator. The center of the actuator on plate 9 debonded around 65 Volts RMS. Plates 10 and 11 failed around 100 Volts RMS and 80 Volts RMS respectively, due to

shorting occurring along small cracks running from the corners of the actuator to its center.

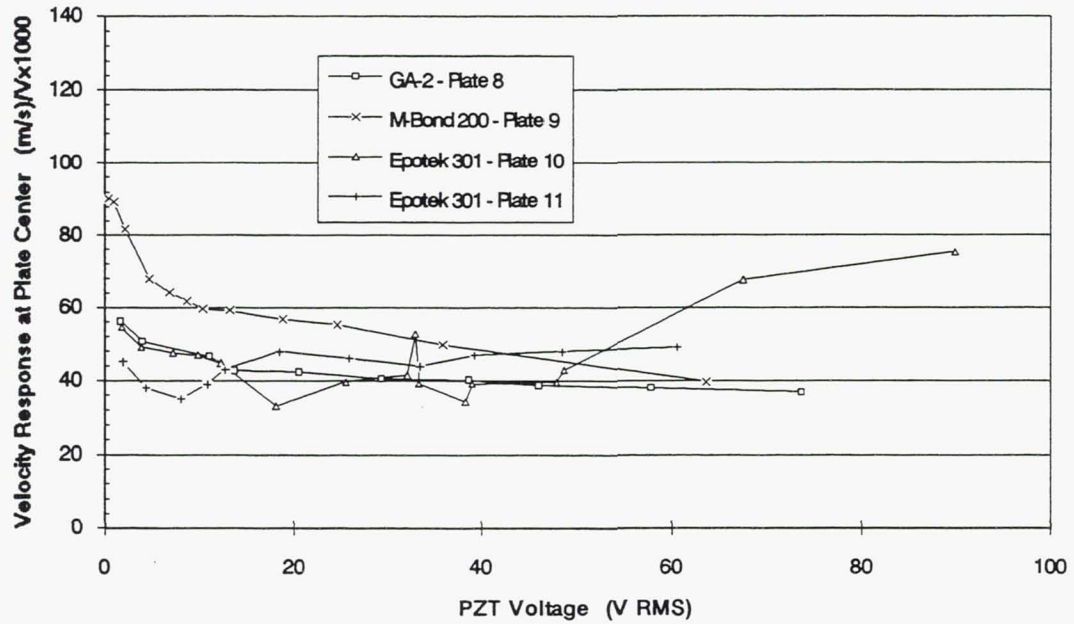


Figure 3.33. Velocity response at plate center versus actuator voltage - Plates 8 to 11.

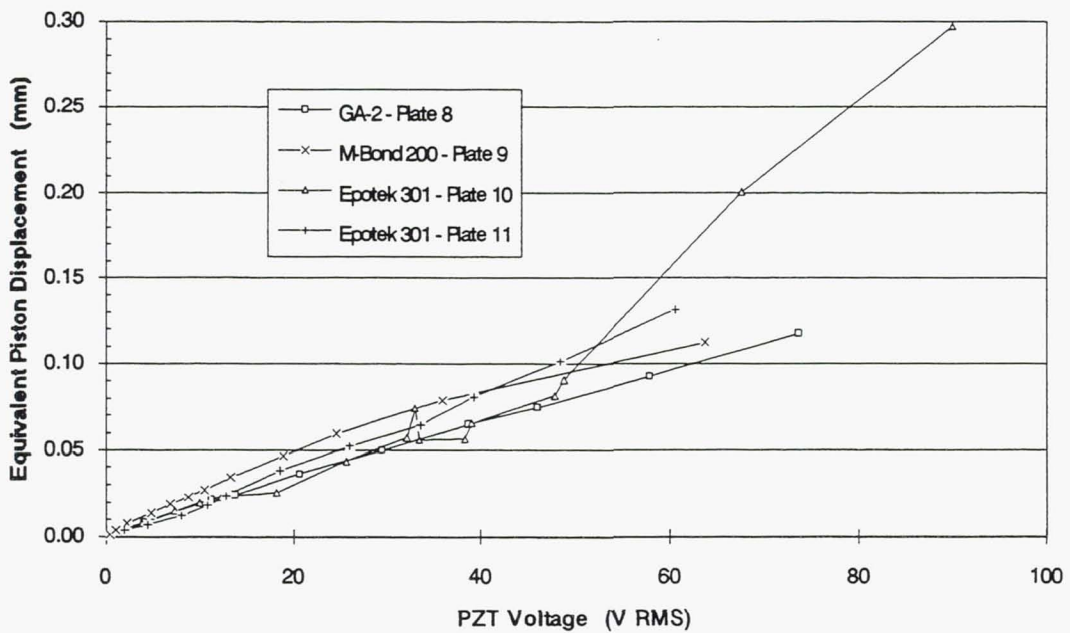


Figure 3.34. Equivalent piston displacement versus actuator voltage - Plates 8 to 11.

The harmonic distortion of the plate corner velocity was measured for plates 9 and 10 for several actuator voltages:

Plate Number	Actuator Voltage (V RMS)	Harmonic Distortion at Plate Corner				
		Fund. (dB)	1st Har. (dB)	2nd Har. (dB)	3rd Har. (dB)	4th Har. (dB)
9	64	0	-21.6	-26.0	-21.1	-39.6
10	10	0	-20.4	-	-	-
10	18	0	-26.0	-	-	-

Table 3.16. Harmonic distortion - Plates 9 and 10.

3.8.4.4. 0.76 mm Thick Aluminum - 0.25-mm Actuator - Plates 12 to 15

Figures 3.35 to 3.37 show results for 0.76-mm thick plates with a one-sided 0.25-mm actuator configuration.

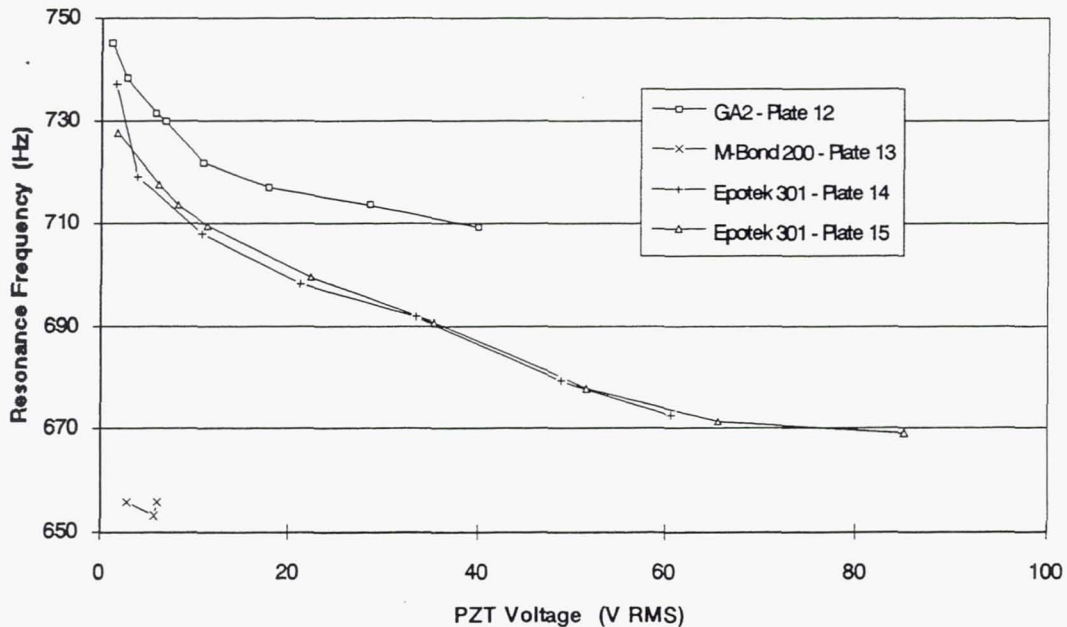


Figure 3.35. Resonance frequency versus actuator voltage - Plates 12 to 15.

The resonance frequency and velocity response both drop substantially with increasing actuator voltage, with the velocity response drop being more pronounced than with the 1.52-mm thick plates. As expected, the velocity response is higher than with the thicker plates although there are substantial differences between plates with different bonding

materials. Nonlinearities in the response and differences between plates are also clear when looking at the equivalent piston displacement shown in Figure 3.37.

Equivalent piston displacement was as high as 0.28 mm at 85 Volts RMS for plate 15.

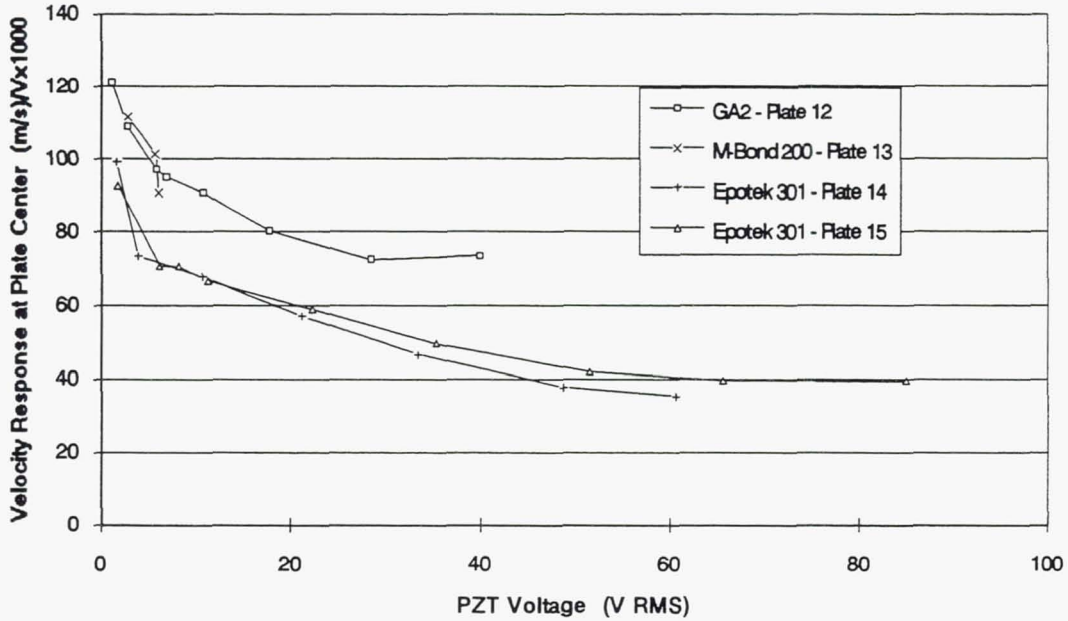


Figure 3.36. Velocity response at plate center versus actuator voltage - Plates 12 to 15.

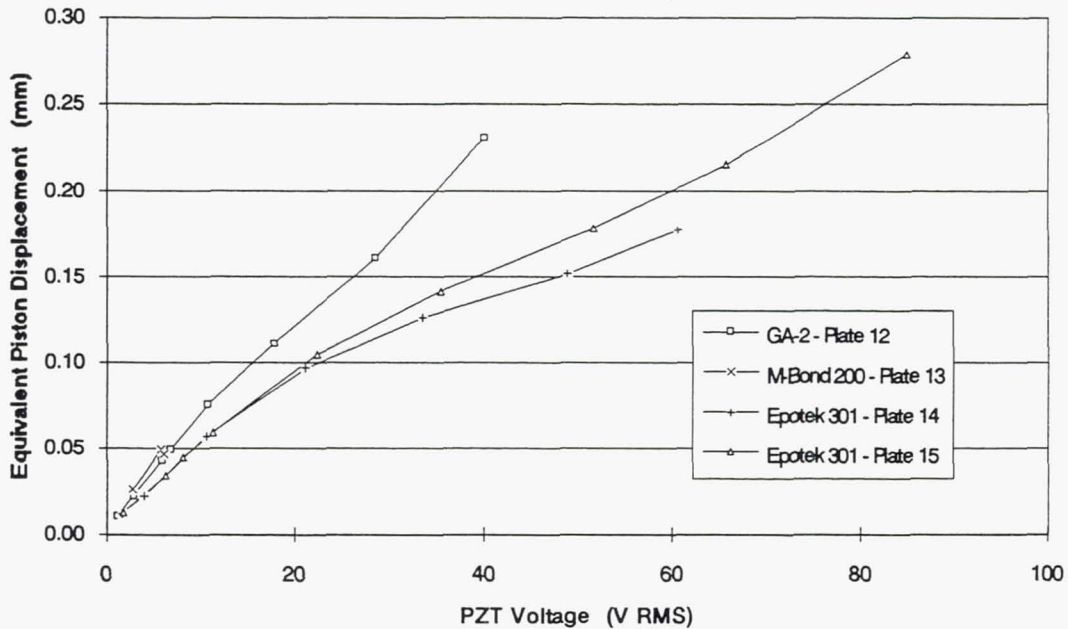


Figure 3.37. Equivalent piston displacement versus actuator voltage - Plates 12 to 15.

Plates 12 and 13 failed around 50 Volts RMS and 40 Volts RMS respectively with the center of the actuator debonding. Plate 14 and 15 failed around 70 Volts RMS and 90 Volts RMS respectively due to shorting along small multiple cracks.

Harmonic distortion of the plate corner velocity was measured for plate 15 and is shown in Table 3.17.

Actuator Voltage (V RMS)	Harmonic Distortion at Plate Corner			
	Fund. (dB)	1st Har. (dB)	2nd Har. (dB)	3rd Har. (dB)
8	0	-21.8	-28.8	-
22	0	-18.3	-25.6	-21.7
35	0	-14.6	-22.5	-17.2

Table 3.17. Harmonic distortion - Plate 15.

Harmonic distortion is high which is consistent with the high level of nonlinearity in plate response.

3.8.5 Summary - Plate Experimental Results

Tables 3.18 and 3.19 summarize the experimental results for plates 1 through 15.

3.9. Stresses in the Aluminum/Piezoceramic Radiator.

Stress levels in the plate and in the actuator were investigated numerically for a typical optimized plate and compared with critical stress values for the piezoceramic.

The ANSYS FEM code used to calculate the forced response of the plate (Section 3.4) was also used to obtain the stresses acting on the plate and piezoceramic actuator. Element "type 63" was used and the boundary conditions were modeled through linear and torsional springs.

In a rigorous analysis, the plate, bonding layers, and piezoceramic actuators would be modeled individually and employing the compatibility of displacements used to compute the stresses in the composite structure. However, such an approach is very time consuming and requires a large amount of CPU time. In fact, the stress analysis can be greatly simplified by recognizing the following factors:

- The thickness of the bonding layer is small compared to the thickness of the actuator or of the plate. Therefore, we can assume that the shear force between the actuator and the underlying plate is transferred perfectly.

	Plate Number						
	1	2	3	4	5	6	7
Plate Material	Lexan	Al.	Al.	Al.	Al.	Al.	Al.
Plate Size (mm)	140×127	115×100	90×90	90×90	90×90	90×90	90×90
Plate Thickness (mm)	1.6	0.76	1.52	1.52	1.52	1.52	1.52
Actuator Material	PKI-500	PKI-500	D3203HD	D3203HD	D3203HD	D3203HD	D3203HD
Actuator Size (mm)	49×25	49×25	66×66	66×66	66×66	66×66	66×66
Actuator Thickness (mm)	0.28	0.28	0.51	0.51	0.51	0.51	0.51
Number of Actuators	1	2	2	2	1	1	1
Number of Actuators Powered	1	2	1	1	1	1	1
Bonding Material	GA-2	GA-2	GA-2	GA-2	GA-2	Epotek 301	Epotek 301
(1,1) Mode Resonance Frequency (Hz)	166	500	1300-1400	1230-1330	1320-1350	1230-1320	1210-1280
(1,1) Mode Damping (%)	2.3	1.4	0.94	-	-	-	-
Center Vel. Resp. - Low Volt. (mm/s)/V *	4	35	58	34	-	72	55
Center Vel. Resp. - High Volt (mm/s)V *		15-20	25-40	19-22	29-38	25-37	30-36
Max. Equ. Piston Disp. (mm)		0.13	-	0.06	0.39	0.05	0.08
Maximum Actuator Voltage (V RMS)		80	-	72	250	41	55
Harmonic Level (dB)		< -17 (80 V)	-	-	-	-	-
Approx. Failure Voltage (V RMS)	-	100	-	80	80-250	50	80
Failure Mode	-	Debonding	-	Debonding	Debonding	Broken electrode	Large cracks

Table 3.18. Summary of plate results - Plates 1 to 7

	Plate Number							
	8	9	10	11	12	13	14	15
Plate Material	Al.	Al.	Al.	Al.	Al.	Al.	Al.	Al.
Plate Size (mm)	90×90	90×90	90×90	90×90	90×90	90×90	90×90	90×90
Plate Thickness (mm)	1.52	1.52	1.52	1.52	0.76	0.76	0.76	0.76
Actuator Material	D3203HD	D3203HD	D3203HD	D3203HD	D3203HD	D3203HD	D3203HD	D3203HD
Actuator Size (mm)	66×66	66×66	66×66	66×66	66×66	66×66	66×66	66×66
Actuator Thickness (mm)	0.25	0.25	0.25	0.25	0.25	0.25	0.25	0.25
Number of Actuators	1	1	1	1	1	1	1	1
Number of Actuators Powered	1	1	1	1	1	1	1	1
Bonding Material	GA-2	M-Bond 200	Epotek 301	Epotek 301	GA-2	M-Bond 200	Epotek 301	Epotek 301
(1,1) Mode Resonance Frequency (Hz)	1290-1360	1260-1330	1270-1310	1255-1305	710-745	650	670-740	670-730
(1,1) Mode Damping (%)	-	-	-	-	-	-	-	-
Center Vel. Resp. - Low Volt. (mm/s)/V	56	90	55	45	121	112	99	93
Center Vel. Resp. - High Volt (mm/s)/V	37-46	40-60	33-75	39-49	74-91	-	35-68	39-67
Max. Equ. Piston Disp. (mm)	0.12	0.11	0.30	0.13	0.23	0.05	0.18	0.28
Maximum Actuator Voltage (V RMS)	74	64	90	61	40	6	61	85
Harmonic Level (dB)	-	< -21 (64 V)	< -20 (10 V)	-	-	-	-	< -15 (35 V)
Approx. Failure Voltage (V RMS)	90	65	100	80	50	40	70	90
Failure Mode	Cracks	Debonding	Small cracks	Small cracks	Debonding	Debonding	Small cracks	Small cracks

Table 3.19. Summary of plate results - Plates 8 to 15

* : Low voltage: < 10 Volts
 High Voltage: > 10 Volts

- The Young's Modulus of the ceramic actuator and the aluminum plate structure are the same for the current configuration.

The current approach computes the smeared Young's Modulus and density for the actuator/plate composite section (as in Equations 3.10 and 3.11). Because the stresses of interest are the stresses in the actuator, t_{eff} in Equations 3.10 and 3.11 is equal to the true thickness of the actuator/plate composite region. Since t_{eff} is taken as the actual thickness of the composite section, the Young's modulus of the actuator, of the plate, and the smeared Young's Modulus of the composite section are all equal.

The smeared density however is in-between the density of the piezoceramic actuator and the density of the aluminum plate. Since the density of the actuator is higher than that of the plate, the smeared density would be lower in the region occupied by the actuator. Hence, the estimates for the dynamic stresses for the actuator region should be slightly lower than the actual levels. However, the relative error due to the density smearing is small and is neglected in this analysis since stiffness effects are dominant compared to inertia effects for stress computation.

The stress analysis was performed on an optimized aluminum plate similar to several of the plates tested. The forcing moments per unit length m_x and m_y induced by the actuators were calculated using Equation 3.9. The linear and torsional spring stiffnesses were set so that the resonance frequency of the system matched the experimental data.

Plate Dimensions	90 × 90 × 1.52 mm
Actuator Configuration	Double-sided - 66 × 66 × 0.25 mm
Bond Thickness	0.076 mm - Epoxy
Forcing Moments	0.053 (N·m/m).
Linear Spring Stiffness	4.8·10 ⁹ N/m
Torsional Spring Stiffness	58 N/rad
Damping Ratio	0.9 %
Resonance Frequency - Mode (1,1)	1317 Hz

Table 3.20. Acoustic plate radiator physical properties - characteristics - Stress analysis

The stresses for the plate are shown in Figure 3.38. The contour plot shows the effective Tresca stresses which are the stresses which would cause failure in the plate [44]. The stresses were computed as follows: If the principle stresses at one point are σ_1 , σ_2 , and σ_3 , and

$$\sigma_1 > \sigma_2 > \sigma_3 \quad (3.14)$$

then, the Tresca failure criterion states that

$$TS = (\sigma_1 - \sigma_3) \leq \sigma_{\text{Failure}} \quad (3.15)$$

where TS is the Tresca stress and σ_{Failure} is the 1-D failure stress for the particular material under consideration. The Tresca stress is therefore a measure of the maximum shear stresses occurring in the material. Since piezoceramic materials are brittle in nature, we can also use the maximum tensile stress criteria which states that $\sigma_1 \leq \sigma_{\text{Failure}}$. However, since $\sigma_3 = 0$ at the point of maximum stress, the Tresca criterion and the maximum stress criterion have the same result.

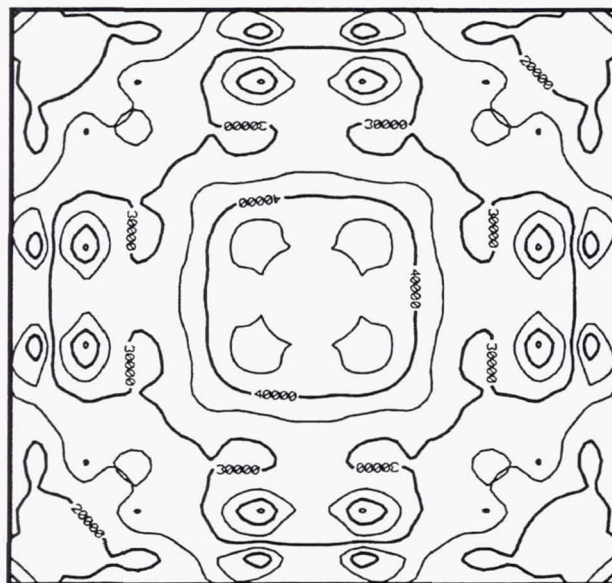


Figure 3.38. Tresca stresses in acoustic plate radiator

Figure 3.38. shows the stresses at the centroid of each element used in the FEM analysis. The centroid stresses rather than the nodal stresses are used because nodal stresses at the interface between the bare and the composite plate can be computed only by averaging the stresses in the neighboring elements which is not meaningful for this analysis.

The maximum stress in the plate is equal to $6.78 \cdot 10^4$ (N/m²)/V and occurs at the center of the actuator. This corresponds to a stress of $6.78 \cdot 10^6$ N/m² for an actuator voltage of 100 Volts, and $1.36 \cdot 10^7$ N/m² for an actuator voltage of 200 Volts. Maximum recommended tensile and compressive stresses for piezoceramic actuators vary substantially depending on material, manufacturer, electrical and mechanical environment, and the application. Typical critical strengths obtained from manufacturer documentation for middle-of-the-line materials (such as the PKI-500) are in the $0.8\text{-}4.6 \cdot 10^7$ N/m² range for tensile loads and in the $1.4\text{-}1.4 \cdot 10^8$ N/m² range for compressive loads [43,39].

For most plates tested, failure occurred for stress levels substantially below the maximum recommended tensile stress. Failure seemed to originate either at the center of the ceramic, or at the corners at the location of the copper electrode connecting the power supply to the actuator electrode bonded to the plate. Several factors responsible for early failure are listed below:

- Critical stresses at which failure occurs are very dependent on the actual transducer design and fabrication as demonstrated by the wide spread in critical stress data obtained from manufacturer literature. Failure stresses given by manufacturers are usually measured in pure compression or tension in a controlled environment. In a practical application, critical stresses depend on many factors such as: stress direction compared to poling axis, static or dynamic operation, and electrical field. Since the stress field in actuators bonded to plate radiators differs substantially from the stress field for which data are available, the level at which failure will occur is very difficult to predict from existing data.
- Defects in the bonding layer lead to local regions with high stress concentrations which can lead to early failure. Some of these defects are due to bubbles formed in the epoxy due to outgassing, residual stresses due to shrinkage of the glue during the curing process, variations in bond thickness due to uneven pressure applied during the curing process, and variations in bond thickness due to the copper electrode connecting the power supply to the actuator electrode bonded to the plate. These problems were magnified by the large size of the actuator which prevented excess glue from flowing freely out the sides of the actuator, resulting in thickness variations in the bond. Much effort was devoted to improving the bonding process as discussed in Appendices A and B. Outgassing and shrinkage of the epoxy were minimized by curing the plates at room temperature without a vacuum pad and using a different epoxy material (see Appendix B). The thickness of the copper electrode was reduced from 0.076 mm in the early tests to 0.025 mm in the later ones..
- There is a singularity in the stress field for sharp corners such as the corners of the actuator. This singularity is indicative of a very high stress concentration at that location. Indeed, failure in all samples tested originated either at the center or at the corners of the piezoceramic actuator.
- Nonlinearities and variations in the actuator mechanical properties with electric field can lead to early failure at high voltage levels.

The work presented in this report clearly shows that preventing the stress failure of piezoceramic actuators is one of the main areas where work must be continued. As discussed further in the concluding Chapter, there are several measures that can be taken which will greatly reduce this problem:

- Further improve the bonding technique.

- Locate the actuators in reduced-stress high-coupling areas.
- Round the corners of the actuators.
- Use a piezoceramic material with a higher critical stress value.
- Use segmented actuators in combination with stress-release grooves in the plate structure so that most of the bending occurs in the plate and actuator stresses are minimized.
- Reduce the size of the actuator and use a segmented actuator approach. This will help alleviate some of the problem mentioned above.

3.10. Fatigue Life of Aluminum/Piezoceramic Acoustic Plate Radiators

Of interest here is the fatigue life of an aluminum plate radiator for aircraft engine application.

Fatigue failure occurs when a structure is subjected to a repetitive or fluctuating stress field. Such failure occurs at a stress level much lower than that required to cause fracture on a single application of load. The basic factors which are necessary to cause fatigue failure are:

- A maximum tensile stress of sufficiently high value.
- Large enough variations or fluctuations in applied stress.
- A sufficiently large number of cycles of applied stress.

In addition, there are a host of other variables such as stress concentration, corrosion, temperature, overload, metallurgical structure, and residual stresses, which tend to alter the conditions of fatigue.

Boyer [45] presents a variety of S-N curves (S denotes the subjected stress level, and N denotes the number of cycles to failure) to estimate the fatigue life of various metals. Since the plate radiator is subjected to repeated bending stresses, it is sufficient to consider the fatigue life of the radiator subjected to bending stresses with a zero mean stress. The S-N curve appropriate for such an application given in [45] is shown in Figure 3.39.

The maximum bending stress for the $90 \times 90 \times 1.52$ mm plate radiator configuration considered previously is $1.36 \cdot 10^7$ N/m² for an actuator voltage of 200 Volts.

From Figure 3.39, it is clear that below $20 \cdot 10^3$ psi ($1.38 \cdot 10^8$ N/m²), aluminum alloys do not exhibit fatigue failure and have an infinite fatigue life. Since maximum stresses in the aluminum plate radiator are about 10 times below this threshold, the plate should not be prone to fatigue failure.

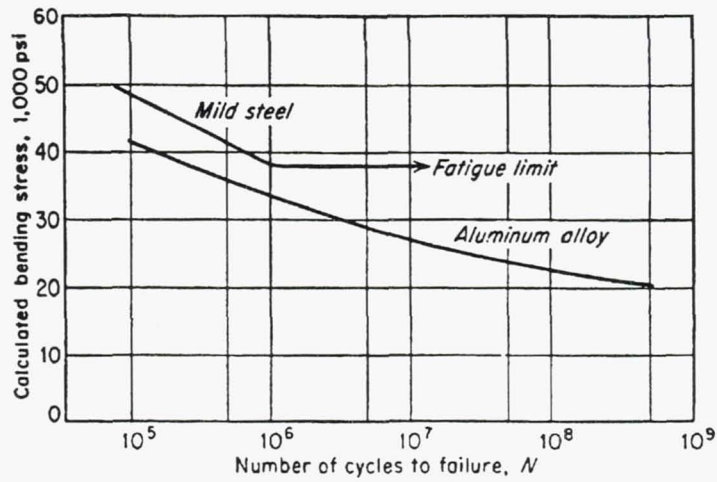


Figure 3.39. S-N curve for bending stresses with zero mean stress (from Boyer [45]).

There are other issues however which need to be addressed in future work such as the fatigue life of the actuator and of the bonding layer. Since only very limited data is available on piezoceramics and bonding layers, it was not possible at this early stage of development to obtain reliable estimates for the fatigue life of the bonding layer and of the actuator.

4. Adaptive Tuning for Acoustic Plate Radiators

Adaptive tuning methods were investigated as a way to increase the bandwidth of acoustic plate radiators. Adaptive tuning is defined as the action of changing the resonance frequency of the first plate mode. Since the transducers studied in this report are low-damping resonant devices, their frequency range is limited. In addition, slight differences in resonance frequency are always present even between identical actuators. As a result, since several plate radiators would be used in an aircraft engine, tuning of each radiator is required so that they all have the same resonance frequency. In addition, adaptive tuning will be required if the actuator is to track engine RPM over a wide frequency range.

Adaptive or variable tuning can be achieved by changing one or more of the mechanical parameters that affect resonance frequency for plate radiators, such as boundary conditions or stress distribution. Several potential methods are identified below, including passive, active, and semi-active methods with various degrees of complexity. The most promising method in terms of performance and ease of implementation was chosen and tested.

4.1. Wide-Bandwidth Source Through Damping Control

The simplest "passive" way to increase the bandwidth of an acoustic plate radiator is to increase its damping. However, increasing damping reduces the transducer power output at resonance proportionally. From the results presented in Chapter 3, it is clear that with the present state of the art, increasing damping would result in plate displacement magnitudes well below the levels required for a large aircraft engine application.

The trade-off between bandwidth and power output at resonance is best illustrated by looking at the definition of the 3-dB and 10-dB bandwidth for a single decoupled plate mode:

$$\begin{aligned} H(\omega_0 + \Delta\omega_{3dB}) &= \frac{H(\omega_0)}{\sqrt{2}} \\ H(\omega_0 + \Delta\omega_{10dB}) &= \frac{H(\omega_0)}{\sqrt{10}} \end{aligned} \quad (4.1)$$

where $H(\omega)$ is the plate response at frequency ω , $\Delta\omega_{3dB}$ and $\Delta\omega_{10dB}$ are the 3-dB and 10-dB bandwidths, and ω_0 is the resonance frequency. For a single-degree of freedom system and for low damping ($(\Delta\omega_{3dB}/\omega_0) \ll 1$ and $(\Delta\omega_{10dB}/\omega_0) \ll 1$), the 3-dB and 10-dB bandwidths, and the response at resonance are given by:

$$\begin{aligned} \Delta\omega_{3dB} &= 2 \zeta \omega_0 \\ \Delta\omega_{10dB} &= 6 \zeta \omega_0 \end{aligned} \quad (4.2)$$

$$|H(\omega_0)| = \frac{A}{2\zeta\omega_0^2} \quad (4.3)$$

where ζ is the damping ratio.

Figures 4.1 and 4.2 show the phase and normalized amplitude response for a plate resonating at 2 KHz for two damping ratios.

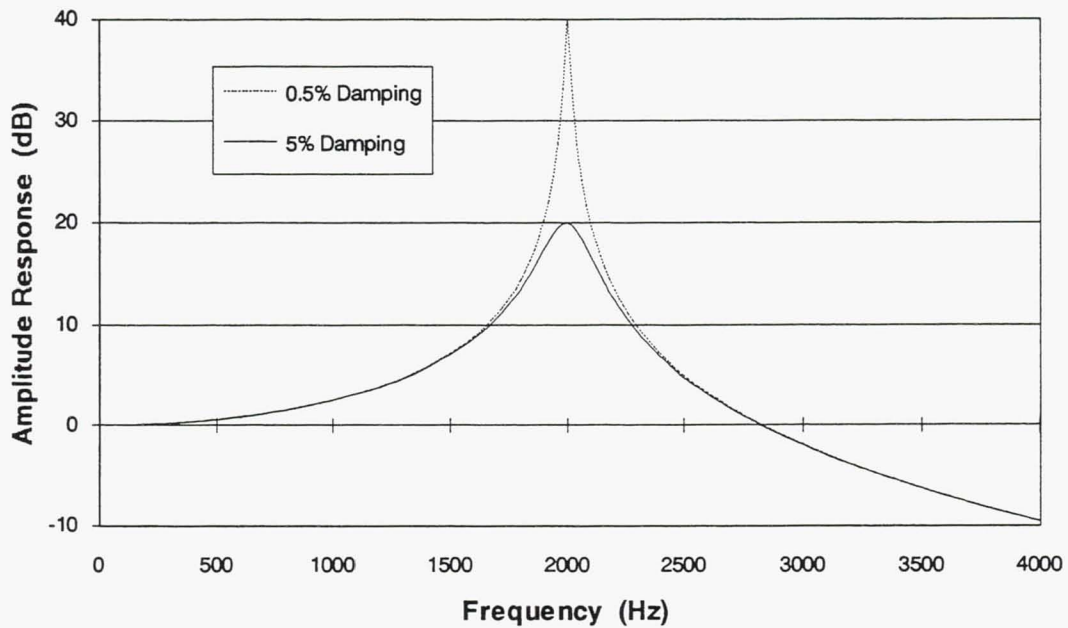


Figure 4.1. Amplitude response for damping ratios of 0.5 % and 5 %.

Table 4.1 lists bandwidths and normalized response for the two cases shown in Figures 4.1 as well as for damping ratios of $\zeta = 1$, and 2.

ζ	$\Delta\omega_{3dB}$ (Hz)	$\Delta\omega_{10dB}$ (Hz)	$\frac{2\omega_0^2 H(\omega_0) }{A}$	$\frac{2\omega_0^2 H(\omega_0) }{A}$ (dB)
0.5	20	60	1	0
1	40	120	0.5	-6
2	80	240	0.25	-12
5	200	600	0.1	-20

Table 4.1. 3-dB and 10-dB bandwidths, and normalized response for plate radiator versus damping ratio.

The 10-dB bandwidth can be increased by a factor 10 from 60 Hz to 600 Hz by going from a lightly damped ($\zeta = 0.5$) to a heavily damped ($\zeta = 5$) plate. However, the response of the highly damped plate is also lower by 20 dB. On the other hand, the higher slope for the phase at low damping ratios around resonance stiffens the requirements for the controller used to calculate the noise canceling signal since an accurate knowledge of the transducer phase response is required for effective cancellation.

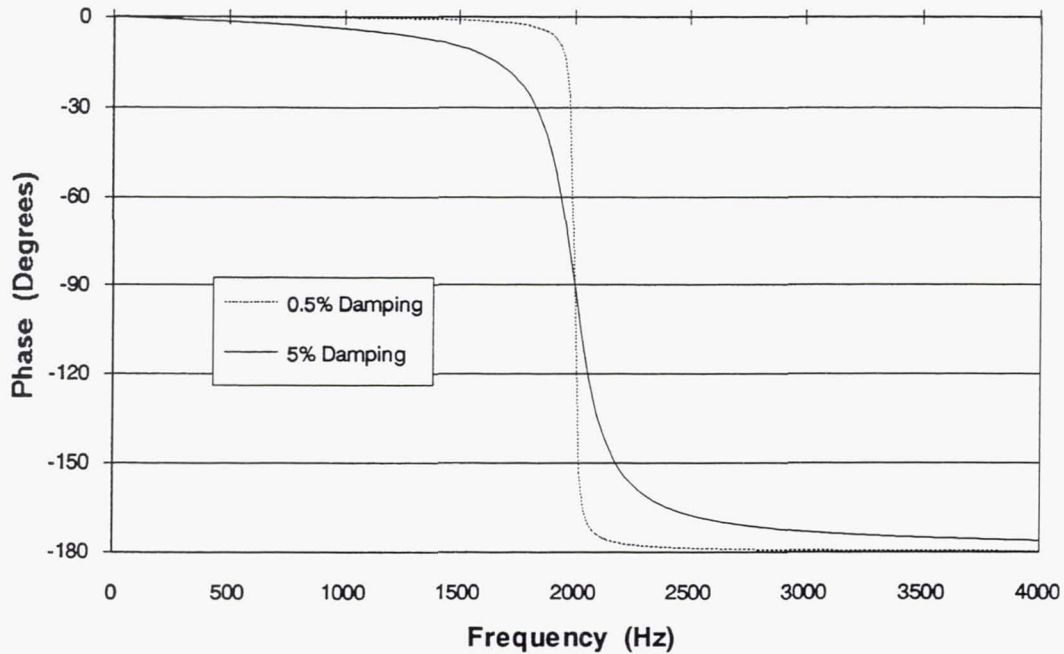


Figure 4.2. Phase response for damping ratios of 0.5 % and 5 %.

4.2. Adaptive Tuning Using Linear or Bending Stiffness Control

In this approach, the resonance frequency of the plate is controlled by changing the linear or bending stiffness of its boundaries through linear or torsional springs.

4.2.1. Analysis

In order to evaluate this approach, an analysis was performed using a simply supported beam with linear or torsional springs attached at a variable distance from each beam support. The beam is shown in Figure 4.3 for the case of a linear spring attached at a distance x_0 from the beam support. Due to symmetry, only half the problem is considered.

The beam end at $x = 0$ is simply supported and hence has displacement and moment boundary conditions equal to zero:

$$u = EI \frac{\partial^2 u}{\partial x^2} = 0 \quad (4.4)$$

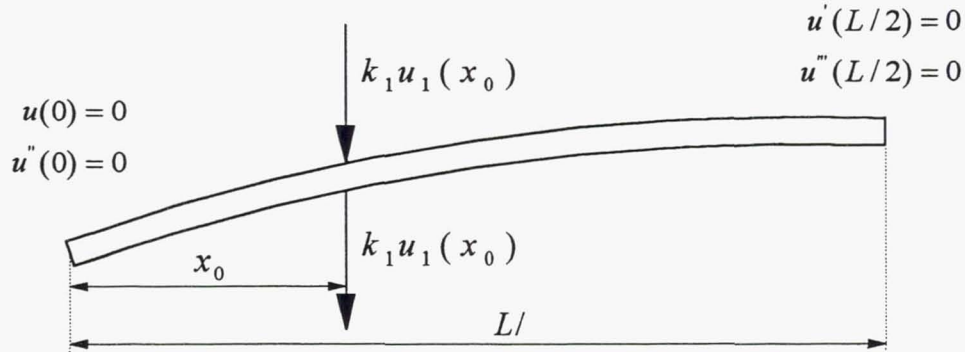


Figure 4.3. Free-body diagram of a simply supported half-beam with linear springs.

The midpoint of the beam a $x = L/2$ has slope and shear force equal to zero:

$$\frac{\partial u}{\partial x} = EI \frac{\partial^3 u}{\partial x^3} = 0 \quad (4.5)$$

The half-beam is compartmentalized into two regions: $0 < x < x_0$, and $x_0 < x < L/2$. The compatibility conditions at $x = x_0$ are:

$$\begin{aligned} u_1 &= u_2 \\ \frac{\partial u_1}{\partial x} &= \frac{\partial u_2}{\partial x} \\ EI \frac{\partial^2 u_1}{\partial x^2} &= EI \frac{\partial^2 u_2}{\partial x^2} \\ EI \frac{\partial^3 u_1}{\partial x^3} &= EI \frac{\partial^3 u_2}{\partial x^3} + 2k_1 u_1(x_0) \end{aligned} \quad (4.6)$$

Where subscripts $_1$ and $_2$ denote the regions $0 < x < x_0$ and $x_0 < x < L/2$ respectively, and k_1 denotes the linear spring stiffness.

The displacement profile in each region ($i = 1$ or 2) takes the form:

$$u_i = c_{1i} \cos \lambda x + c_{2i} \sin \lambda x + c_{3i} \cosh \lambda x + c_{4i} \sinh \lambda x \quad (4.7)$$

where $\lambda = (\omega^2 m / EI)$. Here, ω is the natural frequency of interest, m is the mass per unit length, E is the Young's modulus, and I is the moment of inertia of the beam. The eight undetermined coefficients in Equation 4.7 can be solved by making use of the eight boundary conditions (Equations 4.4 to 4.6). The resulting matrix equation is of the form:

$$[A]\{C\} = 0 \quad (4.8)$$

$\{C\}$ is an 8×1 vector containing the undetermined coefficients from Equation 4.7 and $[A]$ is an 8×8 coefficient matrix consisting of hyperbolic and trigonometric functions. For a non-trivial solution the determinant of $[A]$ is equal to zero which leads to an equation of the form:

$$f(\omega) = 0 \quad (4.9)$$

Solving the above expression for ω yields the resonance frequencies of the system. This was done numerically using the Newton-Raphson method for both the linear and torsional spring cases.

The analysis for the case of torsional springs, is identical except for the compatibility conditions at $x = x_0$ which takes the following form:

$$\begin{aligned} u_1 &= u_2 \\ \frac{\partial u_1}{\partial x} &= \frac{\partial u_2}{\partial x} \\ EI \frac{\partial^2 u_1}{\partial x^2} &= EI \frac{\partial^2 u_2}{\partial x^2} + k_2 \frac{\partial u_1}{\partial x} \Big|_{x=x_0} \\ EI \frac{\partial^3 u_1}{\partial x^3} &= EI \frac{\partial^3 u_2}{\partial x^3} \end{aligned} \quad (4.10)$$

Where k_2 denotes the torsional stiffness.

4.2.2. Results

The effect of linear stiffness control on the resonance frequency of the first mode of a simply supported beam is illustrated in Figure 4.4. Nine curves are shown for values of x/L varying from 5 % to 0.45 %. In every case, the beam resonance frequency increases as stiffness increases. However, the increase is also larger as the springs are attached closer to the center of the beam. Therefore, this approach is not practical since attaching stiff springs close to the center of the beam limits the equivalent piston displacement for the first mode by effectively grounding the beam center. Attaching the springs close to the beam boundaries maximizes the equivalent piston displacement but minimizes the effect of the springs as shown by the $x/L = 5\%$ curve.

Adaptive tuning using a torsional spring is a much more effective approach to control the first mode resonance frequency. Using this method, the boundary conditions are changed from those of a simply supported plate with no rotational restraint (zero bending stiffness), to those of a clamped plate with no rotation at the boundary (infinite bending stiffness).

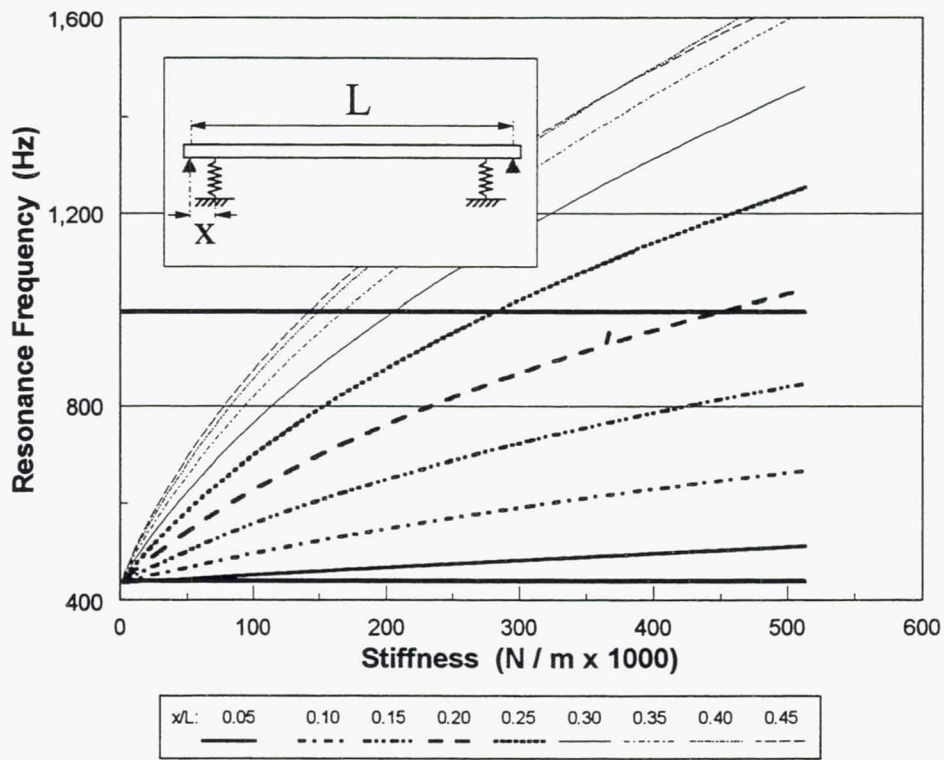


Figure 4.4. First mode resonance frequency versus linear spring stiffness.

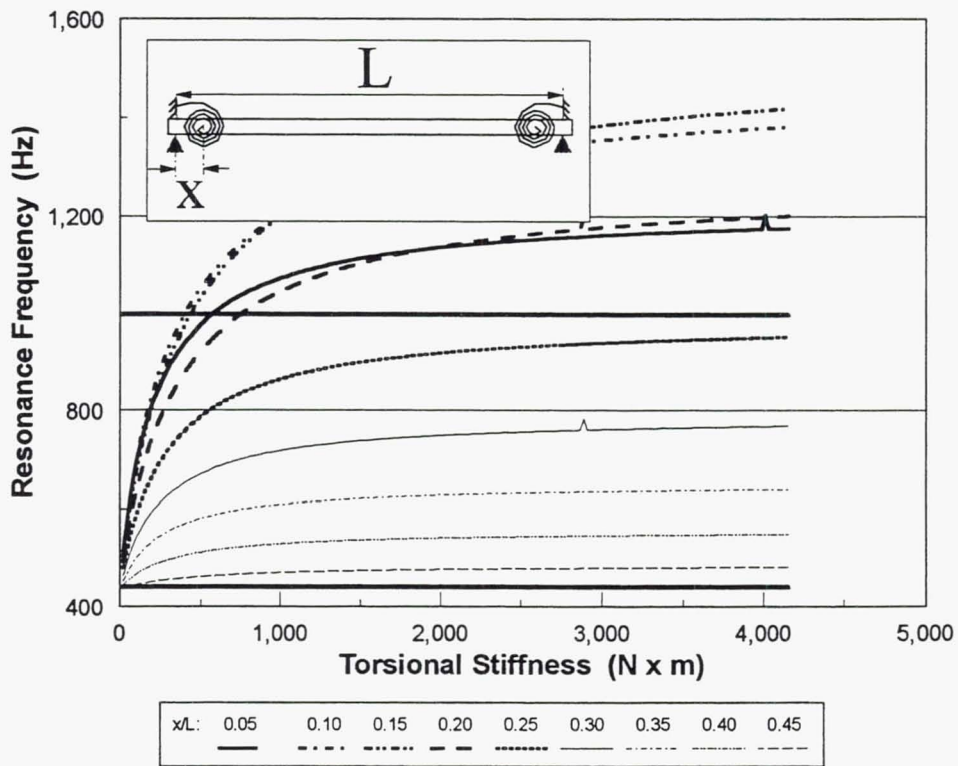


Figure 4.5. First mode resonance frequency versus torsional spring stiffness.

The effect of bending stiffness control on the resonance frequency of the first mode of a simply supported beam is illustrated in Figure 4.5. Nine curves are shown for values of x/L varying from 5 % to 0.45 %. In every case, the beam resonance frequency increases as the bending stiffness increases. The maximum frequency variation (bandwidth) as a function of spring location is very different from the linear spring case and is shown in Figure 4.6.

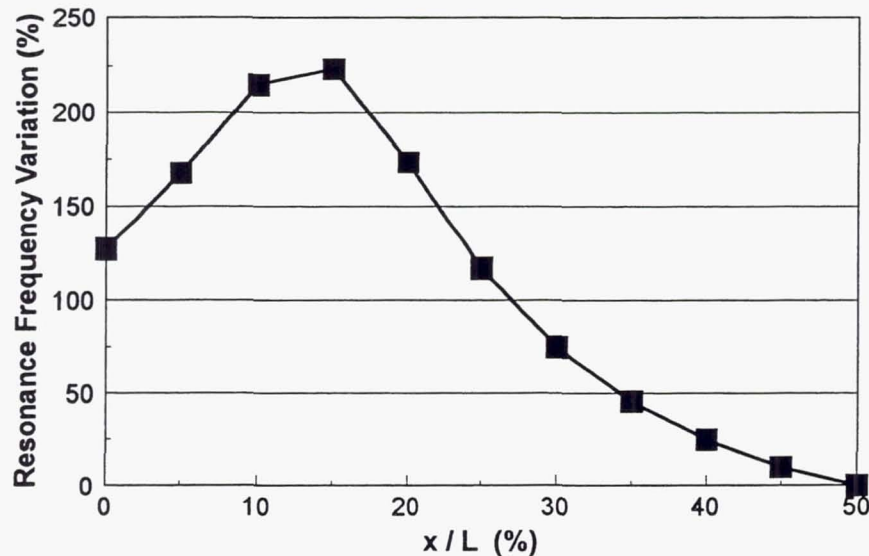


Figure 4.6. Maximum variation of the first mode resonance frequency versus torsional spring location.

For a spring located at the boundary, the frequency variation is bounded by the simply-supported and the clamped cases. As the attachment location moves towards the center of the beam, the maximum frequency variation increases and peaks around $x/L = 15$ %. It then decreases to zero when both springs are attached at the center of the beam where the beam slope is zero for the first mode.

A large variation in the resonance frequency is possible with this approach. The high slope of the resonance frequency curve at low values of the torsional stiffnesses, implies that large variations in resonance frequency can be obtained for relatively modest changes in the torsional stiffness. This assumes that a "good" simply supported boundary condition can be implemented and that no shear forces are applied by the torsional spring, which might be difficult to implement in practice.

4.2.3. Implementation

Figures 4.7 and 4.8 show two possible designs for adaptive tuning through linear or bending stiffness control.

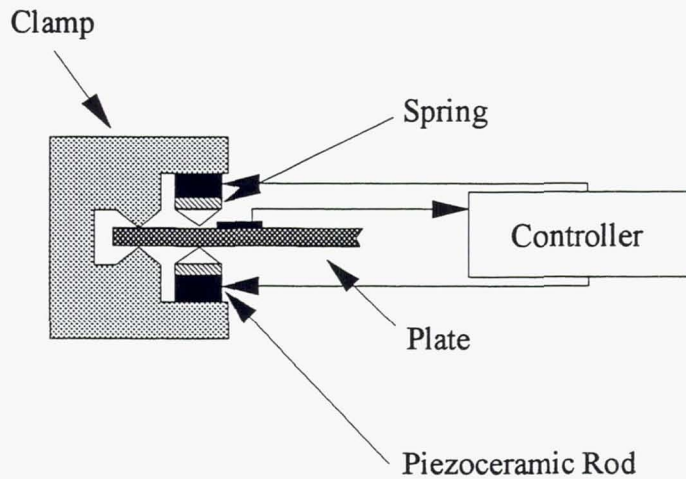


Figure 4.7. Adaptive tuning using linear stiffness control.

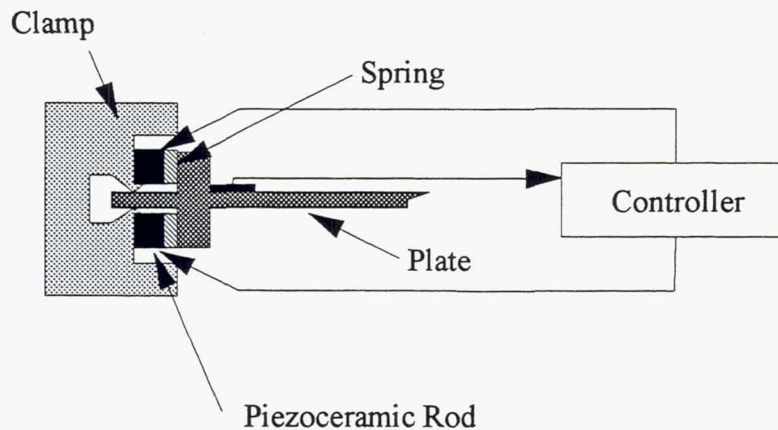


Figure 4.8. Adaptive tuning using bending stiffness control.

With both methods, stiffness members with variable overall stiffnesses are attached to the plate clamp assembly so as to exert a variable force or a moment on the plate. The members consist of a spring element with a fixed stiffness and a rigid "displacement actuator". The plate displacement is sensed and fed back to the stiffness member which generates a force or moment which replicates the action of a linear or torsional spring having a specific stiffness. The stiffness of the members is controlled by the gain of the feedback loop.

The principle of operation is best illustrated with the following simplified analysis where the finite stiffness of the displacement actuator element has been ignored.

The static equilibrium conditions for the beam shown in Figure 4.9 is:

$$F_t = F_b = k(x - x_0) \quad (4.11)$$

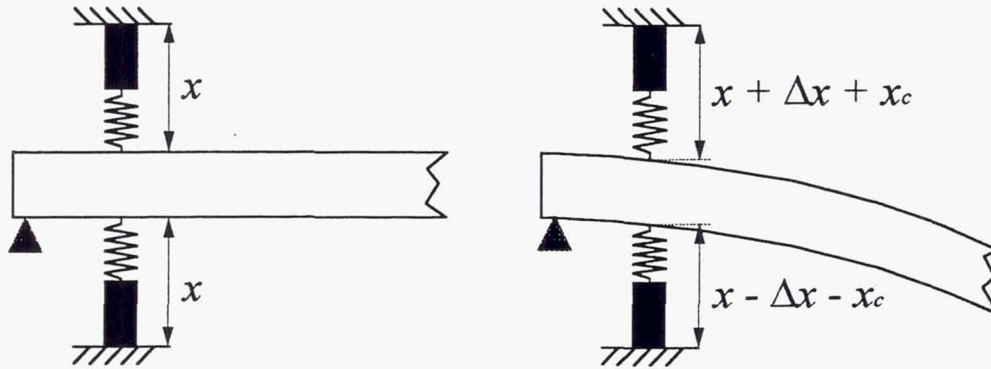


Figure 4.9. Adaptive tuning using linear stiffness control

where F_t and F_b are the forces exerted on the beam by the top and bottom members, k is the spring stiffness, x is length of each pre-compressed stiffness member, and x_0 is the length of a stiffness member with no load applied.

From the dynamic equilibrium condition, we have:

$$\begin{aligned} F_t &= k(x - x_0 + \Delta x + x_c) \\ F_b &= k(x - x_0 - \Delta x - x_c) \end{aligned} \quad (4.12)$$

where Δx is the beam displacement and x_c is the change in length of the PZT actuator which is part of the stiffness member. Therefore, the net force on the beam is given by:

$$\Delta F = F_t - F_b = 2k(\Delta x + x_c) \quad (4.13)$$

If the plate displacement is fed back to the actuator through the controller such that $x_c = G \Delta x$, the net force on the beam is:

$$\Delta F = 2k(1 + G) \Delta x \quad (4.14)$$

Hence, the controller feedback gain G controls the stiffness of the linear spring member.

Since the actuator motion x_c is proportional to the beam displacement Δx , the system must operate in an AC mode. To simplify implementation, the driving signal to the plate can be used to drive the displacement actuator rather than the output signal from a plate displacement sensor. In addition, plate acceleration can be used instead of displacement in order to vary the first mode resonance frequency through inertial rather than stiffness control.

In order to complete the design, the maximum feedback gain and actuator displacement must be determined.

The combined stiffness of the member is minimum and equal to zero for $G = -1$. The maximum combined stiffness K_{\max} required to obtain a specific bandwidth can be obtained from Figure 4.4. The resulting maximum value for the gain G_{\max} is given by:

$$G_{\max} = \frac{K_{\max}}{k} - 1 \quad (4.15)$$

Therefore, the maximum force F_{\max} required by the actuator is:

$$F_{\max} = kG_{\max} \Delta x_a \quad (4.16)$$

Where Δx_a is the beam displacement amplitude at the spring attachment point. The maximum displacement amplitude $x_{c \max}$ for the actuator is given by:

$$x_{c \max} = G_{\max} \Delta x_a \quad (4.17)$$

This analysis also applies to the bending stiffness control approach using torsional springs. The maximum combined torsional stiffness $K_{R \max}$ required to obtain a specific bandwidth can be obtained from Figure 4.5. The maximum gain $G_{R \max}$ is then given by:

$$G_{R \max} = \frac{K_{R \max}}{k d^2} - 1 \quad (4.18)$$

Where d is the distance between the application point of the forces and the beam centerline. The maximum force $F_{R \max}$ and maximum displacement amplitude $x_{c \max}$ for the actuator are given by:

$$F_{R \max} = kG_{R \max} d \Delta \theta_a \quad (4.19)$$

and

$$x_{Rc \max} = G_{R \max} d \Delta \theta_a \quad (4.20)$$

Where $\Delta \theta_a$ is the beam rotation amplitude at the attachment point of the moment arm.

F_{\max} , $x_{c \max}$, $F_{R \max}$, and $x_{Rc \max}$ specify the actuator properties required in each case. For a complete analysis including an estimate of actuator force and displacement requirements, the beam amplitude Δx_a or rotation $\Delta \theta_a$ at the spring attachment point must be known. These values can be derived from the beam mode shapes and can be obtained in a straightforward fashion by expanding the resonance frequency analysis in Section 4.2.1 following an approach similar to the one used to calculate the beam response due to bonded PZT actuators (Section 2.2.1).

Due to time constraints and since another adaptive tuning concept simpler to implement was chosen for testing (tuning using back chamber pressurization), no further work was performed on the bending stiffness control approach. Additional work should be carried out to estimate absolute actuator force and displacement requirements for a practical design.

Adaptive tuning using bending stiffness control looks promising if it can be implemented effectively. It does not impose a DC stress field on the plate and the actuator, and therefore does not limit the dynamic range of the source. However, disadvantages of this approach are that it requires an AC feedback control system, a "good" simply-supported boundary condition (to minimize $G_{R_{max}}$), and accurate control of the boundary condition around the entire plate.

4.3. Adaptive Tuning Using Variable In-Plane Frame Loading

Axial loading can be used to control the resonance frequency. An in-plane tensile load applied to a plate increases its resonance frequency, while a compressional load decreases it.

Figure 4.10 shows a typical implementation for a rectangular noise radiating panel. The panel is clamped in a frame at each corner such that there is no slippage between the frame and the panel. An open loop controller turns a "desired frequency" signal into a DC position signal sent to the actuators which expand and contract the frame, thus changing the tensile and compressive in-plane loading on the plate. The plate displacement can be sensed and fed back to the controller to monitor the plate response and ensure that the plate resonance frequency is as required. On-line system identification techniques using low-level "dithering" broadband signals can be used for this purpose.

One of the main advantages of this method compared with the linear or bending stiffness control approach is that it only requires a DC controller, thus simplifying the system. However, it still requires actuators to be mounted in the frame of each plate radiator. In addition, stretching of the plate also induces stresses in the actuators bonded to the plate which limits the dynamic range of the system.

The principle of operation is further illustrated by the following simple analysis.

An approximate closed form solution for the natural frequencies of a rectangular plate is given by [35]

$$f_{ij} = \frac{\pi}{2} \left[\frac{G_1^4}{a^4} + \frac{G_2^4}{b^4} + \frac{2J_1J_2 + 2\nu(H_1H_2 - J_1J_2)}{a^2b^2} \right]^{1/2} \left[\frac{Eh^2}{12\rho(1-\nu^2)} \right]^{1/2} \quad (4.21)$$

where, $i = 1, 2, 3, \dots$, $j = 1, 2, 3, \dots$, and the indices $_1$ and $_2$ relate to the sides of width a and b respectively. G , H , and J are given in Table 4.2 as a function of the mode index (indices i and j) for simply-supported and clamped boundary conditions.

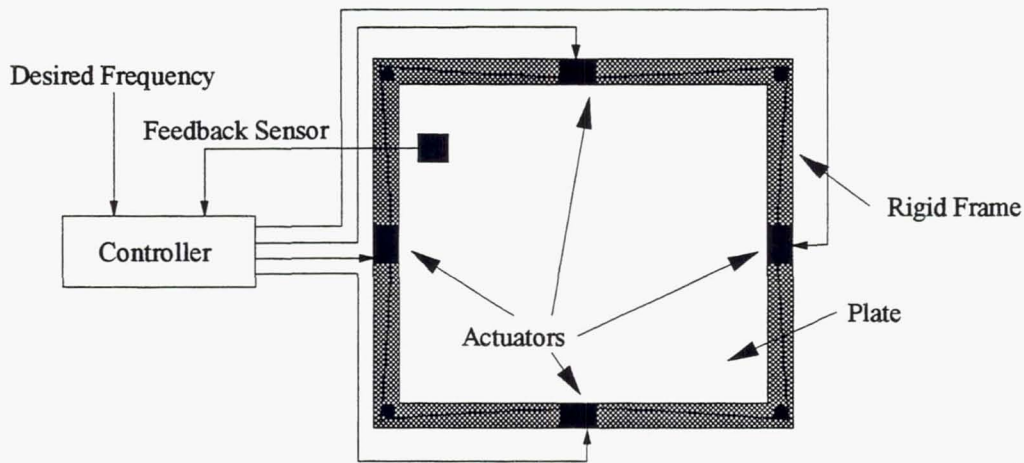


Figure 4.10. Adaptive tuning using in-plane plate loading.

Boundary Conditions on Opposite Edges	Mode Index (n)	G	H	J
2. Simply Supported-Simply Supported	1	1	1	J = H
	2	2	4	
	3	3	9	
	n	n	n ²	
3. Clamped-Clamped	1	1.506	1.248	J = H
	2	2.5	4.658	
	3	3.5	10.02	
	n (n > 1)	$\left(n + \frac{1}{2}\right)$	$\left(n + \frac{1}{2}\right)^2 \left[1 - \frac{2}{\left(n + \frac{1}{2}\right)\pi}\right]$	

Table 4.2. G, H, and J coefficients for simply-supported and clamped plates.

Adding normal in-plane loads to the plate, the natural frequencies $f_{ij}|_{\text{in-plane load}}$ can be approximated as [32]:

$$f_{ij}|_{\text{in-plane loads}} = \left(f_{ij}^2|_{\text{no loads}} + \frac{N_1 J_1}{4\rho h a^2} + \frac{N_2 J_2}{4\rho h b^2} \right)^{1/2} \quad (4.22)$$

where N_1 and N_2 are the in-plane loads per unit length, and ρ and h are the plate density and thickness.

For a square plate loaded equally on each side, the buckling load N_b is given by:

$$N_b = -f_{ij}^2|_{\text{no loads}} \times \frac{2\rho ha^2}{J} \quad (4.23)$$

For large compressional loads ($N \approx -|N_b|$), the first mode resonance frequency goes to zero. In addition, it is clear from Figure 4.11 that the largest variation in natural frequency is for the first mode, which is the best acoustic radiator.

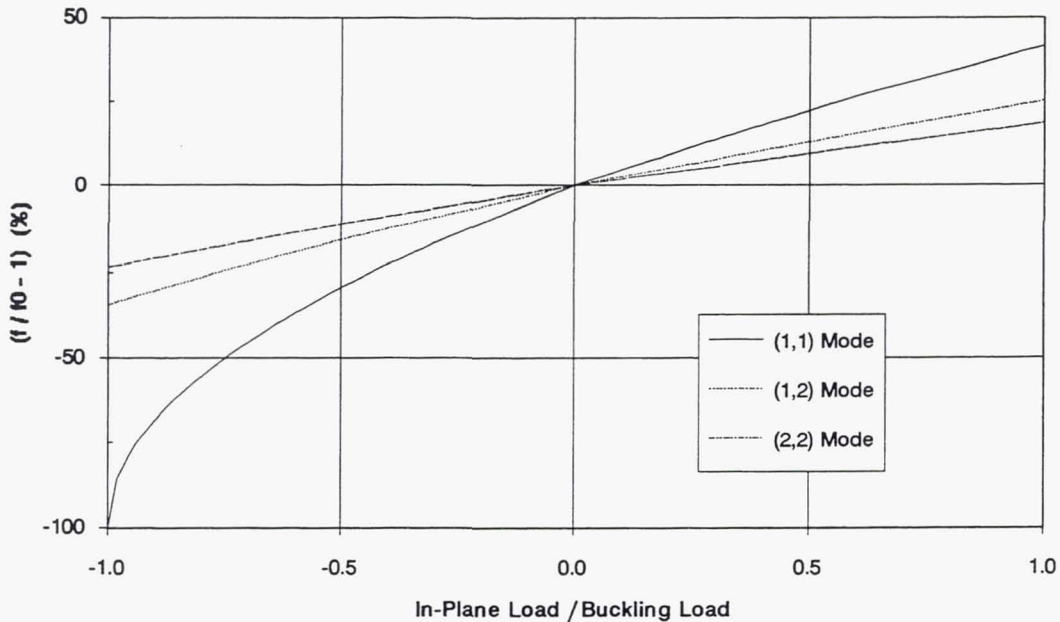


Figure 4.11. Plate resonance frequencies versus in-plane load.

The buckling forces for 90×90 mm aluminum beams are listed in Table 4.3 as a function of beam thickness:

Beam Thickness (mm)	Buckling Load (N)
0.76	1,694
1.52	13,552

Table 4.3. Beam buckling load versus beam thickness - Aluminum.

A corresponding force/displacement diagram is shown in Figure 4.12 for plates with thicknesses ranging from 0.76 mm to 1.52 mm. Data points are for tensile or compressive forces equal to half the buckling load of each plate, corresponding to variations in the resonance frequency of -29 % to 22 %.

Figure 4.12 shows that relatively modest forces and displacements are necessary for the thinner plates, while much higher displacements and forces are required for the thicker plates. Also plotted are the force/displacements capabilities for a typical piezoelectric or electrostrictive multilayer actuators (rough dimensions $10 \times 10 \times 20$ mm). Four actuator combinations are shown: One single actuator in each frame member, a 2×2 combination of two actuators in parallel each consisting of two actuators in series, and 3×3 and 4×4 combinations.

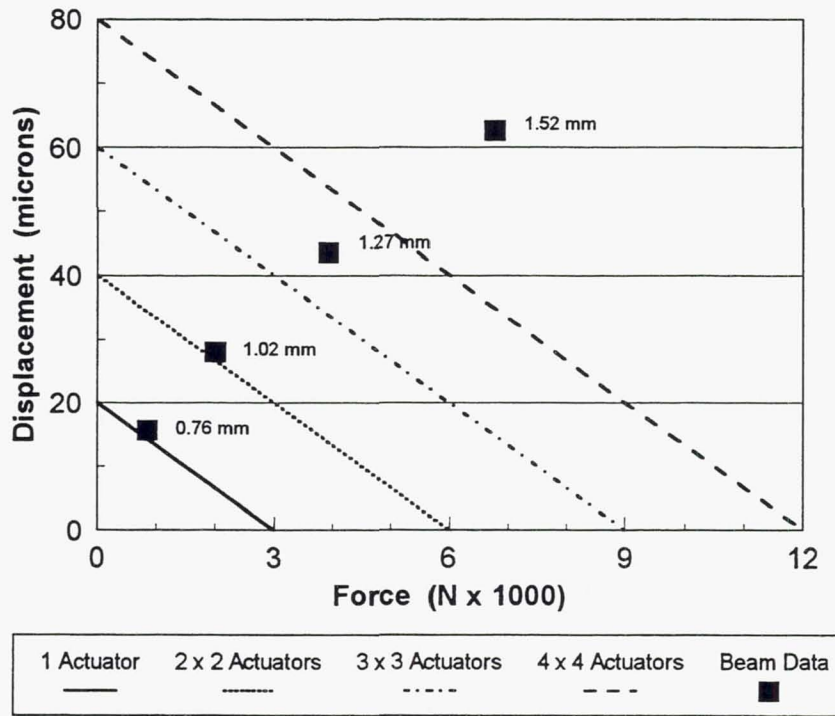


Figure 4.12. Force/Displacement diagram for aluminum plates of varying thicknesses.

Stresses in the piezoceramic actuator bonded to the plate must also be lower than the critical stresses for the actuator material. For the case described above, the stress σ_c in the ceramic can be approximated by:

$$\sigma_c = E_c \varepsilon \quad (4.24)$$

where E_c is the Young's modulus for the ceramic. The strain ε is given by:

$$\varepsilon = \frac{(N_b a / 2) / A}{E_{Al}} \quad (4.25)$$

where $(N_b a / 2)$ is the in-plane load, A is the plate cross sectional area, and E_{Al} is the Young's modulus for aluminum. Stresses in thin and thick beams are given in Table 4.4.

Beam Thickness (mm)	Stresses in Actuator (N / m ²)
0.76	$1.24 \cdot 10^7$
1.52	$4.95 \cdot 10^7$

Table 4.4. Stresses in piezoceramic actuator versus beam thickness - Aluminum.

The stresses in the actuator induced by the axial loading are below and above the typical maximum allowable tensile stresses for the thinner and the thicker plates respectively. However, for both plates, actuator stresses are well below the maximum allowable compressive stresses. As a result, adaptive tuning using in-plane plate loading might be best implemented using a pre-stressed system. This also has the advantage of increasing the bandwidth of the system as the rate of change in resonance frequency as a function of in-plane load is higher for compressive loads than for tensile loads (see Figure 4.11).

4.4. Adaptive Tuning Using Variable Embedded In-Plane Loading

Another technique based on the same principle as variable in-plane frame loading is shown in Figure 4.13 and is inspired from the techniques used to detune rotating blades such as circular saws.

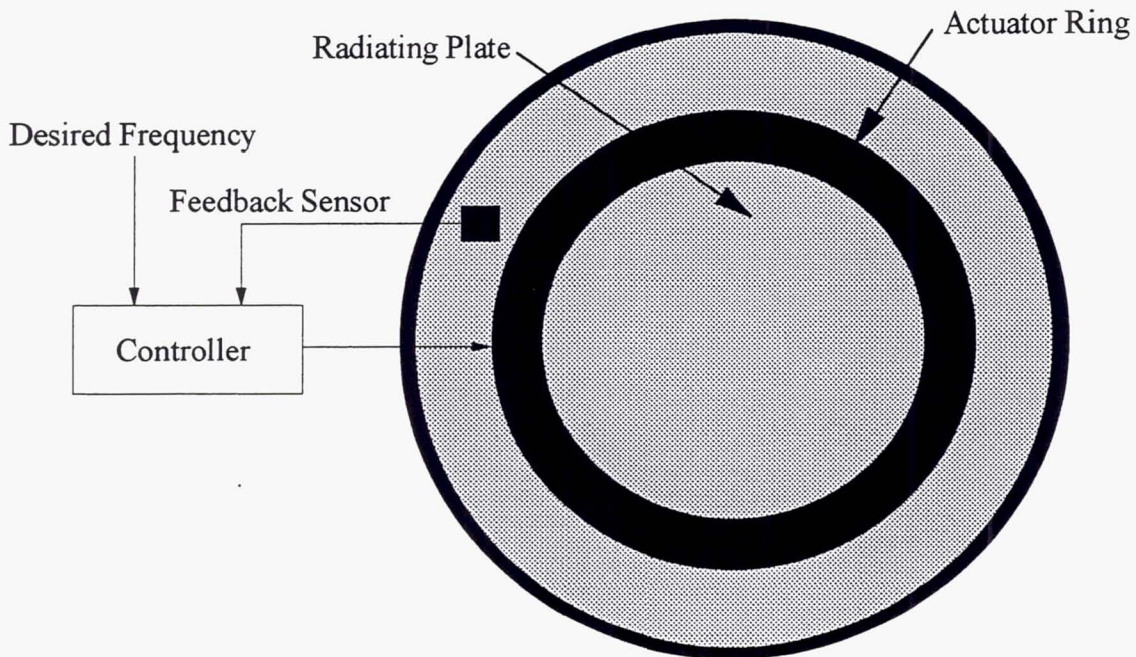


Figure 4.13. Adaptive tuning using in-plane plate loading.

A thin annular actuator ring induces both compression and tension in a circular plate or membrane. The actuator ring can be embedded between two layers comprising the plate or bonded on both sides of the plate at about half the total radius of the plate. Extension and compression of the ring induces compressive and tensile stresses which change the natural frequencies of the plate. This arrangement has the advantage that the stiffness of the plate is equal to the stiffness of the PZT support structure. Hence there is no stiffness mismatch between the frame and the plate.

A quick experiment was performed using a $90 \times 90 \times 1.52$ mm aluminum plate with $66 \times 66 \times 0.51$ mm piezoceramic actuators bonded on each side of the plate. The actuators were powered by a "tuning" DC signal using a high-voltage DC/AC TREK amplifier. The polarity of the electrical field applied to each actuator was such that displacements were in the same direction. Two methods were used to identify the natural frequencies of the plate: Impulse hammer method and random excitation through a low level AC signal superimposed to the DC tuning signal. No "useful" change in resonance frequency was observed with this experimental setup, even with DC voltages of up to 60 Volts.

Using results from the previous Chapter, a quick analysis of this experiment can be performed. The maximum force developed by a typical PZT actuator such as the Motorola D3203HD used in this experiment can be approximated by the blocked force F given by:

$$F = \frac{VI}{g_{13}} \quad (4.26)$$

$$= 440 \text{ N}$$

where l is the actuator width (66 mm), V is the voltage applied to the actuator (60 Volts), and g_{13} is the transverse voltage coefficient ($-9 \cdot 10^{-3}$ Vm/N).

The 440 N force is only equal to 3 % of the buckling force for a 1.52-mm thick beam given (see Table 4.3). From Equation 4.22, this results in less than a 2.5 % increase or decrease in resonance frequency which is too small to be of practical use. Although larger increases can be obtained by optimizing the design, much larger forces must be applied to the structure for this tuning method to become effective.

4.5. Adaptive Tuning Using Back Chamber Pressurization and Volume Variation

In this approach, tuning is obtained by changing the pressure or the volume of an enclosure mounted behind the radiating plate. This in turn changes the internal stresses and curvature of the plate, which shifts its resonance frequencies. In addition, the stiffness of the combined plate/enclosure system also varies with the air pressure or the enclosure volume, which contributes to the shift in resonance frequencies.

Figure 4.14 shows a schematic of one noise source as it might be implemented in an aircraft engine. The noise source consists of a plate radiator excited by a thin sheet

piezoceramic actuator driven by an Active Noise Control (ANC) controller. The back of the plate radiates noise in an enclosed cavity with a variable pressure or volume (or both).

A tuning controller varies the back cavity pressure relative to the pressure in the front of the plate. This applies a distributed force which deforms and stretches the plate. As a result, the internal in-plane stresses in the plate and its curvature are increased, which raises its natural frequencies. In addition, increasing the pressure in the cavity increases the stiffness of the air spring formed by the back cavity volume which raises the resonance frequencies of the first mode of the system.

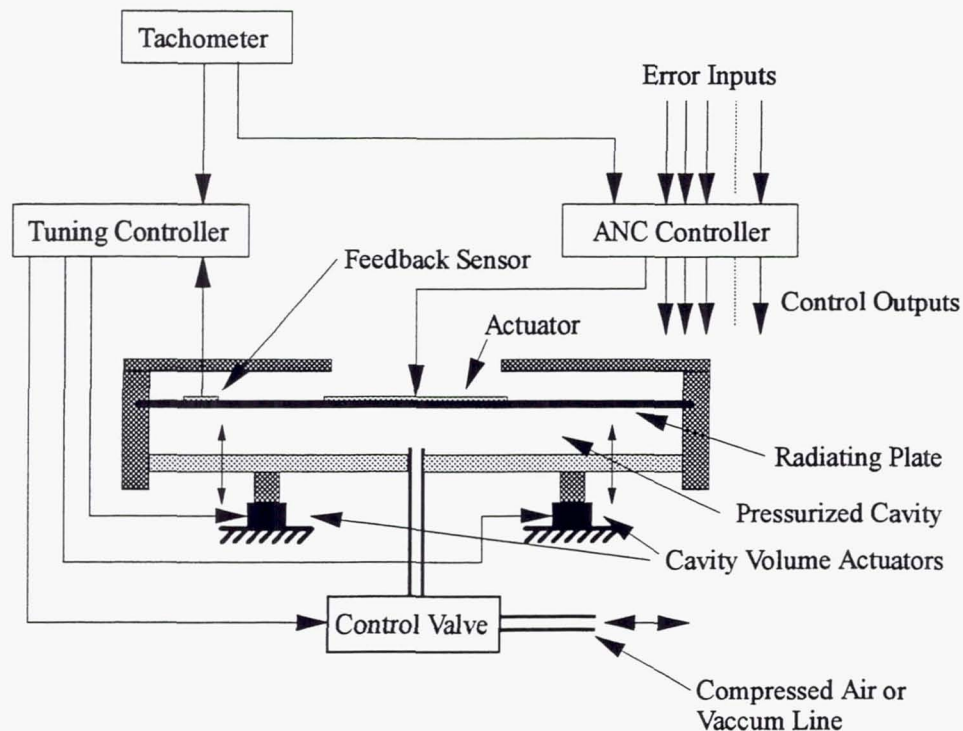


Figure 4.14. Adaptive tuning using back chamber pressurization and volume variation.

Similarly, decreasing the volume of the back cavity increases the stiffness of the air spring, therefore increasing the first mode resonance frequency. The main advantage of the volume variation approach is that the pressure on each side of the plate can be equalized. This eliminates plate stretching and deformation and extends the dynamic range of the system. Disadvantages of this approach are the limited frequency variation possible and the nonlinear behavior of the air spring when using relatively stiff panels, as discussed in the following section.

The stiffness k of the air spring is easily calculated assuming an adiabatic compression inside the back chamber [46]:

$$k = \frac{\gamma P S^2}{V} \left[\frac{1}{1 - (S/V)\Delta x} \right]^{\gamma+1} \quad (4.27)$$

where P and V are the back chamber pressure and volume with the plate at rest. γ is the ratio of specific heats, S is the plate area, and Δx is the equivalent plate piston displacement.

To be useful, the stiffness of the air spring must be comparable to the plate stiffness. For a relatively stiff aluminum plate, this means a small volume V , which in turn might result in the volume displaced by the plate ($S \Delta x$) being comparable to V . From the above expression for the spring stiffness k , this violates the condition that $S \Delta x \ll V$ which ensures spring linearity. Unwanted harmonics are generated as a result, which reduces the source effectiveness.

The tuning controller uses "desired frequency" information from a tachometer signal to determine the chamber pressure required to set the first mode resonance frequency to the proper value. A control valve connected to the controller sets the pressure in the back chamber. As mentioned earlier, a feedback sensor can be used in combination with the main radiating plate actuator to ensure that the system has the proper resonance frequency by measuring the resonance frequencies of the combined system using one of a variety of system identification techniques.

In the case of stiffness control through changes in cavity volume, the controller output is sent to an actuator which controls the position of the back wall of the cavity while the control valve is used to equalize the DC pressures on each side of the radiating plate.

Both pressure and volume variation tuning methods can be implemented together, or independently. The effectiveness of each method depends on the stiffness of the radiating plate. In the case of actuators for aircraft engines, stiff materials such as aluminum are preferable for which the pressure tuning method is usually the most effective. For less stiff materials such as Lexan, the volume tuning method is very effective.

Tests were run for both the pressure and volume variation method.

4.5.1. Adaptive Tuning Through Chamber Volume Variation

Tests were first carried out using a $127 \times 140 \times 0.76$ mm Lexan plate with no actuator and a $127 \times 140 \times 1.52$ mm Lexan plate with $66 \times 66 \times 0.25$ mm actuators bonded on each side. The low stiffness of the Lexan allows the volume variation method to be tested easily. Several back chambers were constructed with volumes as shown in Table 4.5 and Figure 4.15.

A simple mass/spring model was used to predict the resonance frequencies of the plate/back cavity combination as shown in Figure 4.16.

Chamber #	Volume ($\times 10^{-3} \text{ m}^3$)
1	0.12
2	0.36
3	1.53
4	2.95

Table 4.5. Back chamber volumes for Lexan plates experiment.

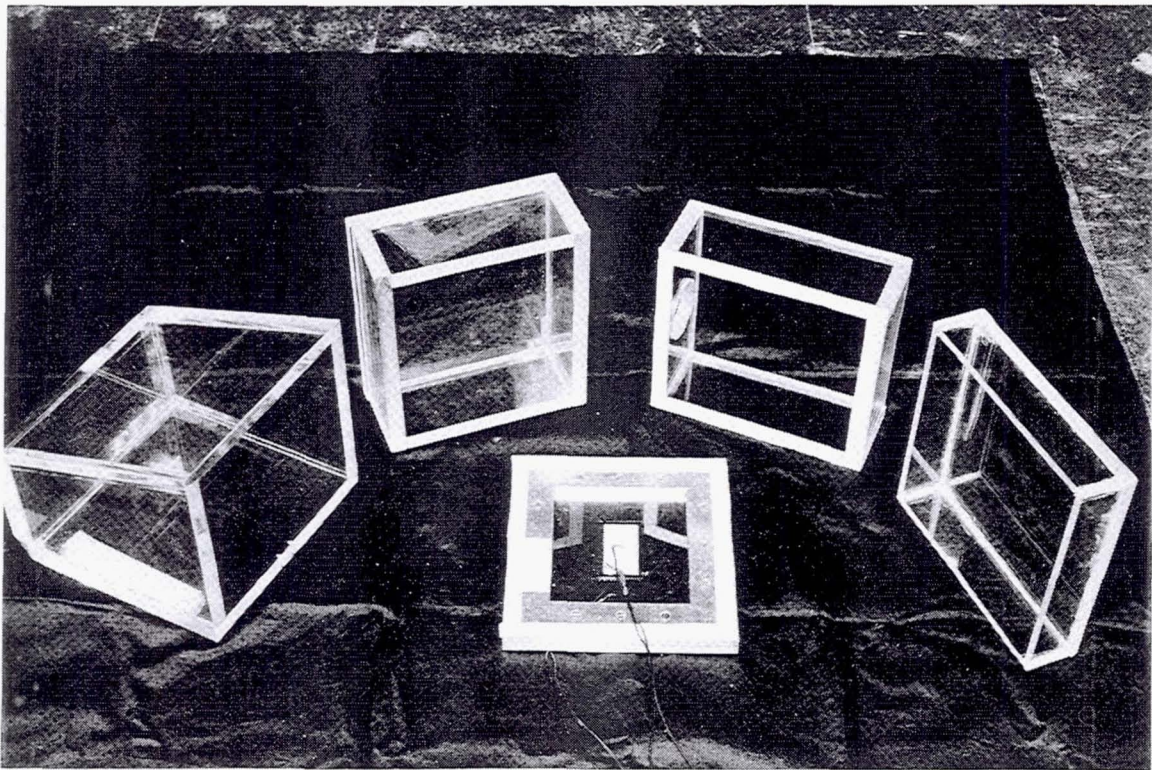


Figure 4.15. Back chambers and plate used for adaptive tuning using chamber volume variation.

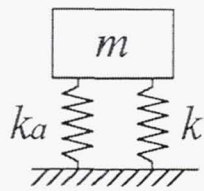


Figure 4.16. Simplified model for plate and back chamber cavity.

Where M and k are the plate modal mass and stiffness, and k_a is the stiffness of the back cavity.

The plate modal mass and stiffness used in the analytical prediction were determined experimentally by measuring the resonance frequency of the combined system for two different back cavity volumes:

$$m = \frac{k_{a2} - k_{a1}}{\omega_2^2 - \omega_1^2} \quad ; \quad k = \frac{k_{a2}\omega_1^2 - k_{a1}\omega_2^2}{\omega_2^2 - \omega_1^2} \quad (4.28)$$

where the subscripts $_1$ and $_2$ refer to the resonance frequency and stiffness of the air spring for two different back cavity volumes. Experimental and analytical results are in very good agreement for both Lexan plates as shown in Figure 4.17.

Plate resonance frequencies with no back chamber are given in Table 4.6.

	Analytical (Hz)	Experimental (Hz)
0.76-mm Lexan Plate	157	156
1.52-mm Lexan Plate	241	240

Table 4.6. Back chamber volumes for Lexan plate experiment.

Results were extrapolated to $90 \times 90 \times 1.52$ mm and $90 \times 90 \times 0.76$ mm aluminum plates and are shown in Figure 4.18. An average air spring stiffness was determined for each chamber depth by arbitrary setting Δx to 0.635 mm (25 mils).

As seen in Figure 4.18, the air spring is only effective for small back chamber volumes due to the high stiffness of the plate. In addition, the effectiveness drops rapidly as the plate thickness increases since the plate bending stiffness is proportional to h^3 (h is the plate thickness).

From Equation 4.27, nonlinearities can be kept within 10 % if the volume displaced by the plate $S \Delta x$ is less than 4 % of the volume V of the chamber. For an equivalent piston displacement equal to 1.27 mm (50 mils), this result in a minimum chamber depth of 31.75 mm for which the air spring is largely ineffective (Figure 4.18). Therefore, in order for the volume variation approach to be practical, the actuator signal must compensate for the nonlinearities of the air spring. This could be achieved by sensing plate displacement and feeding it back to PZT actuator through a nonlinear controller to ensure that plate motion is truly sinusoidal.

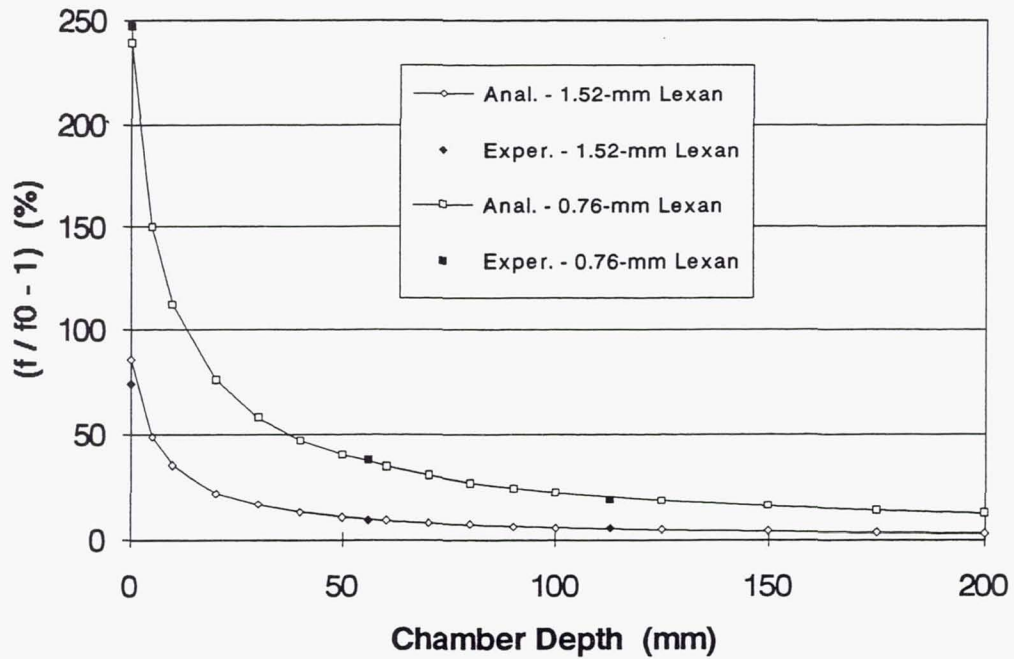


Figure 4.17. (Resonance frequency for plate/back cavity combination) / (Resonance frequency for plate alone) versus chamber depth - (1,1) mode - Lexan plates.

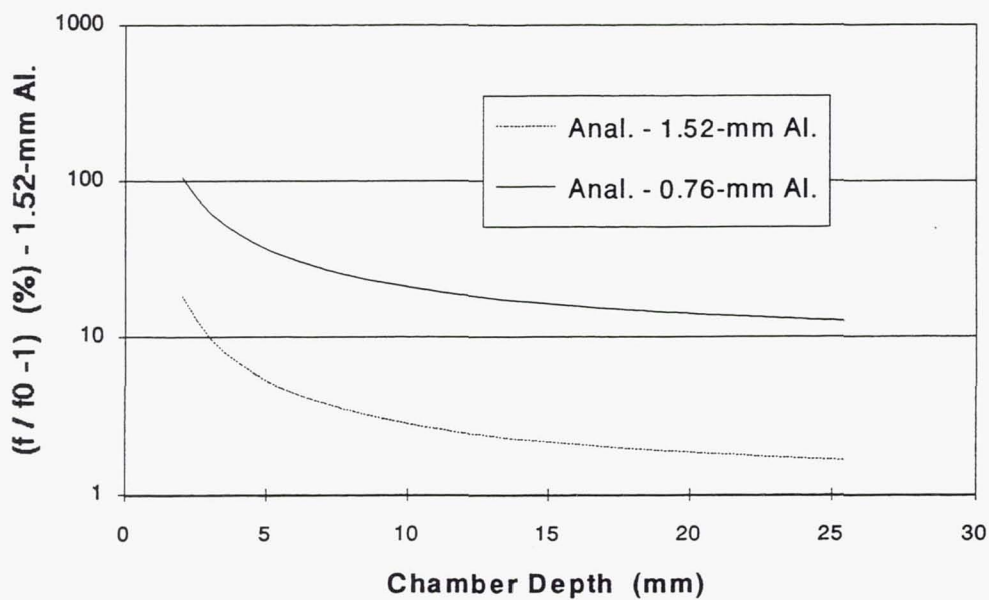


Figure 4.18. (Resonance frequency for plate/back cavity combination) / (Resonance frequency for plate alone) versus chamber depth - (1,1) mode - Aluminum plates.

4.5.2. Adaptive Tuning Through Chamber Pressure Variation

Tests were first carried out using 90×90 Lexan and aluminum plates with thicknesses of 1.524 mm and 0.762 mm. A sealed back pressure chamber shown in Figure 4.19 was fabricated and bolted to the frame. A small port on the back wall of the pressure chamber allowed the pressure in the chamber to be varied from very close to 0 N/m^2 to $413,700 \text{ N/m}^2$ (0 to psi to 60 psi).

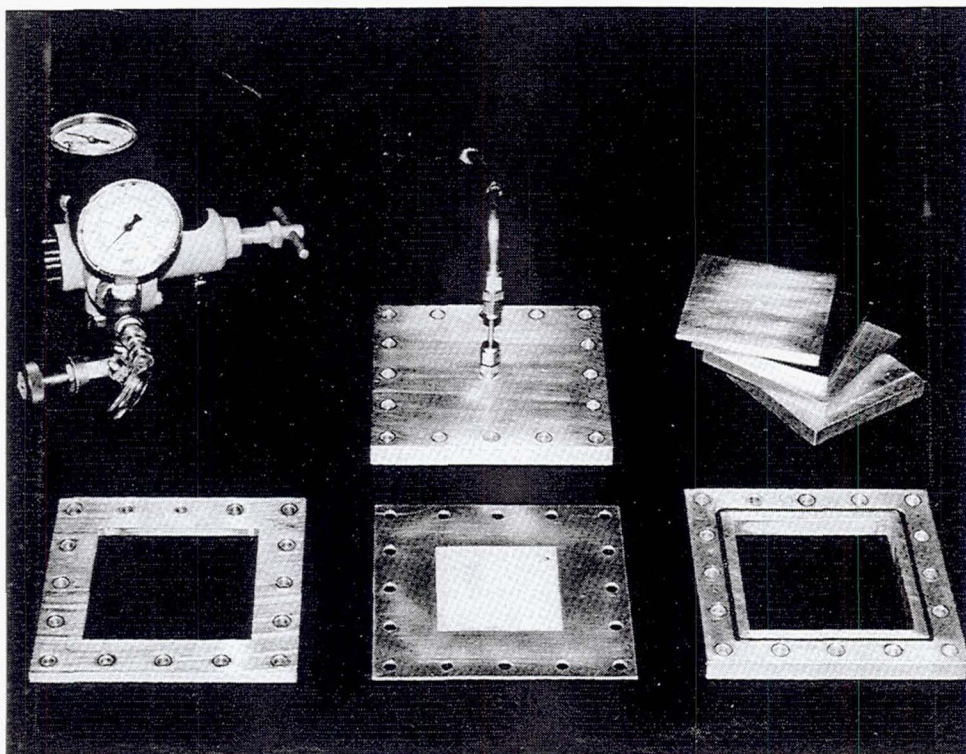


Figure 4.19. Pressure chamber and plate used for adaptive tuning using chamber pressure variation.

Initial tests showed an identical resonance frequency variation for similar pressure differences between each side of the plate whether vacuum or compressed air were used. Therefore, subsequent tests were all run using compressed air only.

Figure 4.20 shows the first mode resonance frequency variation for the Lexan plate. The analytical data only takes into account the stiffening effect of the air spring with increasing chamber pressure. The large difference between analytical and experimental results indicates that the air spring stiffness only plays a minor role in changing the system resonance frequency. In-plane stresses and plate curvature due to the pressure difference across the plate are the two main mechanisms responsible for the change in resonance frequency.

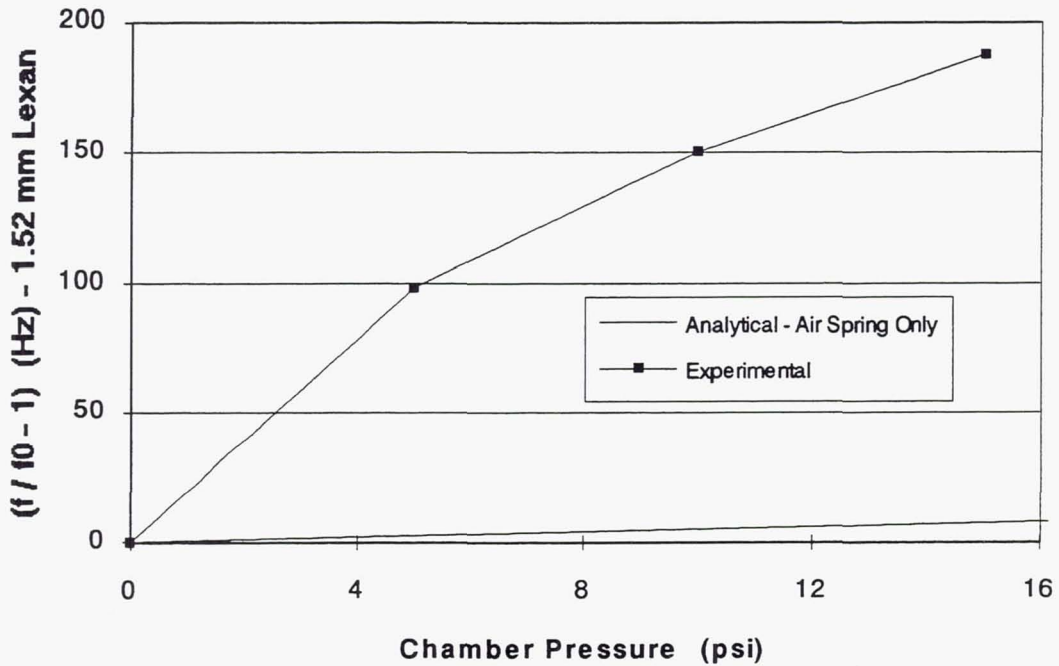


Figure 4.20. (Resonance frequency for plate/back cavity combination) / (Resonance frequency for plate alone) versus back chamber pressure - (1,1) mode - Lexan plate.

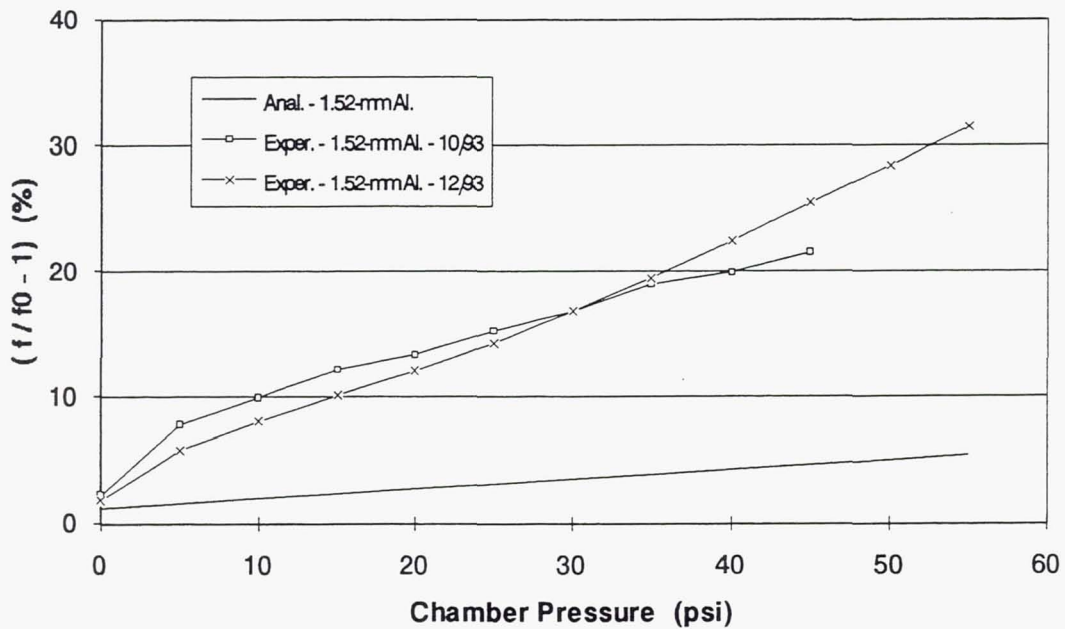


Figure 4.21. (Resonance frequency for plate/back cavity combination) / (Resonance frequency for plate alone) versus back chamber pressure - (1,1) mode - 1.524-mm thick aluminum plate.

Figure 4.21 shows similar results for a 1.52-mm thick aluminum plate. Again, in-plane stresses and curvature effects are dominant. The total frequency variation is significant (about 20%), although much less than for the Lexan plate which has a much lower bending stiffness. As with the volume variation approach, the resonance frequency variation drops as the plate thickness increases. Figure 4.22 shows the plate frequency response for several back chamber pressures for one of the tests. Levels at resonance increase with increasing chamber pressure.

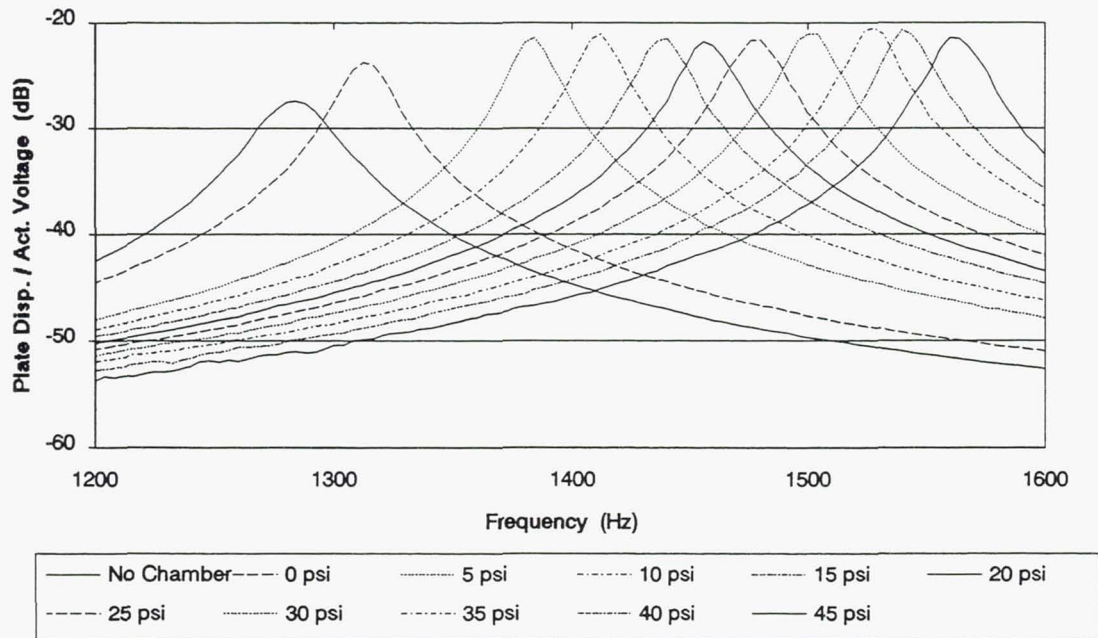


Figure 4.22. Frequency response for several back chamber pressures - (1,1) mode - 1.52-mm thick aluminum plate. 10/93 test.

The velocity response at resonance is shown in Figure 4.23 for both tests as a function of back chamber pressure. The response increases dramatically with increasing pressure in the chamber although the increase is very different for each test for unknown reasons. Additional testing should be performed to identify the cause of this difference. The most likely reason for the change in velocity response is the increase in plate curvature which increases the coupling between the "in-plane" deformation of the actuator and the first bending mode of the plate.

Figure 4.24 shows similar results for a 0.762-mm thick aluminum plate. The total frequency variation is very significant and much larger than for the 1.524-mm plate.

One of the drawbacks of the pressurization approach is plate deformation, which increases stress levels in the actuator and limits the dynamic range of the source. When tested, the thick PZT actuators (0.51 mm) bonded to the aluminum plate failed for a back chamber pressure of 55 psi.

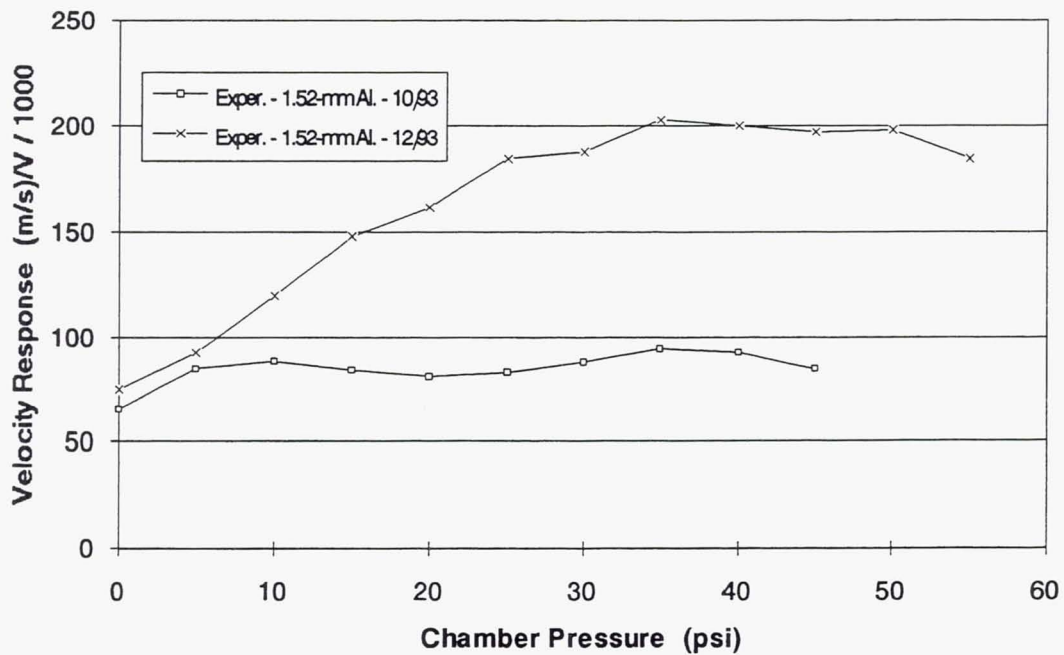


Figure 4.23. Velocity response at resonance for several back chamber pressures - (1,1) mode - 1.52-mm aluminum plate. 10/93 and 12/93 tests.

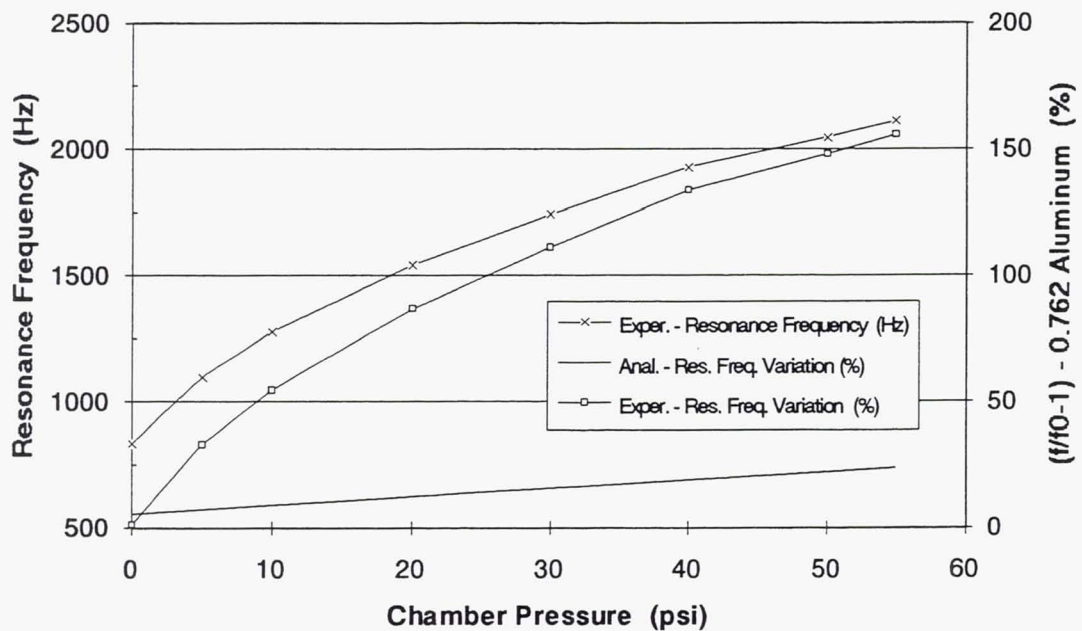


Figure 4.24. Resonance frequency for plate/back cavity combination versus back chamber pressure - (1,1) mode - 0.762-mm aluminum plate.

The static deflection at the center of the plate can be easily calculated and compared with the target dynamic deflection to obtain an estimate of the static versus dynamic stresses in the plate. The deflection w at a center of a square plate of width a and bending stiffness D due to a uniform pressure load P is given by [47]:

$$w = 0.00126 \frac{Pa^4}{D} \quad (4.29)$$

Deflections at the plate center are shown in Figure 4.25 for various aluminum plates. With the exception of the thinner plate, the static deflection is smaller than the dynamic deflection of 3.8 mm corresponding to an equivalent piston displacement of 1.27 mm (50 mils). However, for similar static center deflections, the relative change in resonance frequency is larger for the thinner plate than for the thicker one.

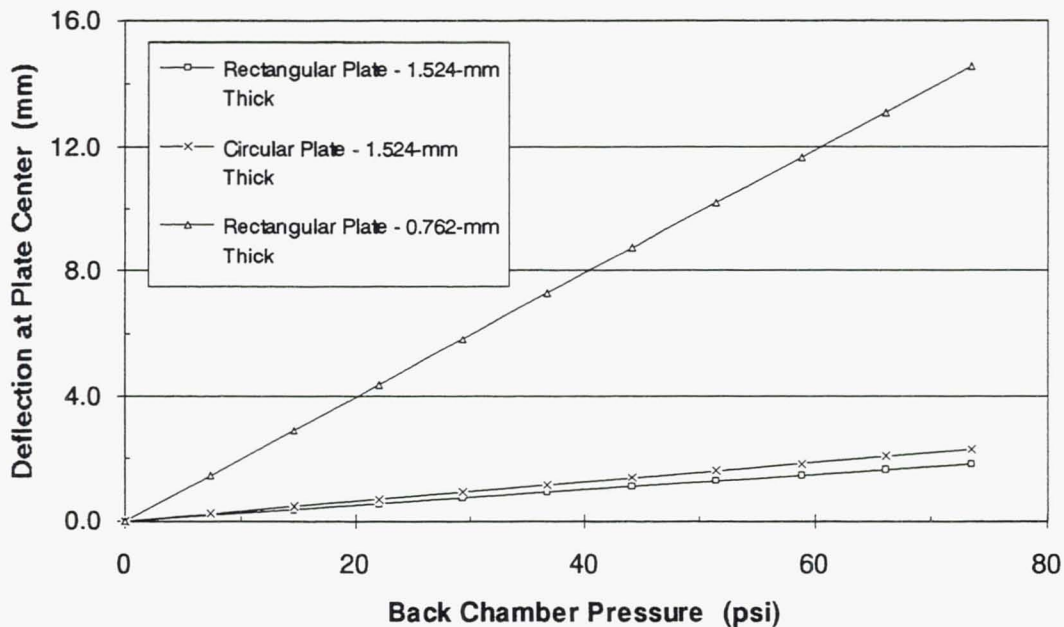


Figure 4.25. Deflection at center of plate versus back chamber pressures for several plates.

Adaptive tuning using back chamber pressurization offers substantial control over the resonance frequency of a plate radiator. Some of the main advantages of this approach are its simplicity and the ease with which it can be implemented since it only requires compressed air. One potential drawback is a reduced dynamic range at high pressure differentials across the plate. However, this reduced dynamic range is accompanied by an increased in overall sensitivity as the plate curvature increases.

4.6. Summary of Adaptive Tuning Methods:

Table 4.7 summarizes some of the benefits and drawbacks of the various adaptive tuning approaches discussed in this Chapter.

Method	Benefits	Drawbacks
Damping Control	Passive - No control system Slow phase variation No DC stresses in plate	Low bandwidth Low maximum displacement Fixed resonance frequency
Linear Stiffness Control	No DC stresses in plate	Very low bandwidth Requires AC feedback system Difficult to implement Rapid phase variation
Bending Stiffness Control	Large bandwidth No DC stresses in plate	Requires AC feedback system Difficult to implement Rapid phase variation
In-Plane Frame Loading	Moderate bandwidth Average implementation difficulty	Requires DC feedback system Requires high-force actuators DC stresses in plate Reduced dynamic range Rapid phase variation
In-Plane Embedded Loading	Low bandwidth Difficult to implement	Requires DC feedback system Requires high-force actuators DC stresses in plate Reduced dynamic range Rapid phase variation
Chamber Pressurization	Moderate bandwidth Easy to implement Only requires compressed air Increase in transducer sensitivity	Requires DC feedback system DC stresses in plate Plate curvature Reduced dynamic range Rapid phase variation
Volume Variation	Low bandwidth Average implementation difficulty No DC stresses in plate	Requires DC feedback system Nonlinearities Rapid phase variation

Table 4.7. Benefits and drawbacks of various adaptive tuning approaches.

5. Conclusions

As stated in the introduction, the main goal of this study was to investigate whether or not volume velocities high enough for canceling aircraft engine fan noise can be generated using piezoceramic-based acoustic plate radiators.

From basic acoustic plate radiation theory and to conform to the work of Kraft and Kontos [7], it is clear that a plate radiator must be operated in its first (1,1) mode. In addition, the frequency of operation must be at or very close to the resonance frequency of the first mode in order to maximize the volume velocity of the source.

An equivalent piston displacement as high as 0.39 mm (15.4 mil) was obtained with the optimized plate samples tested with only one actuator powered. This corresponds to a plate deflection at the center of over 1 millimeter and is only 3 times less than the target displacements set at the beginning of this study (1.27 mm or 50 mils [7]). This displacement also represents a 160-fold improvement over previous work [10] using a similar plate radiator concept.

The magnitudes of the displacements obtained are believed to be very close to the magnitude required for fan noise cancellation in a full size engine at take-off and landing conditions.

A further increase in displacement will easily be achieved by using a double-sided actuator configuration and by refining the plate design and choice of actuator material as described in the next Chapter. Still, much work remains to be done before a flight-worthy plate transducer can be fabricated. Further work should address the minimization of stresses in the actuator, the minimization of nonlinear effects in the ceramics, improvements in the bonding process, and the increase in the transducer bandwidth for engine RPM tracking.

The main results of this study are listed below:

Analytical Modeling and Optimization

Analytical and numerical (FEM) models of beams and plates actuated by piezoceramic thin plates were developed and validated. The models, which include actuator inertial and stiffness effects, were validated experimentally using Lexan and aluminum beam and plate. For aluminum plates, the analytical and experimental responses are within 1 % to 3 % of each other at the low actuator voltage levels investigated.

Once the model was validated, an optimization study was performed. The objective was to identify the design parameters which affect resonance frequency and volume velocity of the first mode and to find the optimum combination of these parameters which maximizes volume velocity for a given resonance frequency for that mode. The parameters varied included:

- Beam/Plate boundary conditions
- Beam/Plate material properties
- Beam/Plate thickness
- Actuator location
- Actuator size
- Actuator thickness
- Single or multiple actuator configuration

Since computer turn-around time for the beam analytical solution is very quick, an extensive optimization study was carried out which would have been too time consuming with the FEM approach. Since there are many similarities in the manner in which beams and plates behave, these results were then used as a starting point for the plate optimization using the FEM method.

Results of the plate optimization point to an aluminum plate with a large double-sided actuator configuration covering 75% of the plate area. The actuators are bonded at the plate center and have an optimum thickness of about 0.28-mm for a 1.52-mm thick plate. Several arbitrary constraints were used such as size and thicknesses of the plate ($90 \times 90 \times 1.52$ or $\times 0.76$ mm). These constraints represent a good compromise between plate size, available thicknesses, resonance frequency, performance, and ease of fabrication, but can be adjusted to fit the application without loss of performance. The plate dimensions were selected so that the resonance frequency of the first mode would occur around 750 Hz and 1500 Hz, which is typical of the frequencies required to cancel aircraft engine fan noise.

Experimental Study

Using results from the optimization study, a double-sided actuator configuration was chosen with the actuators bonded at the center of an aluminum plate. The 66×66 mm actuators covered 54 % of the plate area. This area ratio is lower than the optimum ratio, even though the actuators used were the largest available in this type of material. The piezoceramic material used also had the second highest $d_{31}Y_{11}$ product (piezoelectric constant \times Young's modulus) out of 36 different materials surveyed, which results in a more than 40 % increase in deflection compared to the more conventional actuators materials. The predicted equivalent piston displacement was 0.7 mm for a voltage of 100 Volts RMS.

In total, 15 plate radiators were fabricated and tested with most radiator configurations very close to the optimum plate design. Variations in the configurations tested included plate and actuator material, size, and thicknesses, as well as three different bonding methods.

The following plate radiator properties were investigated:

- Volume velocity versus actuator voltage
- First mode resonance frequency versus actuator voltage
- Plate response at high actuator voltages
- Harmonic distortion
- Effect of actuator number and actuator polarity
- Effect of plate and actuator thickness.

Plate Results - Highlights

The main results for all fifteen plates tested are shown in Tables 3.18 and 3.19. Some of the critical and sometimes unexpected characteristics of the plate radiators tested are listed below:

- The equivalent piston displacement achievable with a PZT actuator-based plate radiator is not limited by the maximum moment available from the actuator, but by the critical stress of the piezoceramic actuator and bonding layer. In other words, the actuators will crack or debond before they start depolarizing and losing their electrical properties as a result of a high electrical field. In general the epoxy bonds performed better than the alkyl cyanolate compound. No debonding took place when using the low-viscosity epoxy on six different plates.
- The plate velocity response is nonlinear, usually dropping as the actuator voltage increases. This is due to the nonlinear behavior of the mechanical and electrical properties of the actuator material at high stress levels and for high electrical fields. However, this strong nonlinearity in the plate average response does not always translate into a strong nonlinearity in the plate velocity waveform.
- The resonance frequency strongly depends on the actuator voltage. Again, this is a result of nonlinearities in the actuator properties such as the dependence on the electrical field of the Young's Modulus of the piezoceramic material.
- Harmonic distortion is typically in the -15 dB to -20 dB range at high actuator voltage levels due mainly to the nonlinear properties of the actuator material.
- Using a double-sided actuator configuration rather than a single-side one effectively doubles the plate response at low actuator voltages. At high voltages, the increase is less (by as much as 30 %).

Stresses in the Piezoceramic Actuator

Since stress-related failure in the actuator is the limiting factor in the design investigated, stresses in the piezoceramic actuator for a typical plate tested were computed using the FEM analysis. Stress levels at the plate center were shown to be in the vicinity of the critical tensile stress level only for very high actuator voltages (> 100 Volts). However, most actuator failures occurred for stress levels substantially below the critical tensile stress. Failure originated either at the center of the actuator, at a corner, or at the location of the copper electrode connecting the power supply to the actuator electrode bonded to the plate.

Several of the factors responsible for the failure of the actuator at a lower tensile stress than expected are listed below:

- The critical stress at which failure occurs depends on transducer design, fabrication, and operating condition, and is difficult to predict from existing data which typically applies to transducer configurations different from the configuration used in this work. As an example, critical stresses depend on many factors such as: direction of stress compared to poling axis, static or dynamic operation, and electrical field.
- Defects in the bonding layer lead to local regions of high stress concentrations which lead to early failure. Defects include residual stresses and inhomogeneities resulting from the curing process, from the large actuator size, and from the thickness of the copper electrode.
- The sharp corners of the actuator lead to very high stress concentration at the corners which can lead to early failure.
- Inhomogeneities in the piezoceramic material itself can lead to weaker regions from which cracks can originate.
- Degradation in the actuator mechanical properties at high stress levels and high electrical fields can lead to early failure.

Finally, a simplified analysis of the fatigue life of the aluminum plate itself was performed showing that maximum stresses are low enough to ensure that the plate will not be prone to fatigue failure.

Adaptive Tuning Study

This work concludes with a study of adaptive tuning methods used to increase the bandwidth of acoustic plate radiators. Adaptive tuning allows the plate radiators to operate over a wide range of frequencies, thus tracking engine RPM variations. In addition, it can be used to match the resonance frequencies of individual radiators which are part of a ring source array in a fan duct.

Several adaptive tuning methods were identified and investigated analytically including passive, active, and semi-active methods:

- *Structural Modification: Damping control.*

Passive approach: The bandwidth is controlled by increasing the radiator damping,

- *Boundary Condition Control: Linear or bending stiffness control.*

Active approach: The plate is tuned by changing the boundary conditions.

- *Control of Plate In-Plane Stresses: Variable in-plane frame loading and variable embedded in-plane loading.*

Semi-active approach: The plate is tuned by changing the plate in-plane stress distribution.

- *Hybrid Stress/Stiffness control: Back chamber pressurization and volume variation.*

Semi-active approach: The plate is tuned by changing the volume and/or pressure in a chamber enclosing the back of the plate. The tuning mechanism is through changes in the plate internal stresses and through the variable stiffness of the chamber.

The back chamber pressurization and volume variation methods were investigated experimentally. Adaptive tuning using back chamber pressurization was shown to be simple and effective way to obtain substantial control over the resonance frequency of a plate radiator with the added potential of an increase in the plate velocity response due to the increase in plate curvature. One drawback of this technique is the reduction in dynamic range as the plate static stresses increase with increasing pressure in the chamber.

It is still too early at this stage of the design to determine which approach is best. Table 4.7 summarizes the benefits and drawbacks of each method. Some approaches such as the bending stiffness control approach offer great performance potential with no added static stresses, but at the expense of a complex system. Therefore, the choice of which method is most appropriate will be a compromise between performance and system complexity.

6. Follow-on Work Recommendations

This chapter describes two key recommendations for the follow-on work:

1. Development and demonstration of a prototype active fan noise control system using a PZT-based acoustic ring source and controller in the NASA Lewis four-foot test fan.
2. Improvements to the current PZT-based acoustic plate radiator design to satisfy aircraft engine flight-worthiness standards.

6.1. Development and Demonstration of an Active Noise Cancellation System for the NASA Lewis Four-Foot Test Fan.

Results of the actuator development described in this report have clearly demonstrated the feasibility of using PZT-based acoustic sources for generating "anti-sound" to cancel fan noise in high-bypass ratio aircraft engines. A logical next step is to design, fabricate, and demonstrate a ring actuator source array based on these PZT acoustic plate radiators, and a controller system for the active control of inlet noise in the NASA Lewis four-foot diameter test fan.

The ring source can be designed as a "ring frame" which is mounted in the four-foot test fan. The ring frame supports several identical acoustic plate radiator elements. Each plate radiator element can be connected to its own power supply for independent amplitude and phase control. Each element consists of an aluminum plate clamped in a frame with a sealed back enclosure allowing variable tuning over a limited frequency range by varying the pressure in the enclosure.

Based on the known characteristics of the NASA Lewis four-foot test fan, and in cooperation with NASA Lewis, the requirements for the ANC system should be established in terms of target fan configuration and operating conditions, choice of inlet or exhaust mode suppression, modes to be canceled, frequency range, and expected noise levels to be canceled. Based on the results of this work, a single acoustic plate radiator element should first be designed and fabricated with the goal being to maximize volume velocity within the required frequency bandwidth of operation.

Several power supply alternatives for the plate radiator elements should be evaluated, including off-the-shelf equipment such as conventional audio power amplifiers and matching networks, or custom-made high-voltage amplifiers. The ring source should include plate radiator elements and power supplies. Proper operation should be checked by powering the ring and measuring vibratory and acoustic frequency response of each element, in both individual and simultaneous operation.

Another effort should be to develop, fabricate, and test a controller system for the cancellation of fan tones in the four-foot test fan. The controller should be designed to operate in either the inlet or exhaust mode and be such that all sensing elements are contained within the fan duct.

The controller operational requirements are based on the operational scenarios for the four-foot test facility. They include the number of system outputs (noise canceling elements), inputs (error sensors), error sensor location, and the constraints that affect controller design such as RPM stability of the test fan and the allowable locations for the error sensors and for the ring source.

Several control approaches should be evaluated in cooperation with NASA Lewis. Proven performance, robustness, upgradability, and cost should be emphasized during the selection process. Control schemes evaluated should include frequency domain and time domain approaches. Modal control schemes that could reduce the complexity of the controller, allow control sensors located in the fan duct, and increase the model control selectivity should be evaluated.

Once installed in the NASA four-foot test fan, the overall system including ring source hardware and controller should then be tested extensively to evaluate its effectiveness in reducing far-field fan noise.

Based on the test results, the configurations offering the best prospect for successful application of active noise control technology to high-bypass aircraft engines would be identified. Recommendations would then be made for further research and development of fan noise active control systems.

6.2. Improvements to the Current PZT-Based Acoustic Plate Radiator Design to Satisfy Flight-Worthiness Standards.

This Section describes in detail the design changes that will lead to a flight-worthy acoustic plate radiator and how to achieve these changes.

The present study has clearly shown that the limiting factor in the design is not how much moment the actuator can transfer to the structure, but how much stress it can take before failing. In addition, strong nonlinearities in the mechanical and electrical properties of the piezoceramic actuator reduce performance at high stress levels and for high electrical fields.

Future work must therefore concentrate on low-stress designs to prevent actuator failure, and increased high-end performance and linearity. The main steps that must be taken to achieve the goal of a flight-worthy plate radiator are listed below:

- *Use a piezoceramic material with the best high-voltage, high-stress properties.*

The Motorola 3203HD piezoceramic material used in most of this study was chosen for its high $d_{31}Y_{11}$ which results in a high response (defined in terms of the ratio of the moment transferred to the electrical field), and for its high quality. This however resulted in a ceramic with highly nonlinear properties and a low critical stress.

Results of this work have clearly shifted the requirements for the actuator material to a material having the best combination of highest critical stress and highest and most stable properties at high stress levels and for high electrical fields. Materials with lower $d_{31} Y_{11}$ products typically have higher critical stress values. In addition, their electrical and mechanical properties are also typically more stable at high stress levels and for high electrical fields. As a result, the velocity response of plate radiators using actuators with lower $d_{31} Y_{11}$ will be lower at low stress levels and low voltages than with current plates. However, at high stress levels and high voltages, the velocity response will not decrease as much as with current plates, resulting in better high-end performance, increased life, and reduced harmonic distortion. In addition, this should also minimize the variation in resonance frequency with actuator voltage level.

- *Use a pre-stressed actuator design.*

The typical actuator tensile critical stress is 3 to 20 times lower than the compressive critical stress. Therefore, pre-stressing the actuator during the bonding process should increase the dynamic range of the plate radiator several fold by operating the actuator mainly in compression.

- *Use multiple actuators each having a smaller area.*

Using smaller actuators will improve the bonding process by allowing a thinner and more uniform bonding layer. This will increase moment transmission to the structure, and reduce local stress concentrations responsible for early failure.

- *Round the Actuator Corners.*

For most plates tested, cracks leading to failure originated at the actuator corners. Therefore, lowering the stress levels at the corners by rounding them will increase the maximum level at which the plate radiators can operate.

- *Use a double-sided actuator configuration*

Although this is an obvious solution, most of the results presented in this work were obtained with a single actuator in order to minimize fabrication cost and time. Using a double-sided actuator configuration will improve plate deflection by 40 % to 100 %.

- *Perform a new optimization study by changing the objective from maximizing the volume velocity alone to simultaneously maximizing the volume velocity and minimizing the maximum stress in the actuator.*

The goal is to find actuator locations where stress levels are lower than in the present design while still being able to generate sufficient plate deflections. As a result of changing the actuator location, the plate response (volume velocity/actuator voltage) will decrease requiring a higher actuator voltage to maintain a constant volume

velocity. This should not be a problem however, as the maximum electrical field used with the present design is well below the maximum allowable electrical field for typical piezoceramic materials (See Appendix D).

- *Remove copper electrode between the plate and the actuator electrode.*

Removing the copper electrode and powering the actuator through the aluminum plate should improve bonding layer uniformity and reduce local stress concentrations leading to early failure.

- *Further improve the bonding technique.*

Bonding is clearly a critical area requiring additional work. Although the Epotek Bond used in many tests represents a clear improvement over the other methods since no debonding occurred, its critical strength and fatigue life remains to be tested. Other bonding methods should also be investigated.

- *Use segmented actuators in combination with a non-uniform plate.*

Innovative designs using non-uniform plates and actuators should be investigated to increase volume velocity and reduce actuator stress levels. For instance, segmented actuators in combination with stress-release grooves in the plate structure between actuator segments can force most of the plate bending to take place between actuators, increasing volume velocity without increasing actuator stress levels.

- *Use "stack actuators" at the plate boundary to drive the plate.*

Finally, the use of piezoelectric or electrostrictive stack actuators should be investigated as an alternate drive system for plate radiators. The design of such a system is basically similar to the arrangement described in Section 4.2.3. on adaptive tuning using the linear or bending stiffness control approach. However, in this application the actuators are used to power the plate rather than to control the stiffness of the boundary. This approach has the potential for minimizing the actuator stress problem although the drawback is the increased complexity of the system.

Additional issues also need to be addressed in future work such as the fatigue life of the actuator and of the bonding layer. Since only limited data is available on piezoceramic materials and bonding materials, it was not possible at this early stage of development to obtain reliable estimates for the fatigue life of the bonding layer and of the actuator.

We believe that these and additional improvements will allow plate radiators to reach and maintain reliably the levels required for the active control of fan noise in full size engines. For instance, a relatively simple change such as the use of pre-stressed actuators has the potential to increase the dynamic range of plate radiators several fold.

7. References

1. Stevens, J. and Ahuja, K., "The State of the Art in Active Noise Control", AIAA 90-3924, AIAA 13th Aeroacoustics Conference, Tallahassee, FL., 1990.
2. Simonich, J., Lavrich P., Sofrin, T., and Topol, D., "Active Aerodynamic Control of Wake-Airfoil Interaction Noise - Experiment," AIAA 92-02-038, 1992.
3. Kousen, K. A. and Verdon, J. M., "Active Control of Wake/Blade-Row Interaction Noise," AIAA 93-4351, 15 AIAA Aeroacoustics Conference, Long Beach, 1993.
4. Simonich, J. C. and Chi, R. M., "Stator Loading Reduction Through Active Aerodynamic Control," AIAA 93-4353, AIAA Aeroacoustics Conference, Long Beach, 1993.
5. Thomas, R. H., Burdisso, R. A., Fuller, C. R., and O'Brien W. F., "Active Control of Fan Noise from a Turbofan Engine," AIAA 93-0597, 31st Aerospace Science Meeting and Exhibit, Reno, NV, 1993.
6. Burdisso, R. A., Thomas, R. H., Fuller, C. R., and O'Brien W. F., "Active Control of Radiated Inlet Noise from Turbofan Engines," Second Conference on Recent Advances in Active Control of Sound and Vibration, pp. 848-860 1993.
7. Kraft, R. E. and Kontos, K. B., "Theoretical Implications of Active Noise Control for Turbofan Engines," AIAA 93-4355, AIAA Aeroacoustics Conference, Long Beach, 1993.
8. Julliard, J., Riou, G., and Lozachmeur, C., "Recent Developments in Turbomachinery Noise Control and Reduction Systems," AIAA 93-4375, AIAA Aeroacoustics Conference, Long Beach, 1993.
9. Berge, D., Bouty, E., and Cailleau, J. M., "Active Noise Control of a Jet Engine at Low Frequency Radiation: BEM for Predicting Far-Field Noise Reduction," AIAA 93-4354, AIAA Aeroacoustics Conference, Long Beach, 1993.
10. Dungan, M. E., "Development of a Compact Sound Source for the Active Control of Turbofan Inlet Noise," Report No. VPI-E-92-23, Virginia Polytechnic institute, October 1992.

11. Bailey, T. and Hubbard, J. E., "Distributed Piezoelectric - Polymer Active Vibration Control of a Cantilever Beam", *Journal of Guidance, Control and Dynamics*, Vol.8, No. 5, pp. 605-611, 1985.
12. Fansen, J. L. and Chen, J. C., "Structural Control by the Use of Piezoelectric Active Members", *Proceedings of NASA/DOD Control-Structure Interaction Conference*, NASA CP-2447, Part II, 1897.
13. Baz, A. and Poh, S., "Optimum Vibration Control of Flexible Beams by Piezoelectric Actuators", NASA CR-180209, 1987
14. Crawley, E. F. and de Luis, J., "Use of Piezoelectric Actuators as Elements of Intelligent Structures" , *AIAA journal*, Vol. 25, No. 10, pp. 1373-1385, 1987.
15. Im, S. and Atluri, S. N., " Effects of a Piezoelectric Actuators on a Finitely Deformed Beam Subjected to General Loading", *AIAA Journal*, Vol. 27, pp. 1801-1807, 1989.
16. Dimitriadis, E. K., Fuller, C. R. and Rogers, C. A., "Piezo- electric Actuators for Distributed Vibration Excitation of Thin Plates", *ASME Journal of Vibration and Acoustics*, Vol. 113, pp. 100-107, 1991.
17. Kim, S. J. and Jones, J. D., "Optimal Design of Piezo Actuators for Active Noise and Vibration Control", *AIAA Journal*, Vol. 29, No. 12, pp. 2047-2053, 1991.
18. Lee, C. K., "Laminated Piezo Polymer Plates for Torsion and Bending Sensors and Actuators", *J. Acous. Soc. Am.*, Vol. 85 (6), pp. 2432-2439, 1989.
19. Lee, C. K. and Moon, F. C., " Modal Sensors/Actuators", *Trans. ASME , J. of Applied Mechanics* , Vol. 57, pp. 434-441, 1990.
20. Jones, J. D. and Fuller, C. R., "Experiments on the Reduction of Propeller Induced Interior Noise by Active Control of Cylinder Vibration", *J. Sound and Vib.*, Vol. 12 (2), pp. 389-396, 1987.
21. Dimitriadis, E. K. and Fuller, C. R., "Investigation of Active Control of Sound Transmission Through Elastic Plates Using Piezoelectric Actuators", *AIAA 12th Aeroacoustics Conference*, April 10-12, San Antonio, TX, AIAA 89-1062, 1989.
22. Wang, B. T. and Fuller, C. R., "Active Control of Structurally Radiated Noise Using Multiple Piezoelectric Actuators", *AIAA 90-1172*, 31st AIAA/ASME/ASCE/AHS Structures, Structural Dynamics, Materials Conference, Long Beach, CA, 1990.

23. Clark, R. L. and Fuller, C. R., "Experiments on Active Control of Structurally Radiated Sound Using Multiple Piezoceramic Actuators," J. Acous. Soc. Am., Vol. 91 (60), pp. 3313-3320, 1992.
24. Fuller, C. R. and Hansen, C., "Active Control of Interior Noise in Model Aircraft Fuselages Using Piezoceramic Actuators", AIAA 90-3922, AIAA 13th Aeroacoustics Conference, Tallahassee, FL, 1990.
25. Sonti, V. R. and Jones, J. D., "Active Vibration Control of Thin Cylindrical Shells Using Piezoelectric Actuators", Proceedings of Recent Advances in Active Noise and Vibration Control, pp. 27-38, Blacksburg, VA, 1991.
26. Lester, H. C. and Lefebvre, S., " Piezoelectric Actuator Models for Active Sound and Vibration Control of Cylinders", Proceedings of Recent Advances in Active Noise and Vibration Control, pp. 3-26, Blacksburg, VA, 1991.
27. Liang, C. and Rogers, C. A., "A Fully-Coupled Acoustic Analysis of Curved PVDF Acoustic Actuators for Active Sound Attenuation", Proceeding of the Conference on Recent Advances in Adaptive and Sensing Materials and Their Applications, Blacksburg, VA, pp. 765-779, 1992.
28. Tiersten, H. F., "Linear Piezoelectric Plate Vibrations", Plenum Press, New York, NY, 1969.
29. Flugge, W., "Handbook of Engineering Mechanics ", McGraw-Hill Book Company, 1962.
30. ANSYS: Engineering Analysis System, Version 4.2, Swanson Analysis System, Inc., Houston, PA, 1985.
31. Fahy, F. Sound and Structural Vibration - Radiation, Transmission, and Response, Academic press, 1985.
32. Blevins, R. D., Formulas for Natural Frequency and Mode Shape, Krieger Publishing Co., 1993.
33. Pierce, A. D., Acoustics - An Introduction to its Physical Principles and Applications, McGraw-Hill, 1981.
34. Wallace, C. E., "Radiation Resistance of a Rectangular Panel," J. Acous. Soc. Am., Vol. 51 (3), pp. 946-952, 1970.
35. Dickinson, S. M., "The Buckling and Frequency of Flexural Vibration of Rectangular, Isotropic and Orthotropic Plates Using Rayleigh's Method," J. of Sound and Vibration, Vol. 61, pp. 1-8, 1978.

36. Krueger, H. H. A., "Stress Sensitivity of Piezoelectric Ceramics: Part 1. Sensitivity to Compressive Stress Parallel to the Polar Axis," J. of the Acous. Soc. of Am., Vol. 42, No. 3, pp. 636-645, 1967.
37. Krueger, H. H. A., "Stress Sensitivity of Piezoelectric Ceramics: Part 3. Sensitivity to Compressive Stress Perpendicular to the Polar Axis," J. of the Acous. Soc. of Am., Vol. 43, No. 3, pp. 583-591, 1968.
38. Berlincourt, D. A. and Krueger, H. H. A., "Behavior of Piezoelectric Ceramics under Various Environmental and Operation Conditions of Radiating Sonar Transducers," Technical Note TP-228, Morgan Matroc Inc.
39. Berlincourt, D. A. and Krueger, H. H. A., "Important Properties of Morgan Matroc Piezoelectric Ceramics," Technical Note TP-226, Morgan Matroc Inc.
40. Guide to Modern Piezoelectric Ceramics, Morgan Matroc Inc.
41. Piezoelectric Ceramics Catalog, EDO Corporation.
42. "Some Design Considerations in the Use of Bimorphs as Motor Transducers," Technical Note TP-237, Morgan Matroc Inc.
43. Carter, R., Piezo Seminar, Vol. 1., Piezo Systems, Inc., 1985.
44. Popov, E. P. , Introduction to Mechanics of Solids, Prentice Hall, 1968.
45. Boyer, H. E., ed., "Atlas of Fatigue Curves," Am. Soc. of Metals, Metals Park, OH, 1985.
46. C. Harris, Editor, Shock and Vibration Handbook, Third Edition, McGraw-Hill, page 33-3, 1988.
47. S. Timoshenko and S. Woinowsky-Krieger. Theory of Plates and Shells, 2nd Edition, page 202, McGraw-Hill Kogakusha, 1959.
48. Venkataramani S., "private communication," GE CRD, Schenectady NY, May 1993.
49. Kensley R., "private communication," Piezo Systems, Inc., Cambridge MA, June 1993.

APPENDIX A

INSTALLATION OF PIEZOELECTRIC ACTUATORS STANDARD OPERATING PROCEDURES JUNE 1992

I. OBJECTIVE

This is the procedure for the installation of piezoelectric actuators on structures. The instructions for installation were adapted from Measurements Group, Inc. bulletin b-129-7, and technical bulletins related to the various components.

II. MATERIALS NEEDED:

PIEZOCERAMIC ELECTRODES

RUBBING ALCOHOL

CLEAN COTTON SWABS & KIM WIPES

CONDUCTIVE SILVER EPOXY ADHESIVE (Tra-duct 2902)

COPPER SHEET

TEFLON SHEET, PLATE, AND SPREADER

SMALL PIECES OF SCRAP LEXAN

SMALL BLACK PINCH TYPE PAPER GRIPS

M-BOND GA -2 ADHESIVE KIT

III. PROCEDURE

Procedures

1.1 Select perfect piezoceramic actuators. Handle carefully by the edges only so as not to contaminate them. Check for cracks and chips, discarding if any are found.

1.2 Clean surface of actuator with rubbing alcohol.

Precautions

1.1 DON'T TOUCH ACTUATOR SURFACE !!

1.2 DON'T TOUCH ACTUATOR SURFACE AFTER CLEANING!

1.3 Cut copper strips from copper sheet using tin snips or sharp scissors. The strips should be 1/4 to 3/8 inch wide and 1 1/2 to 2 inches in length maximum.

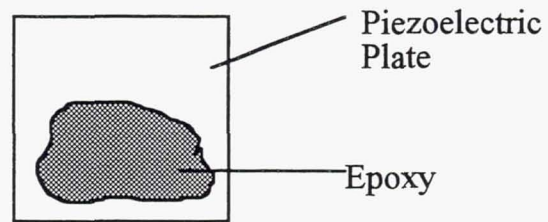
1.3 The less these are handled the better.

1.4 Prepare silver conducting Epoxy by removing the clamp on the package and squeezing the package until the two components are thoroughly mixed and the color is uniform throughout. There will be plenty for 20 or more actuators.

1.4 The epoxy will stay workable for about an hour after mixing.

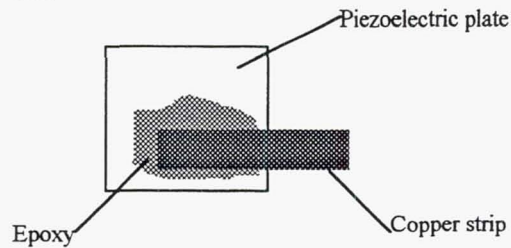
1.5 Put the epoxy on a (Teflon) plate and use a (Teflon) spreader to spread a thin layer on an area of the piezoelectric plate large enough to surround the copper strip as illustrated. Be careful to prevent the epoxy from overflowing (or even reaching) the edges of the plate.

1.5



1.6 Apply copper strip. Press down gently with the clean end of the spreader to seat the strip firmly in the epoxy along its entire length of contact.

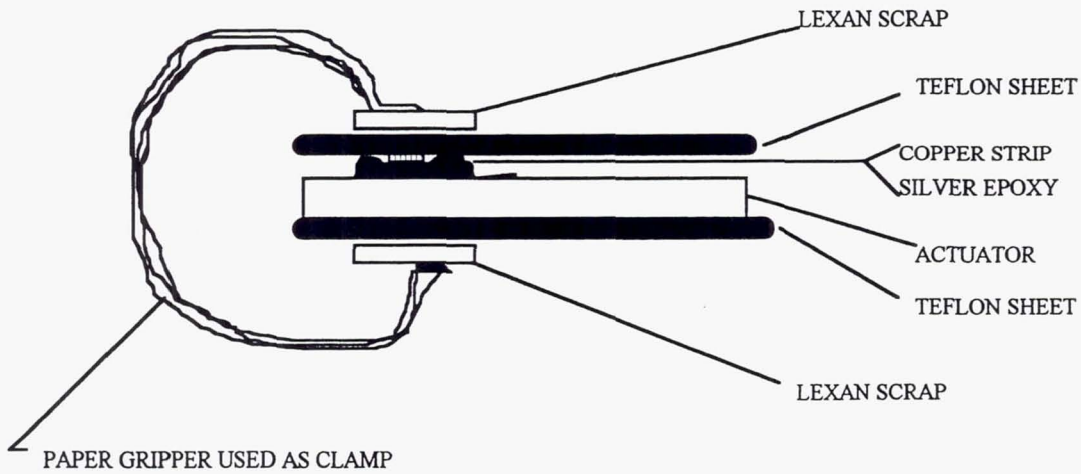
1.6



Because the epoxy is conductive, it is **CRITICAL** that it does not reach or overflow the edge of the plate.

1.7 Apply Teflon sheets to both sides of the electrode/copper strip assembly. Place a scrap piece of Lexan on each side of the sandwich over the copper strip and apply a paper grip, parallel to the copper strip to hold the assembly together. See the cross section illustration below.

SIDE VIEW

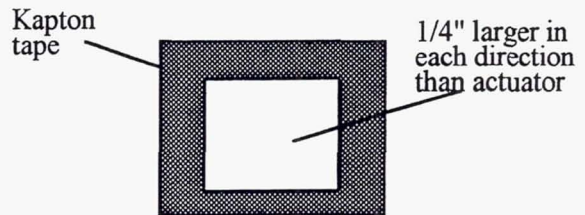


Procedure for Installation

Hints & Tips

CAUTION: READ AND UNDERSTAND THE ENTIRE PROCEDURE BEFORE BEGINNING!

- 2.1 Test the actuators for conductivity.
- 2.2 Determine the location for the application of the actuator on the structure.
- 2.3 Clean an area larger than necessary with degreasing solvent and clean gauze or cotton swabs until the surface is clean and grease free (use Loctite 755 recommended).
- 2.4 Use 1/2" x .002" thick Kapton tape, (or 1" wide cut in half) to mask an area 1/4" larger in each direction than the size of the actuator. For room temperature curing, white freezer tape works better and comes off more easily and neatly and leaves no residue.



2.5 Thoroughly clean the area AGAIN with cotton swab and grain alcohol. Remove any dust with a soft brush. Next, condition using clean gauze and red capped solution, until a clean gauze comes away clean. Then neutralize using the same method and the blue capped solution. If the PZTs don't stick well to plastic, sand lightly while wet with the red cap solution to rough up the surface.

2.6 Prepare GA-2 adhesive. Brush a thin coat of the adhesive on the cleaned area so that the cement is just above the height of the tape. Be sparing of the cement, and make certain there are no air bubbles in it.

2.7 Align the actuator exactly where you want it located and press on to the adhesive GENTLY. Apply a Teflon sheet over the actuator and partially over the mask, taking care that it is free from wrinkles and air bubbles in the cement. Apply a silicone gum sheet (SGP-2) over the Teflon sheet, then apply the soft rubber vacuum pad over all and tape in place.

2.8 Apply heat and vacuum.

Heat at 150 F for about 2 hours, conservatively. (From graph on Measurements Group instructions.)

2.9 When actuator is cured in place, clean the areas to be soldered with alcohol. Apply soft solder liquid flux to the area. Solder one lead wire to copper strip and one lead wire to the piezoceramic plate.

2.5 RED = M-Prep conditioner A (a water-based acidic surface cleaner). BLUE = M-Prep neutralizer 5A (a water based alkaline surface cleaner).

Always begin on the cleaned area and make a single stroke to the edge. Any repeats should be made with a clean gauze. Proceed to the next step within a half hour or so.

2.6 GA-2 adhesive is prepared by weight. Weigh a "dollop" of m-bond adhesive resin (black stuff in jar) in a cup on the scale. Add 10% (by weight) as much of the yellow liquid a drop at a time. 2 grams of the resin is more than enough for one actuator (ie. 2 grams resin & .2 grams curing agent).

2.7 CAREFUL! you still don't want to crack or chip the electrode. This is a real touchy part of the procedure. PUT THE COPPER STRIP FACING THE STRUCTURE!

2.8 WARNING! DO NOT OVERHEAT!
(Otherwise, depolarization may occur.)

APPENDIX B

ACTUATOR BONDING

It is clear from experience and from the analytical work that the bonding between the structure and the piezoceramic actuator is critical. The bonding procedure used for the beam experiments was modified after several nagging problems were identified during the plate experiments using the GA-2 adhesive. Some of the problems were related to the unusually large size of the Motorola PZT actuators used (66×66 mm) which made handling difficult and required a low viscosity adhesive.

- Sudden debonding occurred at very high voltages resulting in a break up of the actuator.
- Large residual stresses were present in the actuator after the curing process was completed.
- The relatively high viscosity of the glue made it difficult to obtain a thin bond with homogeneous thickness, resulting in poor coupling between the actuator and the structure and sometime resulting in a breakage of the ceramic during curing.
- Air bubbles developed in the epoxy, weakening the bond. This problem was noticed when gluing the actuator on a transparent Lexan structure so that the bond could be examined.

The following remedies were applied to minimize the bonding problems described above.

Tests showed that the GA-2 epoxy shrunk when cured at high temperatures, thereby causing the residual stresses. The reason for using high temperature curing in the first place was to increase the stiffness of the bond and to reduce the curing time from 24 hours to less than an hour. As a result, room temperature curing was used for the last plate tests.

Curing of the epoxy at atmospheric pressure showed no bubbles while curing in a vacuum chamber resulted in bubbles in the epoxy due to outgassing. As a result, the use of a vacuum pad was dropped for the last plate tests.

The 2-layer bonding process used on conductive plates was eliminated. The 2-layer process was used to electrically insulate the actuator from the structure. In this process, a thin layer of epoxy is first applied and cured to act as an electrical insulator between the conductive structure and the actuator. The actuator is then bonded to the insulating epoxy layer using another layer of epoxy. Although this process ensures fairly good electrical insulation, it increases the thickness of the bond. In addition, when debonding occurred at high stress levels, it happened at the interface between the two epoxy layers.

Consequently, the insulating layer was eliminated, and the actuators were mounted so that electrodes with the same polarity were facing the structure.

Several other bonding materials were investigated. A modified alkyl cyanolate compound (M-Bond 200 from Measurements Group, Inc.) was tested on several plates. The M-Bond 200 is essentially a "super glue" and was tested since it has been used commonly in the past as a bonding material for PZT actuators by several research laboratories. Its advantages are simple handling and fast room-temperature cure. However, it tends to debond suddenly at high strain levels and its properties degrade with time and non-standard environmental conditions.

Another epoxy, EPO-TEK 301 from Epoxy Technology, Inc., which has been used on unrelated piezoceramic projects at GE CRD was tested on plate samples. The EPO-TEK 301 adhesive cures at room temperature overnight and has about half the stiffness of the GA-2, but a much lower viscosity which allows much thinner bonds. No sudden debonding occurred and the ceramics usually did not break during curing.

In addition, a 1-mil copper strip was used to connect the back electrode of the actuator to the power wires instead of the 3-mil copper strips used previously. The size of the copper strip was also reduced to a minimum so as not to interfere with the bond between the actuator and the structure.

APPENDIX C

PROPERTIES OF PIEZOCERAMIC MATERIALS

Properties for PZT materials for several manufacturers are listed in Tables C.1 and C.2. Table C.1 ranks materials by manufacturers. Table C.2 ranks materials by $d_{31}Y_{11}$ which is proportional to the moment applied by the actuator to the structure as shown in Equation 3.9. An increase in $d_{31}Y_{11}$ is usually accompanied by a decrease in the maximum temperature allowable (Curie temperature) and by a decrease in the value of the coercive electric field which is proportional to the maximum allowable electric field across the piezoceramic material. Therefore, the choice of an optimum material is a compromise which depends on how much moment must be transferred to the structure considering the voltage and temperature constraints. The D3203HD ceramic from Motorola has the second highest $d_{31}Y_{11}$ of all the materials surveyed with a fairly good Curie temperature of 260 degrees C and a high coercive field of 27 V/mil. It was recommended for this application by Dr. Venkataramani from the Electrical Ceramics Program at GE CRD.

	Piezo Kinetics				EDO Corp.					
	PKI 800	PKI 400	PKI 500	PKI 550	EC-63	EC-67	EC-65	EC-66	EC-70	EC-76
d33	220	275	400	550	270	241	355	415	480	583
d31 x E-12 m/V	100	120	175	270	120	107	173	215	260	262
Curie Temp. C	320	310	350	200	320	300	350	270	220	190
Density	7.6	7.5	7.6	7.5	7.5	7.5	7.5	7.45	7.45	7.45
k3	1000	1240	1700	3200	1250	1100	1725	2125	2750	3450
kp	0.51	0.52	0.6	0.63	0.58	0.56	0.62	0.62	0.63	0.64
Y11 E+10 N/m2	7.2	7.6	7.1	6	8.1	8.3	6.6	6.5	6.4	6.4
Loss Tangent	0.004	0.005	0.015	0.022						

	Vernitron						Motorola						
	PZT7A	PZT4	PZT5A	PZT5B	PZT5J	PZT5H	B3198	F3195	D3197	F3211	D3199	D3189	D3203
d33	153	285	374	405	500	593	223	390	446		492	534	552
d31 E-12 m/V	60	122	171	185	220	274	97	179	205	244	251	260	283
Curie Temp. C	350	325	365	330	250	195	320	350	330	280	230	240	260
Density	7.7	7.6	7.7	7.6	7.4	7.5	7.8	7.8	7.8	7.8	7.8	7.8	7.8
k3	425	1300	1700	2000	2600	3400	950	1800	2150	2650	3250	3100	3300
kp	0.52	0.58	0.6	0.6	0.6	0.65	0.55	0.63	0.66	0.68	0.66	0.68	0.69
Y11 E+10 N/m2	9.3	8.2	6.1	6.1	6.2	6.1	9.5	6.9	6.8	6.31	6.5	10.9	6.28
Loss Tangent							0.004	0.018	0.02	0.02	0.02	0.02	0.02
Coercive Field (kV/cm)								14.9	14.4	10.8	10.9	23.2	10.6

	P.E.P. Inc.						Channel Industries, Inc.							
	G-1195		G-1512		G-1278		5400	5500	5804	1300	5600	5700	5800	
	Nickel	Silver	Nickel	Silver	Nickel	Silver	Navy I	Navy II	Navy III	Navy IV	Navy V	Navy VI		
d33							300	400	240	145	505	550	245	
d31 E-12 m/V		190	170	225	205	250	230	135	185	105	56	225	250	107
Curie Temp. C		360	360	240	240	170	170	>300	>350	>300	>115	>240	>190	>300
Density		7.6	7.6	7.6	7.6	7.5	7.5	7.55	7.6	7.55	5.55	7.5	7.4	7.55
k3		2000	1800	2800	2600	4000	3600	1300	1750	1050	1350	2600	3200	1100
kp		0.6	0.58	0.6	0.58	0.58	0.55	0.6	0.62	0.54	0.3	0.62	0.62	0.55
Y11 E+10 N/m2		6.3	6.3	6.3	6.3	6	6	8.2	6.4	8.6	11.9	6.2	6.2	8.6
Loss Tangent		0.022	0.018	0.025	0.02	0.03	0.025	0.004	0.02	0.004	0.008	0.02	0.02	0.004
Coercive Field (kV/cm)		12	12			6	6							
Rec. Max DC Volt. (V/mils)		20	20			10	10	+50/-13	+38/-4	+75/-18			+25/-2	
Rec. Max AC Volt. (p-p V/mils)		3	3			2.5	2.5	15	5	20			3	

Table C.1. Piezoceramic materials - Ranking by manufacturer

	Ver.	Channel	P.K.	EDO	Channel	P.K.	Channel	Mot.	EDO	Ver.	Ver.	P.E.P.	
		1300			5804								G-1195
	PZT7A	Navy IV	PKI 800	EC-67	Navy III	PKI 400	5800	B3198	EC-63	PZT4	PZT5A	Silver	
d31 E-12 m/V	60	56	100	107	105	120	107	97	120	122	171	170	
Y11 E+10 N/m2	9.3	11.9	7.2	8.3	8.6	7.6	8.6	9.5	8.1	8.2	6.1	6.3	
d31xY11 E-2 N/mV	558	666.4	720	888.1	903	912	920.2	921.5	972	1000.4	1043.1	1071	
d33	153	145	220	241	240	275	245	223	270	285	374		
Curie Temp. C	350	>115	320	300	>300	310	>300	320	320	325	365	360	
Density	7.7	5.55	7.6	7.5	7.55	7.5	7.55	7.8	7.5	7.6	7.7	7.6	

	Channel	Ver.	EDO	Channel	P.E.P.	Mot.	P.K.	P.E.P.	Ver.	P.E.P.	Mot.	Channel
	5400			5500		G-1195		G-1512		G-1278		5600
	Navy I	PZT5B	EC-65	Navy II	Nickel	F3195	PKI 500	Silver	PZT5J	Silver	D3197	Navy V
d31 E-12 m/V	135	185	173	185	190	179	175	205	220	230	205	225
Y11 E+10 N/m2	8.2	6.1	6.6	6.4	6.3	6.9	7.1	6.3	6.2	6	6.8	6.2
d31xY11 E-2 N/mV	1107	1128.5	1141.8	1184	1197	1235.1	1242.5	1291.5	1364	1380	1394	1395
d33	300	405	355	400		390	400		500		446	505
Curie Temp. C	>300	330	350	>350	360	350	350	240	250	170	330	>240
Density	7.55	7.6	7.5	7.6	7.6	7.8	7.6	7.6	7.4	7.5	7.8	7.5

	EDO	P.E.P.	P.E.P.	Mot.	Channel	P.K.	Mot.	EDO	Ver.	EDO	Mot.	Mot.
	G-1512		G-1278		5700							
	EC-66	Nickel	Nickel	F3211	Navy VI	PKI 550	D3199	EC-70	PZT5H	EC-76	D3203	D3189
d31 E-12 m/V	215	225	250	244	250	270	251	260	274	262	283	260
Y11 E+10 N/m2	6.5	6.3	6	6.31	6.2	6	6.5	6.4	6.1	6.4	6.28	10.9
d31xY11 E-2 N/mV	1397.5	1417.5	1500	1539.64	1550	1620	1631.5	1664	1671.4	1676.8	1777.24	2834
d33	415				550	550	492	480	593	583	552	534
Curie Temp. C	270	240	170	280	>190	200	230	220	195	190	260	240
Density	7.45	7.6	7.5	7.8	7.4	7.5	7.8	7.45	7.5	7.45	7.8	7.8

Ver.: Vernitron
P.K.: Piezo Kinetics
P.E.P.: Piezo Electric Products

EDO: EDO Corporation
Mot.: Motorola
Channel: Channel Industries

Table C.2. Piezoceramic materials - Ranking by (d13 x Y11)

APPENDIX D

VOLTAGE LIMITATIONS FOR PIEZOELECTRIC MATERIALS

PZT voltage limits are shown in Table D.1 for several products and manufacturers. Voltage limits indicated by manufacturers are usually conservative and vary widely from one product or manufacturer to the other even for the same material. For instance, the commonly used G-1195 material from Piezo Electric Product (which is no longer in business) and from Piezo Systems have very different DC and AC voltage limits even though the materials are the same. In addition, Piezo Systems recommends an AC voltage limit of 9.8 Volt/mil peak for their G-1195 ceramic, even though some of the G-1195 based piezoceramic motor products have maximum recommended voltage limits of 28 V/mil peak.

The applied DC voltage in the direction of polarization can be as high as the polarization voltage [48,49]. This can be as high as 50 V/mil under the proper conditions for the G-1195 material. However, to be safe, the voltage should be limited to 30 V/mil. When the voltage is applied in a direction opposite to the polarization direction such as in AC operation, the maximum "safe" voltage is 12 V/mil. In addition, as frequency increases in AC operation, the maximum allowable voltage increases since the material does not have the time to depolarize as a result of the time constant of the poling process being longer than the period of the excitation signal.

As an example of maximum recommended voltages for a typical plate radiator application, we can take the case of a thin sheet G-1195 PZT actuator bonded on an aluminum plate acoustic radiator. If the maximum applied voltages are 30 V/mil in the poling direction and 12 V/mil in the other direction, the total AC variation can be as high as 21 V/mil peak for a 9 V DC bias in the poling direction. Therefore, the maximum voltages for PZT actuators of various thicknesses are:

PZT Thickness (mils)	Maximum RMS Voltage (Volts)
10	148
20	297
40	594

Table D.2. Maximum actuator voltage versus actuator thickness

Assuming 12 V/mil (conservative) and 30 V/mil (high) maximum voltages in either directions, the maximum AC RMS voltages are:

	Piezo Kinetics				EDO Corp.		
	PKI 800	PKI 400	PKI 500	PKI 550	EC-65	EC-70	EC-76
DC (Polarization Direction) (Volt/mil)	20.3	17.8	15.2	10.2	15	11	10
DC (Opposite Pol. Dir.) (Volt/mil)	10.2	8.9	7.6	5.1	7.5	5.5	5
AC (Volt/mil peak)	10.2	8.9	7.6	5.1	7.5	5.5	5

	Vernitron	P.E.P. Inc.	Motorola		
	Typical	G-1195	F3195	D3189	D3203
DC (Polarization Direction) (Volt/mil)		20			
DC (Opposite Pol. Dir.) (Volt/mil)					
AC (Volt/mil peak)	13 to 25	3			
Coercive Field (V/mil)			38	59	27

	Piezo Systems, Inc	Channel Industries, Inc.			
	G-1195	5400 Navy I	5500 Navy II	5804 Navy III	5700 Navy VI
DC (Polarization Direction) (Volt/mil)	55	50	38	75	25
DC (Opposite Pol. Dir.) (Volt/mil)	9.8	13	4	18	2
AC (Volt/mil peak)	9.8	15	5	20	3

Table D.1. Piezoceramic materials - Maximum allowable electrical field.

PZT Thickness (mils)	Maximum Voltage (Volt/mil)	Maximum RMS Voltage (Volts)
10	12	85
10	30	212
20	12	170
20	30	424

Table D.3. Maximum actuator AC RMS voltage versus actuator thickness

High temperature can be a problem when drive voltage, frequency, and stress levels are high. However, the typical failure mode is cracking of the ceramic due to high stresses rather than depolarization due to the elevated temperatures.

REPORT DOCUMENTATION PAGE

Form Approved
OMB No. 0704-0188

Public reporting burden for this collection of information is estimated to average 1 hour per response, including the time for reviewing instructions, searching existing data sources, gathering and maintaining the data needed, and completing and reviewing the collection of information. Send comments regarding this burden estimate or any other aspect of this collection of information, including suggestions for reducing this burden, to Washington Headquarters Services, Directorate for Information Operations and Reports, 1215 Jefferson Davis Highway, Suite 1204, Arlington, VA 22202-4302, and to the Office of Management and Budget, Paperwork Reduction Project (0704-0188), Washington, DC 20503.

1. AGENCY USE ONLY (Leave blank)	2. REPORT DATE March 1995	3. REPORT TYPE AND DATES COVERED Final Contractor Report	
4. TITLE AND SUBTITLE Active Control of Fan Noise-Feasibility Study Volume 2: Canceling Noise Source-Design of an Acoustic Plate Radiator Using Piezoceramic Actuators		5. FUNDING NUMBERS WU-538-03-11 C-NAS3-26617	
6. AUTHOR(S) F.G. Pla and H. Rajiyah		8. PERFORMING ORGANIZATION REPORT NUMBER E-9475	
7. PERFORMING ORGANIZATION NAME(S) AND ADDRESS(ES) General Electric Aircraft Engines 1 Neumann Way P.O. Box 156301 Cincinnati, Ohio 45214-6301		10. SPONSORING/MONITORING AGENCY REPORT NUMBER NASA CR-195440	
9. SPONSORING/MONITORING AGENCY NAME(S) AND ADDRESS(ES) National Aeronautics and Space Administration Lewis Research Center Cleveland, Ohio 44135-3191		11. SUPPLEMENTARY NOTES Project Manager, Laurence J. Heidelberg, Propulsion Systems Division, NASA Lewis Research Center, organization code 2770, (216) 433-3859.	
12a. DISTRIBUTION/AVAILABILITY STATEMENT Unclassified - Unlimited Subject Categories 07 and 71 This publication is available from the NASA Center for Aerospace Information, (301) 621-0390.		12b. DISTRIBUTION CODE	
13. ABSTRACT (Maximum 200 words) The feasibility of using acoustic plate radiators powered by piezoceramic thin sheets as canceling sources for active control of aircraft engine fan noise is demonstrated. Analytical and numerical models of actuated beams and plates are developed and validated. An optimization study is performed to identify the optimum combination of design parameters that maximizes the plate volume velocity for a given resonance frequency. Fifteen plates with various plate and actuator sizes, thicknesses, and bonding layers were fabricated and tested using results from the optimization study. A maximum equivalent piston displacement of 0.39 mm was achieved with the optimized plate samples tested with only one actuator powered, corresponding to a plate deflection at the center of over 1 millimeter. This is very close to the deflection required for a full size engine application and represents a 160-fold improvement over previous work. Experimental results further show that performance is limited by the critical stress of the piezoceramic actuator and bonding layer rather than by the maximum moment available from the actuator. Design enhancements are described in detail that will lead to a flight-worthy acoustic plate radiator by minimizing actuator tensile stresses and reducing nonlinear effects. Finally, several adaptive tuning methods designed to increase the bandwidth of acoustic plate radiators are analyzed including passive, active, and semi-active approaches. The back chamber pressurization and volume variation methods are investigated experimentally and shown to be simple and effective ways to obtain substantial control over the resonance frequency of a plate radiator. This study shows that piezoceramic-based plate radiators can be a viable acoustic source for active control of aircraft engine fan noise.			
14. SUBJECT TERMS Aircraft flyover noise; Active noise control; Noise suppression; Piezoceramic actuators; Acoustic radiation; Plate radiators		15. NUMBER OF PAGES 150	
17. SECURITY CLASSIFICATION OF REPORT Unclassified		16. PRICE CODE A08	
18. SECURITY CLASSIFICATION OF THIS PAGE Unclassified	19. SECURITY CLASSIFICATION OF ABSTRACT Unclassified	20. LIMITATION OF ABSTRACT	